Spring 4-25-2013

Optimization of Induced-Power from Dynamic Inflow Theory with Realistic Constraints

Chad File
Washington University in St. Louis

WASHINGTON UNIVERSITY IN ST. LOUIS

School of Engineering and Applied Science

Department of Mechanical Engineering & Materials Science

Thesis Examination Committee:
David A. Peters, Chair
Ramesh Agarwal
Mark Jakiela
Swami Karunamoorthy
Norman Katz
Shankar Sastry

Optimization of Induced-Power from Dynamic Inflow Theory with Realistic Constraints

by

Chad L. File

A dissertation presented to the
Graduate School of Arts and Sciences
of Washington University in partial fulfillment of the
requirements for the degree of

DOCTOR OF PHILOSOPHY

May 2013
Saint Louis, Missouri

Contents

List of Figures

List of Tables

List of Abbreviations

a	slope of lift curve, rad^{-1}
A	rotor disk area
$[A]$	loading controls matrix
a_n^m, b_n^m	induced-flow states, He model
aoa	angle of attack
$[B]$	loading inflow feedback matrix
c	blade chord, (m)
C_L	roll moment coefficient
$C_{\mathscr{L}}$	lift coefficient
C_M	pitch moment coefficient
C_P	coefficient of power
C_T	thrust coefficient
$\{C\}$	rotor loads and loading constraints
$\{D\}$	vector representation of the mode shape integrals
$[D]$	loads matrix
$F()$	functional
$[G]$	generic matrix of mapping transformation
H	number of defined controls
$[I]$	identitiy matrix
$\hat{i}, \hat{j}, \hat{k}$	unit vectors in Cartesian system
IPR	induced-power ratio
J	maximum number of loading constraints
k	blade harmonic
K	maximum power of $\bar{r}$ in controls
$\mathscr{L}_q$	blade lift per unit length, q^{th} blade
$[\tilde{L}]$	influence coefficient matrix
$[\bar{L}]$	modified $[\tilde{L}]$

$[\bar{L}_s]$ symmetric part of $[\bar{L}]$

$[\hat{L}]$ influence coefficient matrix

$[\mathscr{L}]$ mass and influence coefficient coupling matrix

M maximum harmonic number

$[M]$ mass matrix

$[M]_{\texttt{swirl}}$ modified apparent mass matrix

N total number of inflow states

p flow field pressure, (N/m^2)

P non-dimensional pressure

$\bar{P}_n^m()$ normalized associated Legendre function of the first kind

$[P]$ matrix of loadings vs. controls

ΔP pressure drop across the disk

Q number of blades

$\bar{Q}_n^m()$ normalized associated Legendre function of the second kind

$[Q]$ symmetric optimizing matrix

R rotor radius, (m)

$\bar{r}$ non-dimensional radial position

$[R]$ harmonic expansion of coupling matrix

$[R_s]$ symmetric part of $[R]$

$S_{n,k}^m$ inflow expansion integral

t time, (s)

T non-dimensional time period, $(0, 2\pi)$

$\bar{t}$ non-dimensional time $(\bar{t} = \Omega t)$

$[T]$ matrix of loadings vs. circulation

$[T]_k$ harmonic transformation matrix

U_T, U_P tangential and perpendicular velocity components, (m/sec)

δv perturbation velocity, (m/s)

$\vec{v}$ non-dimensional velocity

$\vec{V}$ total velocity, (m/s)

V_∞ free-stream speed

$w()$ non-dimensional induced flow distribution

x, y, z Cartesian coordinates

$\{Y\}$ generic vector of constraints

α_n^m,β_n^m induced flow states

γ blade circulation

$\{\gamma\}$ lift expansion vector

$\delta()$ variational operator

$\delta_{n,j}$ Kronecker delta

ε_{IP} induced-power efficiency

$\{\zeta\}$ vector of scaled loads

η ellipsoidal coordinate that represents ellipsoids

θ pitch angle, (rad)

$\{\theta\}$ rotor controls vector

κ empirical swirl factor

λ inflow ratio

$\{\Lambda\}$ Lagrange multipliers

μ advance ratio

ν ellipsoidal coordinate that represents hyperboloids

ξ nondimensional vector parallel to streamline directed upstream

ϱ air density, (kg/m^3)

ρ_n^m normalization function

σ blade solidity, $(Qc/\pi R)$

τ_n^m pressure expansion coefficients

φ angle between lift and thrust

Φ pressure potential function

ϕ_j^r polynomial in $\bar{r}$, $(\bar{P}_n^m(\nu)/\nu)$

χ inflow skew angle

ψ azimuth angle of blade from rotor aft

Ψ velocity potential function

Ω rotor rotational speed, (rad/s)

Subscript

c,s temporal cosine or sine portion, respectively

k blade twist number

n, j polynomial number

q blade index

Superscript

c,s	spatial cosine or sine portion, respectively
m, r	harmonic number
$()^A$	unsteadiness terms
$()^V$	convection terms

Operator

$\vec{\nabla}$	differential operator in 3-dimensions
Δ	difference operator
$L[]$	linear operator acting on convective terms
$M[]$	linear operator acting on unsteady terms
$\frac{d()}{d\bar{t}}$	non-dimensional time derivative
$\frac{\partial()}{\partial\xi}$	non-dimensional gradient along free-stream
$()^T$	transposition of matrix or vector
$\{\} \cdot \{\}$	inner product between two vectors

Acknowledgments

The work completed in this research is funded by the joint agreement between Georgia Institute of Technology and Washington University in St Louis under the Vertical Lift Research Center of Excellence (VLRCOE), Technical Monitor, Michael Rutkowski.

A note of acknowledgment is due to Dr. Robert Ormiston of NASA Ames in Moffet Field, California. Dr. Ormiston granted his insipring thoughts and assistance during the early years of this work that planted a solid foundation for insight and understanding into the questions of rotorcraft performance. I truly appreciate the generosity and persistance that was presented during our short work together.

I would like to extend a most sincere thanks to my advisor, Dr. David Peters. His openess and generousity are the traits of a true mentor. Without his continued support and guidance this thesis would not be what it is today. I cannot express enough the confidence that was gained through the many conversations with Dr. Peters. I am eternally grateful for his encouraging words, unending patience, and very cheerful attitude.

Chad L. File

Washington University in Saint Louis
May 2013

To my wife Tabitha, and our beautiful daughters McKenzie and Amelia. This would not have been possible without your love and support... thank you.

ABSTRACT OF THE DISSERTATION

Optimization of Induced-Power from Dynamic Inflow Theory

with Realistic Constraints

by

Chad L. File

Doctor of Philosophy in Aerospace Engineering

Washington University in St. Louis, 2013

Research Advisor: Professor David A. Peters

Finite-state induced-inflow theory is used to develop an analytic formulation for general performance of the lifting rotor with arbitrary loading. The theory incorporates conventional blade-element theory for blade lift and provides the integrated loads and the induced-power of the rotor in terms of an arbitrary number of rotor controls such as conventional collective and cyclic pitch as well as higher harmonic radial and azimuthal pitch. The theory provides the basis for a classical quadratic optimization with realistic constraints that is applied to determine minimum induced-power for a variety of available control combinations, rotor trim constraints, and operating conditions. The findings show significantly increased induced-power relative to ideal Glauert power at moderate and high advance ratios that also depends on the rotor moment trim constraints. Higher harmonic and radial blade twist significantly reduce the non-ideal induced-power increment. It appears that increasing the available controls enables the optimum solution to redistribute the rotor loading so as to minimize the induced-power.

Chapter 1

Introduction

1.1 Problem Statement

Lifting-rotor induced-power represents the most fundamental component of rotary-wing vehicle performance. Intimately related to the rotor wake flow-field, research in these areas dates back to the early development of the autogyro in the 1920s. Difficulty of modeling the complex rotor wake has hampered progress in accurate analytical performance prediction methods. Simple models (e.g., those based on momentum theory) capture the basics of rotor induced-power, but fail to provide important details. This limits rotor performance prediction accuracy and obscures fundamental understanding needed for the intelligent design of efficient rotorcraft.

Over the years, these difficulties have led to the development of numerical methods based on either elaborate, discrete-vortex-filament wakes or on computational fluid dynamics (CFD). Either of these approaches can be very effective, but they are computationally expensive and provide little fundamental insight about rotor inflow and induced-power. Particularly elusive is understanding the nature of optimum induced-power (i.e., minimum power), and how to achieve it.

These problems are important given current emphasis on increasing the speed and efficiency of military and civil rotorcraft. As speed and rotor advance ratio increase, and as compound rotorcraft with slowed and unloaded rotors pose additional questions, the need to rationally design for minimum induced-power to maximize rotorcraft performance becomes more urgent.

Despite the difficulty and limited progress in developing analytical methods and in understanding induced-power, a few researchers have made incremental progress, particularly in recent years. The intent of this research is to pursue and extend the analytical approach. Existing theory and recent research will first be briefly summarized.

1.2 Early Research, Rotor Wake Induced Inflow and Power

As noted above, Glauert's classical momentum theory, Ref.[1], provides the simplest theory for the lifting-rotor in both hover (axial) and forward (edgewise and oblique) flight. Classic momentum theory represents the wake induced flow by a simple uniform induced velocity field that also defines the ideal minimum, or optimum, induced-power. However, this ignores the influence of non-uniform induced velocity that is responsible for significant increases in induced-power above the ideal minimum at higher advance ratios.

In axial flow conditions, considerable theory was developed in the 1930's, primarily for propeller applications. Axisymmetric flow facilitated development of several classical analytical treatments. The most significant were the lightly-loaded propeller theories of Betz, Goldstein, and Prandtl, Refs.[2] - [4]. Betz defined the induced inflow condition for optimum power. Goldstein's theory, based on the Betz condition, is noteworthy in that it provides a rigorous potential flow solution for the optimum loading of a propeller with an arbitrary number of blades, converging to the actuator disk case for an infinite blade number at low climb rate. It implicitly treats swirl angular momentum and local inclination of the blade lift. Nevertheless, Goldstein theory does not address the general case of non-optimum loading.

Progress for the lifting-rotor in forward flight has been considerably more limited. Analytical work on lifting-rotor wake induced velocity in forward flight was accomplished in the 1950's and 1960's by Mangler and Squire, Refs.[5]-[6], and Joglekar and Loewy, Ref.[7], based on a potential flow solution for a circular wing by Kinner, Ref.[8]; but only limited success was achieved, and the effects of blade number on

induced-power in forward flight were not included (i.e., they treated as infinite number of blades). In view of the difficulties with analytical methods in forward flight, the emergence of the digital computer in the 1960's enabled discrete-vortex numerical models to be introduced as a practical alternative approach for rotor wake prediction purposes, followed by CFD methods in the 1980's.

Eventually, analytical methods progressed, first with unsteady extensions of momentum theory, and subsequently with adaptations of Kinner's circular-wing theory for the lifting-rotor. This research, extending over more than 40 years, came to be known as finite-state, or dynamic inflow theory, and appeared in ever-increasingly sophisticated forms for various rotorcraft applications, Ref.[9].

The first simple dynamic inflow theories were based on either simple momentum theory or basic vortex-wing analogies, Refs.[10]-[13]. Although sophisticated work on the mathematical theory of lifting airscrews had appeared in the Russian literature by 1973, Ref.[14], this work did not find practical application for dynamic inflow theories in the U.S. A significant advance by Pitt and Peters, Ref.[15], extended the work of Mangler and Squire and included the unsteady inflow for the first-harmonic loading functions. Modern dynamic inflow theory is based on solutions of the linear, incompressible, potential flow equations for the unsteady flow-field induced by an arbitrarily loaded circular disk in either axial or oblique flow. Extensions of the Pitt-Peters theory to an arbitrary number of radial and azimuthal loading functions yielded the Peters-He Generalized Dynamic Wake Theory, Ref.[16]. The correspondence between dynamic inflow theory and the classical potential flow rotor theories of Goldstein and Loewy (Refs.[3] and [17]) has been established in Refs.[16], [18], and [19]. A more complete and rigorous theory has been developed recently by Peters, Morrillo, Hsieh, and Garcia-Duffy, Refs.[20]-[23]. The early emphasis on dynamic inflow theory was aimed first at rotor response characteristics and then at applications to aeroelastic stability and flight control models. More recently, dynamic inflow has found acceptance for rotor loads analysis and for application to rotor performance, especially for fundamental investigations and applications for lifting-rotor induced-power in both axial and forward flight conditions.

It may be useful to clarify actuator disk terminology at this point. An actuator disk is a disk that supports a pressure jump across the rotor disk that can also vary with

radius, azimuth, and time. Thus an actuator disk can have either an infinite or a finite number of blades. Steady actuator disk theory implies an infinite number of blades while a time varying actuator disk theory implies a finite number. Thus, Peters-He finite-state inflow is an actuator disk model in its original form. In contrast, propeller theory has the lift vector inclined with respect to the disk which implies induced swirl velocity in the wake and so is not an actuator disk. However, propeller theory can include either an infinite or finite number of blades. Goldstein applied the Betz condition for both a finite number of blades and an infinite number of blades. The Makinen adaptation of the Peters-He theory is propeller theory since lift inclination and swirl velocity are included. Garcia-Duffy treated all four cases: finite and infinite blade number for the actuator disk and a propeller. Finally, the lightly-loaded rotor assumes that the influence of the wake induced flow-field on the wake geometry is either small or is neglected.

1.3 Previous Work

1.3.1 Historical Landmarks

Recent research has afforded major new advancements in one of the most fundamental and traditional disciplines of rotorcraft—aerodynamics and performance of the lifting rotor. This research is intended to continue this progress with significant new developments. Dynamic inflow models have been demonstrated to be useful for the optimization of rotor power in axial flow, Ref.[19]. The models result in a classic quadratic optimization problem that can be used to find optimum loading and induced flow for minimum power. Results have been shown to agree with classic propeller solutions of Betz, Prandtl, and Goldstein, Ref.[23]. Reference [23] also shows that finite-state wake models might be used to optimize rotor performance is skewed flow (i.e., forward flight). In this document, it will be shown how the finite-state framework can be used in classical optimization for rotors in forward flight—even with side constraints on the loading and with limitations on blade geometry.

1.3.2 Recent Interest in Induced-Power

The subject of lifting rotor induced-power dates back to Glauert in the mid-1920s, and his classical uniform inflow theory has been widely used ever since. However, it fails to capture the important influence of non-uniform inflow at moderate and high advance ratios and this has limited understanding of the significance of induced-power for advanced rotorcraft. It has been noticed by Harris, Ref.[24], that the induced-power consumed by conventional helicopters can be six to ten times as great as the minimum power predicted by Glauert. Ref.[24] questions why the induced-power is so large. Ormiston, Ref.[25], uses the Government code called "Rotorcraft Comprehensive Analysis System" (RCAS) with dynamic inflow to determine part of the answer to this important question. His results show that nonuniform inflow and the trim state have a profound effect on the induced-power. The recent work of Hall and Hall [26] verifies that there is a significant induced-power penalty at moderate and high advance ratios and provides additional new insight about lifting rotor induced-power. Reference [27] applies the finite-state method on induced-power calculations for a rotor with an infinite number of blades. Building on these advances, dynamic wake theory offers a very promising new means of attacking the problem—through simple, closed-form power formulas that can be derived from the finite-state inflow equations. In this work these models will be used for exactly that purpose. Both the development of the formulation for induced-power efficiency and the numerical results yield insight into this phenomenon.

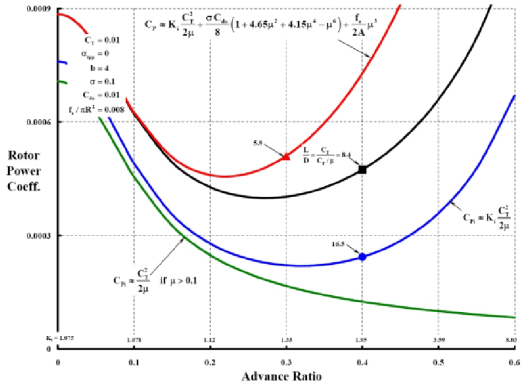

Figure 1.1: Power coefficient data from Harris investigation illustrating the divergence of power.

1.4 Optimum Power

Several rotorcraft researchers have addressed the question of optimum induced-power in hover and forward flight. In hover, or axial flight condition, the earliest is the classical work of Betz and Goldstein noted above. More recently, Hall et al, Ref.[28], use a novel numerical method and linear optimization to verify Goldstein's axial flow optimal loading result for a four-bladed rotor. This is discussed further below. Peters and Makinen (Refs.[18] and [29]) apply finite-state dynamic inflow theory to the optimum loading condition for lightly-loaded rotors of Betz and Goldstein. Since dynamic inflow is based on linear potential theory for the pressure discontinuity across an "actuator disk," the theory was extended in those references to include both the inclination of the blade lift normal to the local flow direction—See Figure 1.2—and the implicit wake induced swirl velocity to reproduce the classical results of Betz for the infinite-blade rotor and of Goldstein for the finite-bladed rotor. Peters and Garcia-Duffy (Ref.[30]) use dynamic inflow to determine the optimum induced-power for actuator disks and propellers for a finite number of blades as a function of thrust coefficient and axial advance ratio.

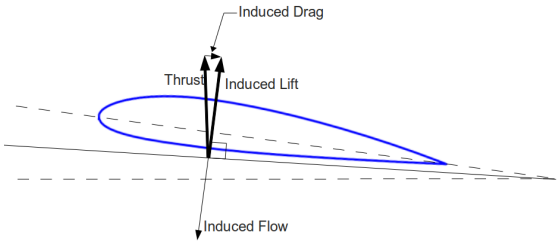

Figure 1.2: Graphic depiction of the induced air loads on a rotor blade airfoil section.

A number of researchers have addressed optimum induced-power for a lifting-rotor in forward flight. These include Moffitt and Bissell, Ref.[31]; Quackenbush et al, Ref.[32]; Hall et al, Ref.[28]; Rand et al, Ref.[33], Ormiston, Ref.[34], and Wachspress et al, Ref.[35]. All of these treat rotors with a finite number of blades. The most rigorous of these, by Hall et al, uses a discrete wake comprised of helical vortex lattice sheets to model a lightly-loaded, four-bladed rotor in forward flight. A wake energy method based on a Trefftz volume—analogous to the classical Trefftz plane method—is used to evaluate the rotor induced-power in the far field. The rotor blade bound circulation loading is discretized as a function of azimuth and radius and linear quadratic optimization is applied, with appropriate lift and rotor moment constraints, to determine the optimum loading and associated induced-power. Although useful steps

forward, these investigations produced relatively limited results and few significant insights about optimum rotor induced-power in forward flight.

Garcia-Duffy et al, Ref.[36], in a precursor to the present investigation, uses an analytical approach and dynamic inflow to determine the optimum induced-power for an untrimmed rotor in oblique flow. The rotor model is for an infinite number of blades, and includes inclination of the lift vector and swirl effects. The oblique flow condition defined by wake skew angle encompasses the full range of operating conditions from axial to an edgewise rotor in forward flight. The rotor is not trimmed to a constrained rotor hub moment condition (e.g., zero moment) and the induced-power for the edgewise flow condition is equal to the Glauert ideal minimum for all advance ratios. The induced-power is shown to increase for increased rotor disk angles of attack and converges to the results of Ref.[30] for axial flow.

In 2010, Hall and Hall, Ref.[26], use the methodology introduced in Ref.[28] to significantly extend the initial lightly-loaded rotor results to a full range of advance ratios, number of blades, and multiple rotor and wing configurations (the latter are significant but beyond the scope of the present single rotor investigation). Significant new insights are obtained, particularly regarding blade number, wake skew angle, and rotor moment trim. These results were interpreted in terms of the configuration of the trailed and shed vorticity in the far wake. Most importantly, for large blade numbers, the optimum induced-power converges to the Glauert ideal for a rotor disk at zero angle-of-attack. For the trimmed rotor with a finite number of blades, the optimum normalized induced-power increases substantially and peaks near the critical advance ratio similar to the corresponding Ormiston's results.

1.5 Present Approach

There are several distinct areas of interest for the induced-power of the lifting-rotor. The first is to better understand fundamental characteristics of induced-power, especially in high-speed forward flight. Also to evolve analytical models to predict induced-power for arbitrary configurations and operating conditions. Finally, determine the optimum induced-power in forward flight subject to arbitrary constraints while properly accounting for the complex wake induced flow-field. Finite-state wake

inflow theory offers a very promising new analytical method of attacking the problem of lifting-rotor induced-power with the potential to derive simple, closed-form expressions from the finite-state inflow equations and provide new fundamental insight about induced-power. The focus of the present research is to address lifting-rotor performance in forward flight for the general loading conditions and apply the methods to the optimization for minimum induced-power subject to arbitrary constraints.

Chapter 2

Dynamic Inflow Theory

To adequately formulate a mathematical model from the physical system, a summary of dynamic inflow theory is in order.

2.1 Fundamentals of Fluid Dynamics

From basic fluid dynamics, the conservation equations for an incommpressible, potential flow are written as follows:

$$\vec{\nabla} \cdot \vec{V} = 0 \tag{2.1}$$

$$\frac{\partial \vec{V}}{\partial t} + (\vec{V} \cdot \vec{\nabla})\vec{V} = -\frac{1}{\varrho}\vec{\nabla}p \tag{2.2}$$

where $\vec{V}$ is the total velocity, ϱ is the air density, and p is the flow field pressure. If one assumes small perturbations—i.e., the total velocity $\vec{V}$ differs only slightly from the free-stream V_∞—then the total velocity may be expressed as the following:

$$\vec{V} = -V_\infty \cdot \hat{\xi} + \delta\vec{v} \tag{2.3}$$

Where ξ is a vector (non-dimensional on R—the rotor radius) along the streamline pointing in the upstream direction (opposite the direction of flow, see Figure 2.1) and $\delta\vec{v}$ is a small perturbation velocity.

$$\hat{\xi} = \sin(\chi)\hat{i} - \cos(\chi)\hat{k} \tag{2.4}$$

$$\delta\vec{v} = \delta\vec{v}_x\hat{i} + \delta\vec{v}_y\hat{j} + \delta\vec{v}_z\hat{k} \tag{2.5}$$

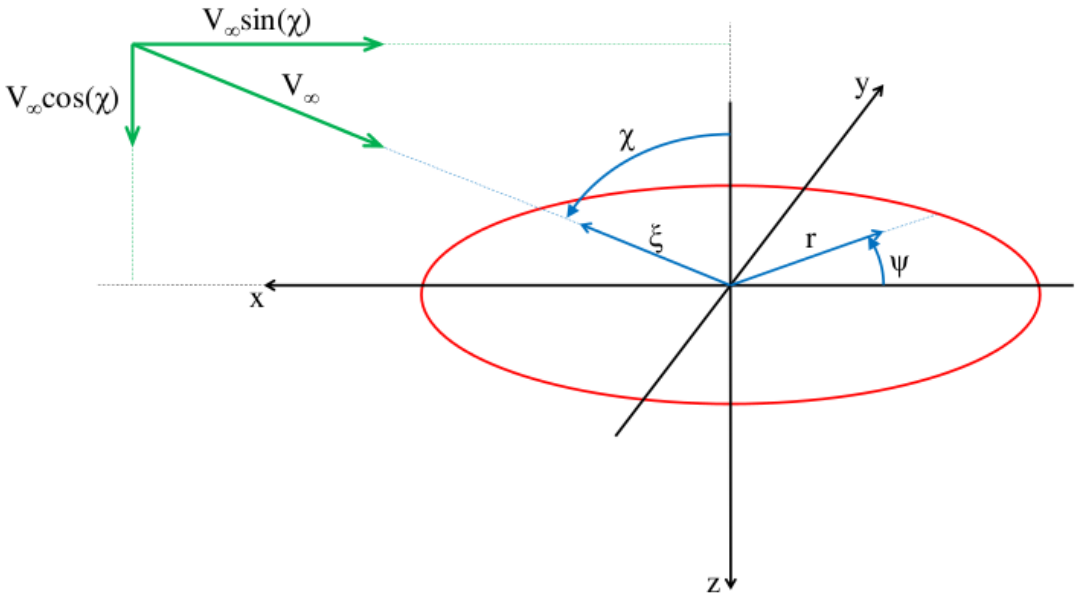

Figure 2.1: Graphic depiction of rotor coordinates with accompanying free-stream.

Substitution of Eqs.((2.3)-(2.5)) into Eq.(2.2) and dropping higher order terms yields the following equation.

$$\frac{\partial\delta\vec{v}}{\partial t} - V_\infty\frac{\partial\delta\vec{v}}{\partial\xi} = -\frac{1}{\varrho}\vec{\nabla}p \tag{2.6}$$

This is a linearized form of the original momentum equations. If one defines a set of non-dimensional parameters, the linearized momentum equations may then become non-dimensional as well.

$$\vec{v} \equiv \frac{\delta\vec{v}}{\Omega R} \tag{2.7}$$

$$P \equiv \frac{p}{\varrho\Omega^2R^2} \tag{2.8}$$

$$\bar{t} \equiv t\cdot\Omega \tag{2.9}$$

where Ω is the rotor rotational speed.

This gives the following set of equations for the continuity of mass and momentum, respectively.

$$\vec{\nabla}\cdot\vec{v} = 0 \tag{2.10}$$

$$\frac{\partial\vec{v}}{\partial\bar{t}} - \frac{\partial\vec{v}}{\partial\xi} = -\vec{\nabla}P \tag{2.11}$$

Next, if one assumes that the non-dimensional velocity $\vec{v}$ can be expressed as the gradient of some potential function, say Ψ. Then the velocity may be expressed as the following.

$$\vec{v} = \vec{\nabla}\Psi \tag{2.12}$$

which then gives for the continuity of mass equations.

$$\vec{\nabla}^2\Psi = 0 \tag{2.13}$$

If the potential function Ψ is substituted into the momentum equations and then one pre-multiplies a divergence to this, the momentum equation reduces to Laplace's equation.

$$\frac{\partial(\vec{\nabla}^2\Psi)}{\partial\bar{t}} - \frac{\partial(\vec{\nabla}^2\Psi)}{\partial\xi} = -\vec{\nabla}^2 P = 0 \tag{2.14}$$

This implies that the non-dimensional pressure P may be expressed as a potential function as well, say Φ.

$$P = \Phi \tag{2.15}$$

We may now solve for the non-dimensional pressure distribution from Eq.(2.14). It is convenient to model the inflow of a helicopter rotor in Ellipsoidal coordinates[1]. Therefore, Laplace's equation, when written in Ellipsoidal coordinates, is as follows.

$$\frac{\partial}{\partial\nu}\left[(1-\nu^2)\frac{\partial\Phi}{\partial\nu}\right] + \frac{\partial}{\partial\eta}\left[(1+\eta^2)\frac{\partial\Phi}{\partial\eta}\right] + \frac{\partial}{\partial\psi}\left[\frac{(\nu^2+\eta^2)}{(1-\nu^2)(1+\eta^2)}\frac{\partial\Phi}{\partial\psi}\right] = 0 \tag{2.16}$$

The solution to this equation is a function of associated Legendre functions[2].

$$\Phi(\nu,\eta,\psi) = \sum_{n,m} \bar{P}_n^m(\nu)\bar{Q}_n^m(i\eta)\left(C_1\cos(m\psi) + C_2\sin(m\psi)\right) \tag{2.17}$$

where $\bar{P}_n^m(\nu)$ and $\bar{Q}_n^m(\eta)$ are normalized associated Legendre functions of the first and second kind, respectively. ν is the coordinate that represents hyperboloids which, on the rotor disk, is given by $\nu = \sqrt{1-\bar{r}^2}$. η is a coordinate that represents ellipsoids. And ψ is the azimuthal angle measured from rotor aft.

[1]Refer to Appendix A for detailed explanation.
[2]Refer to Appendix B for detailed explanation.

It is important to note that the pressure potential defined in Eq.2.17 must satisfy the boundary conditions present on the rotor disk. In the ellipsoidal coordinate system, ν changes sign as it crosses the rotor disk from the upper hemisphere to the lower—and vice versa. Therefore a solution to the pressure potential must account for this. Associated Legendre function are defined such that the sum of m and n even represent and even function in $\bar{P}_n^m$ and likewise the sum of m and n being odd represent an odd function in $\bar{P}_n^m$. Thus the only permissible terms are those with $m+n$ equals odd, all other terms are zero.

2.2 Linear Operators

Returning to the linearized equations in 2.6, one may express the pressure distribution as a combination of two parts—a part due to convection Φ^V and a part due to unsteadiness Φ^A.

$$\Phi = \Phi^V + \Phi^A \tag{2.18}$$

This may then be differentiated as follows:

$$\vec{\nabla}\Phi = \vec{\nabla}\Phi^V + \vec{\nabla}\Phi^A \tag{2.19}$$

where, from Eq.2.6,

$$\vec{\nabla}\Phi^V = V_\infty \frac{\partial \delta\vec{v}}{\partial \xi} \tag{2.20}$$

$$\vec{\nabla}\Phi^A = -\frac{\partial \delta\vec{v}}{\partial t} \tag{2.21}$$

Because the focus of concern is the normal component of the perturbation velocity on the surface of the rotor disk (i.e., z-component at $\xi = 0$), one may integrate Eq.2.20 along a streamline taking into account only the component normal to the disk.

$$\frac{\partial \delta\vec{v}}{\partial \xi} = w = \frac{1}{V_\infty}\int_0^\infty \frac{\partial \Phi^V}{\partial z} d\xi \tag{2.22}$$

Here, w is known as the normal component of the induced-flow, considered positive in the downward direction. Likewise, the non-dimensional time derivative of the unsteadiness perturbation component may be expressed as follows:

$$\frac{\partial \delta \vec{v}}{\partial \bar{t}} = \frac{dw}{d\bar{t}} = -\frac{\partial \Phi^A}{\partial z}|_{\eta=0} \tag{2.23}$$

The two above equations may be thought of as linear operators,

$$w = L[\Phi^V] \tag{2.24}$$

$$\frac{dw}{d\bar{t}} = M^{-1}[\Phi^A] \tag{2.25}$$

where both operators L and M are expressible in matrix form as well as invertible. This is possible by an appropriate choice of expansion functions for the representation of the induced-flow. In a similar fashion as the pressure distribution (Eq.2.17), one may expand the induced-flow distribution in the following way.

$$w(\bar{r}, \psi, \bar{t}) = \sum_{j,r} \bar{\Psi}^r_j(\bar{r}) \left(a^r_j(\bar{t}) \cos(r\psi) + b^r_j(\bar{t}) \sin(r\psi) \right) \tag{2.26}$$

This is represented in terms of a harmonic variation in the azimuthal angle and an arbitrary (i.e., yet to be determined) radial distribution. Here the expansion function $\bar{\Psi}^r_j(\bar{r})$ must be linearly independent and complete for a given harmonic r. Also, the coefficients $a^r_j(\bar{t})$ and $b^r_j(\bar{t})$ may be considered as the time-dependent states of the induced-flow model.

2.3 Finite-State Equations

When one choses appropriate expansion functions for the induced flow distribution, numerical convergence is optimized[42]. In particular, these expansion functions are the following.

$$\Psi^r_j = \phi^r_j(\bar{r}) \equiv \frac{1}{\nu} \bar{P}^r_j(\nu) \tag{2.27}$$

The expansion functions $\phi_j^r(\bar{r})$ turn out to be simple polynomials in $\bar{r}$.

$$\phi_j^r(\bar{r}) = \sqrt{((2j+1)H_j^r)} \sum_{q=r,r+2,\cdots}^{j-1} \bar{r}^q \frac{(-1)^{(q-r)/2}(j+q)!!}{(q-r)!!\,(q+r)!!\,(j-q-1)!!} \tag{2.28}$$

where

$$H_n^m = \frac{(n+m-1)!!\,(n-m-1)!!}{(n+m)!!\,(n-m)!!} \tag{2.29}$$

From the development of the Peters-He model, the following matrices will result from the aforementioned expansion functions.

$$B_{jn}^r = \bar{B}_{jn}^r \equiv \int_0^1 \bar{P}_n^r(\nu)\frac{1}{\nu}\bar{P}_n^r(\nu)d\nu \tag{2.30}$$

Due to the complex nature of the computation of $\bar{B}_{jn}^r$, it is often found beneficial to use the simpler inverse.

$$\left[\bar{B}_{jn}^r\right]^{-1} = \frac{(-1)^{\frac{n+j-2r}{2}}}{\sqrt{H_n^r H_j^r}} \frac{2\sqrt{2n+1}\sqrt{2j+1}}{(n+j)(n+j+2)((n-j)^2-1)} \tag{2.31}$$

Therefore, the final form of the dynamic wake model, using the expansions $\Psi_j^r = \phi_j^r(\bar{r})$, is as follows.

$$\begin{bmatrix} [M^c] & 0 \\ 0 & [M^s] \end{bmatrix} \begin{Bmatrix} \dot{\{\alpha\}} \\ \{\beta\} \end{Bmatrix} + V \begin{bmatrix} [\tilde{L}^c]^{-1} & 0 \\ 0 & [\tilde{L}^s]^{-1} \end{bmatrix} \begin{Bmatrix} \{\alpha\} \\ \{\beta\} \end{Bmatrix} = \frac{1}{2} \begin{Bmatrix} \{\tau^c\} \\ \{\tau^s\} \end{Bmatrix} \tag{2.32}$$

where, in the Peters-He generalized dynamic wake model

$$[M^c] = [M^s] = \begin{bmatrix} \ddots & & \\ & K_n^m & \\ & & \ddots \end{bmatrix} \tag{2.33}$$

where $K_n^m \equiv \frac{\pi}{2} H_n^m$, and

$$[\tilde{L}^c] = \begin{bmatrix} \ddots & & \\ & [\bar{B}_{jn}^r]^{-1} & \\ & & \ddots \end{bmatrix} \begin{bmatrix} & \vdots & \\ \cdots & [\hat{L}_{jn}^{rm}]^c & \cdots \\ & \vdots & \end{bmatrix} \tag{2.34}$$

And likewise, a similar expression exists for $[\tilde{L}^s]$.

The elements of the induced flow influence coefficient matrices $[\hat{L}_{jn}^{rm}]$ are expressed as follows.

$$\begin{aligned} \left[\hat{L}_{jn}^{0m}\right]^c &= X^m [\Gamma_{jn}^{0m}] \\ \left[\hat{L}_{jn}^{rm}\right]^c &= \left[X^{|m-r|} + (-1)^l X^{|m+r|}\right] [\Gamma_{jn}^{rm}] \\ \left[\hat{L}_{jn}^{rm}\right]^s &= \left[X^{|m-r|} - (-1)^l X^{|m+r|}\right] [\Gamma_{jn}^{rm}] \end{aligned} \tag{2.35}$$

where $l = \min(r, m)$ and $X = \tan(|\frac{\chi}{2}|)$. Also, the functions Γ_{jn}^{rm} are defined by the following equations.

for $r + m$ even,

$$\Gamma_{jn}^{rm} = \frac{(-1)^{\frac{n+j-2r}{2}}}{\sqrt{H_n^m H_j^r}} \frac{2\sqrt{(2n+1)(2j+1)}}{(j+n)(j+n+2)((j-n)^2-1)}$$

for $r + m$ odd, $j = n \pm 1$,

$$\Gamma_{jn}^{rm} = \frac{\pi}{2\sqrt{H_n^m H_j^r}} \frac{\text{sgn}(r-m)}{\sqrt{(2n+1)(2j+1)}} \tag{2.36}$$

for $r + m$ odd, $j \neq n \pm 1$,

$$\Gamma_{jn}^{rm} = 0$$

Chapter 3

Aerodynamic Theory

3.1 Induced-Inflow Model

The starting point of this development is the computation of power based on finite-state variables. The induced power (i.e., the work done on the flow) of a rotor can be defined from fundamental physics. This is the time-average of the integration over the disk of the product of induced velocity, force per unit area, and unit area.

$$\text{Power} = \int_T \iint_A (\text{Force} \times \text{velocity})\, dA d\bar{t} \tag{3.1}$$

where T is the time domain of interest—here 1 period—and A is the surface area (2-D) of the rotor disk.

In keeping with the scope of this research, it will be convenient to non-dimensionalize the above with the following relationship.

$$C_P \equiv \frac{\text{Power}}{\pi R^2 \varrho (\Omega R)^2 (\Omega R)} \tag{3.2}$$

The power integral in Eq.(3.1) then becomes the following.

$$C_P = \frac{1}{2\pi} \int_0^{2\pi} \iint_A (\Delta P(\bar{r}, \psi, \bar{t}) \cdot w(\bar{r}, \psi, \bar{t}))\, \bar{r} d\bar{r} d\psi d\bar{t} \tag{3.3}$$

where $w(\bar{r}, \psi, \bar{t})$ is the induced velocity and $\Delta P(\bar{r}, \psi, \bar{t})$ is the net force per unit area. To evaluate this integral, knowledge of w and P are needed. The Peters-He induced

flow theory is a natural place from which to develop this idea, Refs.[43] and [44]. The non-dimensional induced flow distribution in that model is represented by an expansion in velocity coefficients.

$$w(\bar{r},\psi,\bar{t}) = \sum_n \left(\alpha_n^0(\bar{t})\frac{\bar{P}_n^0(\nu)}{2\nu}\right) + \sum_{n,m}\left(\alpha_n^m(\bar{t})cos(m\psi) + \beta_n^m(\bar{t})sin(m\psi)\right)\frac{\bar{P}_n^m(\nu)}{\nu} \tag{3.4}$$

The expansion coefficients α_n^m, β_n^m are partitioned in terms of a superscript m that denotes the harmonic number and a subscript n that denotes the radial expansion for each harmonic number. Also, the zero harmonic terms $(\alpha_n^0(\bar{t}))$ are defined in the following manner.

$$\alpha_n^0(\bar{t}) = 2a_n^0(t)|_{He} \tag{3.5}$$

where $a_n^0(\bar{t})|_{He}$ are the inflow states from the Peters-He model, Ref.[43]. The reason for this will be evident in the coming derivation of induced power.

The non-dimensional pressure across the rotor disk in the He model is also expanded in a similar partition of normalized Legendre functions.

$$\Delta P(\bar{r},\psi,\bar{t}) = 2\left[\sum_n\left(\tau_n^{0c}(\bar{t})\bar{P}_n^0(\nu)\right) + \sum_{n,m}\left(\tau_n^{mc}(\bar{t})cos(m\psi) + \tau_n^{ms}(\bar{t})sin(m\psi)\right)\bar{P}_n^m(\nu)\right] \tag{3.6}$$

where the τ's are pressure expansion coefficients.

Both the velocity coefficients and the pressure coefficients are expanded in harmonics of blade number. For example,

$$\alpha_n^m(\bar{t}) = \alpha_{n0c}^m + \sum_{k=Q,2Q,\ldots}\left(\alpha_{nkc}^m \cdot cos(k\bar{t}) + \alpha_{nks}^m \cdot sin(k\bar{t})\right) \tag{3.7}$$

A similar expansion will exist for α_n^0, β_n^m, τ_n^{0c}, τ_n^{mc}, and τ_n^{ms}. The subscripts c, s represent cosine and sine expansions in non-dimensional time $(\bar{t})$, and the superscripts c, s represent spatial (ψ) cosine and sine expansions—as demonstrated in Eqs.(3.4) and (3.6).

It follows—due to the orthogonality of the basis functions—that the induced power coefficient (Eq.(3.3)), can be written in a very compact form:

$$C_P = \frac{1}{2\pi} \int_0^{2\pi} \{\tau\}^T \{\alpha\} \, d\bar{t} \tag{3.8}$$

where, for the sake of brevity, $\{\alpha\}$ represents the total inflow solution and likewise $\{\tau\}$ the total pressure expansion.

3.2 Finite-State Inflow Model

When the pressure and velocity expansions are substituted into the momentum equations, the following dynamic wake model is produced.

$$\begin{bmatrix} [M^c] & 0 \\ 0 & [M^s] \end{bmatrix} \begin{Bmatrix} \dot{\{\alpha\}} \\ \{\beta\} \end{Bmatrix} + V \begin{bmatrix} [\bar{L}^c]^{-1} & 0 \\ 0 & [\bar{L}^s]^{-1} \end{bmatrix} \begin{Bmatrix} \{\alpha\} \\ \{\beta\} \end{Bmatrix} = \frac{1}{2} \begin{Bmatrix} \{\tau^c\} \\ \{\tau^s\} \end{Bmatrix} \tag{3.9}$$

where the mass matrix $[M]$ and the influence coefficient matrix $[\bar{L}]$ are closed form expressions from the development of the dynamic wake model. Also, note that the influence coefficient matrix $[\bar{L}^c]$ is a modified form of the matrix found in the Peters-He model.

$$[\bar{L}^c] = \begin{bmatrix} 2[I] & & & \\ & [I] & & \\ & & [I] & \\ & & & \ddots \end{bmatrix} [\tilde{L}^c] \tag{3.10}$$

which states that the zero harmonic terms are doubled, all other terms remain unaffected. This follows from the factor of 2 in Eq.(3.5). However, $[\bar{L}^s] = [\tilde{L}^s]$ as in the Peters-He model.

Since the inflow distribution is considered unsteady with blade passage, a solution for the inflow includes a summation of harmonics. Also, due to the time derivative of the inflow states—which are comprised of sines and cosines—the solutions to the above differential equations are coupled and include terms of both $[M]$ and $[\bar{L}]$. The general solution is the sum of the steady and unsteady solutions. For the steady-state

solution, the inflow states are as follows:

$$\left\{ \begin{array}{c} \{\alpha_n^m\}_c \\ \{\beta_n^m\}_c \end{array} \right\}_0 = \frac{1}{2V} \left[\begin{array}{cc} [\bar{L}^c] & 0 \\ 0 & [\bar{L}^s] \end{array} \right]_0 \left\{ \begin{array}{c} \{\tau_n^{mc}\}_c \\ \{\tau_n^{ms}\}_c \end{array} \right\}_0 \tag{3.11}$$

and the unsteady inflow contributions are

$$\left\{ \begin{array}{c} \left\{ \begin{array}{c} \{\alpha_n^m\}_c \\ \{\alpha_n^m\}_s \end{array} \right\} \\ \left\{ \begin{array}{c} \{\beta_n^m\}_c \\ \{\beta_n^m\}_s \end{array} \right\} \end{array} \right\}_k = \frac{1}{2V} \left[\begin{array}{cc} [\mathscr{L}^c] & 0 \\ 0 & [\mathscr{L}^s] \end{array} \right]_k \left\{ \begin{array}{c} \left\{ \begin{array}{c} \{\tau_n^{mc}\}_c \\ \{\tau_n^{mc}\}_s \end{array} \right\} \\ \left\{ \begin{array}{c} \{\tau_n^{ms}\}_c \\ \{\tau_n^{ms}\}_s \end{array} \right\} \end{array} \right\}_k \tag{3.12}$$

where k takes on integer multiples of the number of blades (i.e., $k = Q, 2Q, 3Q, ...$). The matrices $[\mathscr{L}]_k$ are defined below from the coupled momentum equations,

$$[\mathscr{L}^c]_k = \left[\begin{array}{cc} [\bar{L}^c]^{-1} & \frac{k}{V}[M^c] \\ -\frac{k}{V}[M^c] & [\bar{L}^c]^{-1} \end{array} \right]^{-1} = \left[\begin{array}{cc} [N^c]_k & -\frac{k}{V}[N^c]_k[M^c][\bar{L}^c] \\ \frac{k}{V}[\bar{L}^c][M^c][N^c]_k & [N^c]_k \end{array} \right] \tag{3.13}$$

where

$$[N^c]_k \equiv \left[[\bar{L}^c]^{-1} + (\frac{k}{V})^2 [M^c][\bar{L}^c][M^c] \right]^{-1} \tag{3.14}$$

Similar expressions exists for $[\mathscr{L}^s]_k$ and likewise $[N^s]_k$.

Therefore, general solutions to the momentum equations (3.9) are the sum of all solutions and are defined below.

$$\begin{aligned} \{\alpha_n^m(\bar{t})\} =& \frac{1}{2V}[\bar{L}^c]\{\tau_n^{mc}\}_{0c} \\ &+ \sum_{k=Q,2Q,...} \left(\frac{1}{2V} \left[\begin{array}{cc} cos(k\bar{t}) & 0 \\ 0 & sin(k\bar{t}) \end{array} \right] [\mathscr{L}^c]_k \left\{ \begin{array}{c} \{\tau_n^{mc}\}_{kc} \\ \{\tau_n^{mc}\}_{ks} \end{array} \right\} \right) \end{aligned} \tag{3.15}$$

$$\begin{aligned} \{\beta_n^m(\bar{t})\} =& \frac{1}{2V}[\bar{L}^s]\{\tau_n^{ms}\}_{0c} \\ &+ \sum_{k=Q,2Q,...} \left(\frac{1}{2V} \left[\begin{array}{cc} cos(k\bar{t}) & 0 \\ 0 & sin(k\bar{t}) \end{array} \right] [\mathscr{L}^s]_k \left\{ \begin{array}{c} \{\tau_n^{ms}\}_{kc} \\ \{\tau_n^{ms}\}_{ks} \end{array} \right\} \right) \end{aligned}$$

3.3 Formulation of Induced Power

From the inflow solutions in Eq.(3.15) and the pressure coefficients expanded in temporal harmonics—as in Eq.(3.7)—the induced power coefficient is expressed as a summation as well.

$$C_P = \left\{ \begin{array}{c} \{\tau^c\} \\ \{\tau^s\} \end{array} \right\}_{0c}^T \left\{ \begin{array}{c} \{\alpha\} \\ \{\beta\} \end{array} \right\}_{0c} + \frac{1}{2} \sum_k \left(\left\{ \begin{array}{c} \left\{ \begin{array}{c} \{\tau^c\}_c \\ \{\tau^c\}_s \end{array} \right\}_k \\ \left\{ \begin{array}{c} \{\tau^s\}_c \\ \{\tau^s\}_s \end{array} \right\}_k \end{array} \right\}^T \left\{ \begin{array}{c} \left\{ \begin{array}{c} \{\alpha\}_c \\ \{\alpha\}_s \end{array} \right\}_k \\ \left\{ \begin{array}{c} \{\beta\}_c \\ \{\beta\}_s \end{array} \right\}_k \end{array} \right\} \right) \tag{3.16}$$

where, here, the sines and cosines have been averaged over the time-domain and the factor of 2 in Eq.(3.5) cancels the 1/2 from the sinusoidal average.

With the solution to the inflow states in terms of the pressure expansion coefficients, one can now place the power coefficient in a quadratic form in terms of these pressure expansion coefficients.

$$\begin{aligned} C_P = & \frac{1}{2V} \left\{ \begin{array}{c} \{\tau_n^{mc}\} \\ \{\tau_n^{ms}\} \end{array} \right\}^T \left[\begin{array}{cc} [\bar{L}^c] & 0 \\ 0 & [\bar{L}^s] \end{array} \right] \left\{ \begin{array}{c} \{\tau_n^{mc}\} \\ \{\tau_n^{ms}\} \end{array} \right\} \\ & + \frac{1}{2} \sum_k \left(\frac{1}{2V} \left\{ \begin{array}{c} \left\{ \begin{array}{c} \{\tau_n^{mc}\}_c \\ \{\tau_n^{mc}\}_s \end{array} \right\} \\ \left\{ \begin{array}{c} \{\tau_n^{ms}\}_c \\ \{\tau_n^{ms}\}_s \end{array} \right\} \end{array} \right\}_k^T \left[\begin{array}{cc} [\mathscr{L}^c] & 0 \\ 0 & [\mathscr{L}^s] \end{array} \right]_k \left\{ \begin{array}{c} \left\{ \begin{array}{c} \{\tau_n^{mc}\}_c \\ \{\tau_n^{mc}\}_s \end{array} \right\} \\ \left\{ \begin{array}{c} \{\tau_n^{ms}\}_c \\ \{\tau_n^{ms}\}_s \end{array} \right\} \end{array} \right\}_k \right) \end{aligned} \tag{3.17}$$

In Eq.(3.17), $[\bar{L}]$ depends only on one parameter, the wake skew angle χ, and $[\mathscr{L}]_k$ depends on the wake skew angle χ, the mass flow parameter V, and the number of blades Q.

For the special case of an infinite number of blades, the above summation may be reduced by noting that the original dynamic wake (Eq.(3.9)) model becomes steady. Therefore, the solution to the inflow states is reduced to Eq.(3.11). The coefficient of

power is reduced to the following.

$$C_P = \frac{1}{2V} \left\{ \begin{array}{c} \{\tau_n^{mc}\} \\ \{\tau_n^{ms}\} \end{array} \right\}^T \left[\begin{array}{cc} [\bar{L}^c] & 0 \\ 0 & [\bar{L}^s] \end{array} \right] \left\{ \begin{array}{c} \{\tau_n^{mc}\} \\ \{\tau_n^{ms}\} \end{array} \right\} \tag{3.18}$$

Chapter 4

General Rotor Performance Formulation

4.1 Rotor Loads

General rotor performance theory encompasses rotor loads as well as induced-power. Rotor loads in turn are also utilized as the constraints that define optimum induced-power. The dynamic inflow formulation may be used to compute any desired rotor loads. Here we consider rotor loads to be integrals over the disk of the pressure including appropriate weighting functions. We will now express rotor loads in terms of the pressure loading coefficients $\{\tau\}$. Consider, for example, rotor thrust, roll moment, and pitching moment, three common rotor loads. Rotor thrust is defined as the integration of the force per unit area times a unit area of the rotor disk over the surface of the rotor.

$$\text{Thrust} = \iint_A (\text{Force}) dA \tag{4.1}$$

Whereas, the moment loads are defined as the force per unit area times a "moment arm" times the unit area of the rotor disk over the surface of the rotor.

$$\text{Moment} = \iint_A (\text{Force} \times \text{X}) dA \tag{4.2}$$

Thrust is defined as the net force exerted on the rotor, normal to the plane of the disk. In the rotorcraft industry, two standard moments are considered. These are referred to as roll moment and pitch moment. Roll moment is considered a side-to-side force

and pitch moment is considered a fore-to-aft force. A positive roll moment is defined as advancing blade downward. Whereas a positive pitch moment is defined as "nose" up[3]. Figure 4.1 illustrates this with moment arrows representing the roll moment L and pitch moment M as viewed from above the rotor disk. In this diagram, the z-axis is positioned at the origin (standard Cartesian coordinates) and pointing into the page—i.e., away from the reader—giving a valid right-hand coordinate system.

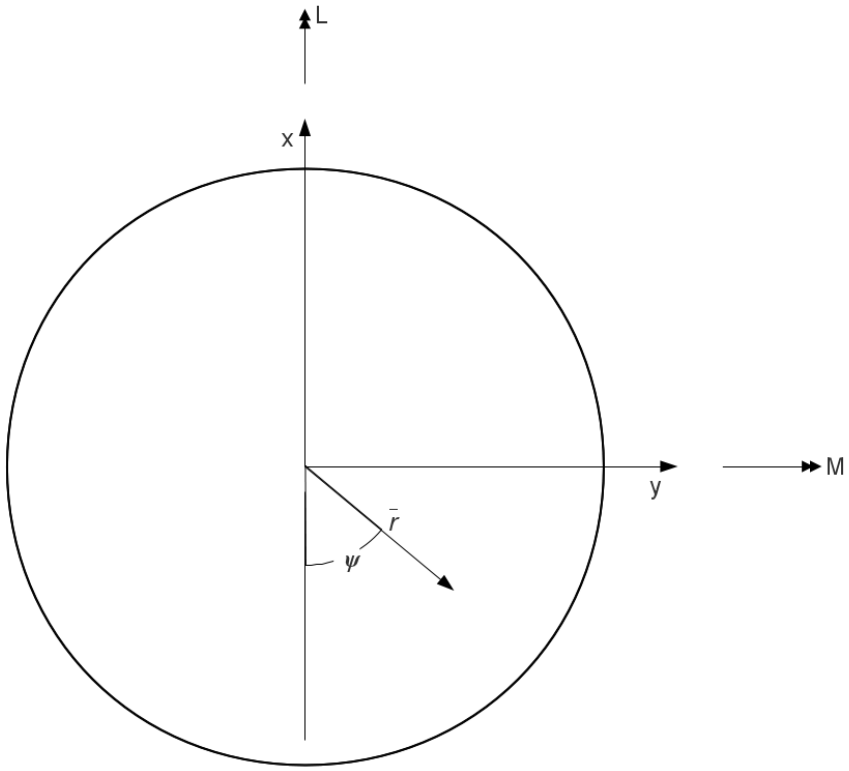

Figure 4.1: Graphic depiction of the rotor moments as viewed from above (looking in the downward direction) the rotor disk.

[3]The nose of a rotor is typically associated with the nose (or front) of a helicopter fuselage. However, in the general case this simply refers to the leading edge of the rotor in foward flight conditions.

We will non-dimensionalize these loads to determine the loading coefficients.

$$
\begin{aligned}
C_T &\equiv \frac{\text{Thrust}}{\pi R^2 \varrho (\Omega R)^2} \\
C_L &\equiv \frac{\text{Roll Moment}}{\pi R^2 \varrho (\Omega R)^2 R} \\
C_M &\equiv \frac{\text{Pitch Moment}}{\pi R^2 \varrho (\Omega R)^2 R}
\end{aligned}
\tag{4.3}
$$

Here C_T is the non-dimensional thrust coefficient, C_L is the non-dimensional roll moment coefficient, and C_M is the non-dimensional pitch moment coefficient.

These load coefficients are defined by the following integrals of the pressure loading.

$$
\begin{aligned}
C_T &= \frac{1}{\pi} \int_0^{2\pi} \int_0^1 \Delta P \cdot \cos(\varphi) \cdot \bar{r} \cdot d\bar{r} d\psi \\
C_L &= -\frac{1}{\pi} \int_0^{2\pi} \int_0^1 \Delta P \cdot \cos(\varphi) \left(\bar{r} \cdot \sin(\psi)\right) \bar{r} \cdot d\bar{r} d\psi \\
C_M &= -\frac{1}{\pi} \int_0^{2\pi} \int_0^1 \Delta P \cdot \cos(\varphi) \left(\bar{r} \cdot \cos(\psi)\right) \bar{r} \cdot d\bar{r} d\psi
\end{aligned}
\tag{4.4}
$$

where $\cos(\varphi)$ is the cosine of the angle between the lift and thrust vectors. An animated diagram of a blade section is shown in Figure 1.2. It is shown how the induced drag positions the lift vector away from the thrust vector which is perpendicular to the rotor disk. This *tilting* of the lift vector induces a net rotational force that drives the wake to rotate, or swirl, as is trails the rotor disk. More on the topic of swirl will be discussed in Section 8.1.

A direct consequence of the lift inclination is that the lift is then positioned perpendicular to the trailing vortex sheets. These sheets are parallel to the total local velocity U.

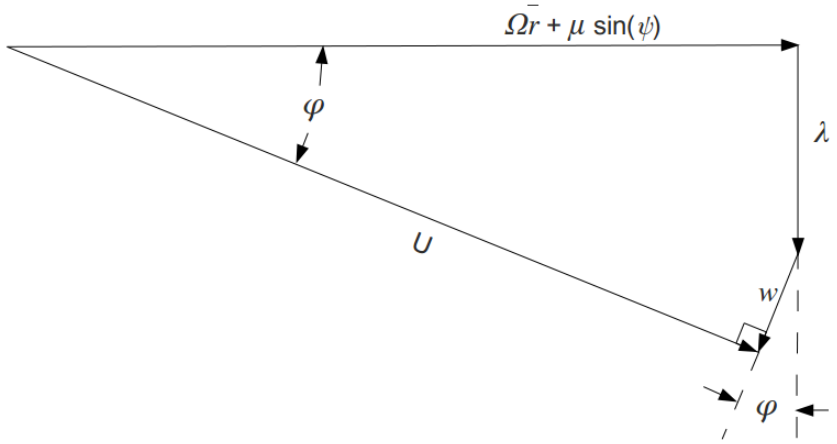

Figure 4.2: Graphic depiction of the induced flow w and subsequent total inflow U.

4.2 Matrix Representation

If one expands $\nu \cos(\varphi)$ in a series of Legendre functions,

$$\nu \cos(\varphi) = \sum_{m,n} \left(D_n^{mc} \cos(m\psi) + D_n^{ms} \sin(m\psi) \right) \bar{P}_n^m(\nu) \tag{4.5}$$

or more aptly,

$$\cos(\varphi) = \sum_{m,n} \left(D_n^{mc} \cos(m\psi) + D_n^{ms} \sin(m\psi) \right) \frac{1}{\nu} \bar{P}_n^m(\nu) \tag{4.6}$$

One may also express the following in Legendre functions.

$$-\bar{r} \cos(\varphi) \cos(\psi) = \sum_{m,n} \left(D_{nc}^{mc} \cos(m\psi) + D_{nc}^{ms} \sin(m\psi) \right) \frac{1}{\nu} \bar{P}_n^m(\nu) \tag{4.7}$$

$$-\bar{r} \cos(\varphi) \sin(\psi) = \sum_{m,n} \left(D_{ns}^{mc} \cos(m\psi) + D_{ns}^{ms} \sin(m\psi) \right) \frac{1}{\nu} \bar{P}_n^m(\nu) \tag{4.8}$$

The thrust, roll moment, and pitch moment coefficients may then be expressed as an inner product of the pressure expansion coefficients and the Legendre-function

expansions defined above.

$$C_T = 2\{\tau_n^{0c}\}^T\{D_n^{0c}\}_0 + \{\tau_n^{mc}\}^T\{D_n^{mc}\}_0 + \{\tau_n^{ms}\}^T\{D_n^{ms}\}_0 \tag{4.9}$$

$$C_L = 2\{\tau_n^{0c}\}^T\{D_n^{0c}\}_c + \{\tau_n^{mc}\}^T\{D_n^{mc}\}_c + \{\tau_n^{ms}\}^T\{D_n^{ms}\}_c \tag{4.10}$$

$$C_M = 2\{\tau_n^{0c}\}^T\{D_n^{0c}\}_s + \{\tau_n^{mc}\}^T\{D_n^{mc}\}_s + \{\tau_n^{ms}\}^T\{D_n^{ms}\}_s \tag{4.11}$$

After substituting the pressure loading of the Peters-He theory from Eq.(3.6) and integrating, the rotor loads are readily expressible in terms of the pressure loadings where the othogonality of the basis functions become utilized. Written in matrix form, they are of the form:

$$\left\{ \begin{array}{c} C_n^{0c} \\ C_n^{mc} \\ C_n^{ms} \end{array} \right\} = \left[\begin{array}{c|c|c} \{\cdots D_n^{0c} \cdots\}_0 & \{\cdots D_n^{mc} \cdots\}_0 & \{\cdots D_n^{ms} \cdots\}_0 \\ \hline \{\cdots D_n^{0c} \cdots\}_c & \{\cdots D_n^{mc} \cdots\}_c & \{\cdots D_n^{ms} \cdots\}_c \\ \hline \{\cdots D_n^{0c} \cdots\}_s & \{\cdots D_n^{mc} \cdots\}_s & \{\cdots D_n^{ms} \cdots\}_s \end{array} \right] \left\{ \begin{array}{c} \tau_n^{0c} \\ \tau_n^{mc} \\ \tau_n^{ms} \end{array} \right\} \tag{4.12}$$

Here the vectors $\{D\}_0$, $\{D\}_c$, and $\{D\}_s$ are the matrix representations of the integration of the mode shape functions. They are detailed below and are a Legendre-function representations of $\nu\cos(\varphi)$ Ref.[23].

$$\begin{aligned} \{D_n^{0c}\}_0 &= \frac{1}{2\pi}\int_0^{2\pi}\int_0^1 \cos(\varphi)\bar{P}_n^0(\nu)\nu d\nu d\psi \\ \{D_n^{mc}\}_0 &= \frac{1}{\pi}\int_0^{2\pi}\int_0^1 \cos(\varphi)\bar{P}_n^m(\nu)\nu d\nu \cos(m\psi)d\psi \\ \{D_n^{ms}\}_0 &= \frac{1}{\pi}\int_0^{2\pi}\int_0^1 \cos(\varphi)\bar{P}_n^m(\nu)\nu d\nu \sin(m\psi)d\psi \end{aligned} \tag{4.13}$$

$$
\begin{aligned}
\{D_n^{0c}\}_c &= \frac{1}{2\pi}\int_0^{2\pi}\int_0^1 \cos(\varphi)\bar{P}_n^0(\nu)\nu d\nu\cos(\psi)d\psi \\
\{D_n^{mc}\}_c &= \frac{1}{\pi}\int_0^{2\pi}\int_0^1 \cos(\varphi)\bar{P}_n^m(\nu)\nu d\nu\cos(\psi)\cos(m\psi)d\psi \\
\{D_n^{ms}\}_c &= \frac{1}{\pi}\int_0^{2\pi}\int_0^1 \cos(\varphi)\bar{P}_n^m(\nu)\nu d\nu\cos(\psi)\sin(m\psi)d\psi
\end{aligned}
\tag{4.14}
$$

$$
\begin{aligned}
\{D_n^{0c}\}_s &= \frac{1}{2\pi}\int_0^{2\pi}\int_0^1 \cos(\varphi)\bar{P}_n^0(\nu)\nu d\nu\sin(\psi)d\psi \\
\{D_n^{mc}\}_s &= \frac{1}{\pi}\int_0^{2\pi}\int_0^1 \cos(\varphi)\bar{P}_n^m(\nu)\nu d\nu\sin(\psi)\cos(m\psi)d\psi \\
\{D_n^{ms}\}_s &= \frac{1}{\pi}\int_0^{2\pi}\int_0^1 \cos(\varphi)\bar{P}_n^m(\nu)\nu d\nu\sin(\psi)\sin(m\psi)d\psi
\end{aligned}
\tag{4.15}
$$

where, for a lightly-loaded rotor,

$$
\cos(\varphi) = \frac{\Omega\bar{r} + \mu\sin(\psi)}{\sqrt{(\Omega\bar{r} + \mu\sin(\psi))^2 + \lambda^2}} \tag{4.16}
$$

This can be verified by inspection of Figure 4.2.

If we neglect the tilting of the lift vector (i.e., $\cos(\varphi) \approx 1$) the loads defined in Eqs.(4.4) reduce to the following closed-form equations.

$$
\left\{\begin{array}{c} C_T \\ C_M \\ C_L \end{array}\right\} = \left[\begin{array}{c|c|c} \frac{2}{\sqrt{3}} & 0 & 0 \\ \hline 0 & -\frac{2}{\sqrt{15}} & 0 \\ \hline 0 & 0 & -\frac{2}{\sqrt{15}} \end{array}\right] \left\{\begin{array}{c} \tau_1^{0c} \\ \tau_2^{1c} \\ \tau_2^{1s} \end{array}\right\} = [D]\{\tau\} \tag{4.17}
$$

This example may be extended to formulate any desired rotor loads. One may therefore write the general loading vector $\{C\}$ in the form:

$$\{C\} = [D]\{\tau\} \tag{4.18}$$

where $[D]$ is a closed-form matrix based on integrals of the inflow shape functions. The $J \times 1$ loading vector $\{C\}$ defines the J rotor loads, and the matrix $[D]$ has J rows and N columns that define the combination of pressure coefficients that form each rotor load. The only limitation is that $1 \leq J \leq N$ since only N loads are defined in this theory. For the optimization problem, any of the rotor loads may be used as constraints to define the optimum induced-power. Typically these include the rotor thrust and moments developed in Eq.(4.17) or other loads (e.g., higher harmonic loads).

The above analysis of loads implicitly assumes that the loading is perpendicular to the rotor disk. As pointed out in Refs.[29] and [36], the true loading is inclined with respect to the disk plane (i.e., the lift is perpendicular to the local air velocity vector). If any of the loads (for example C_T) need to be computed based on the normal component of lift, Ref.[36] shows that this effect can be formally included in the above derivation. The analysis is fairly straightforward. The direction cosine of the lift inclination over the disk is expanded in a series of Legendre functions and harmonic functions—as is pressure in Eq.(3.6)—and the direction cosine expansion coefficients are placed into the elements of $[D]$.

Chapter 5

Rotor Pitch Controls

There are at least two methods of developing a model for the pressure loadidngs of the lifting rotor. One is by means of describing the blade lift in terms of pitch control. Another method is to model the circulation of each blade. Both approaches allow for an optimum solution and both approaches will be examined here. In this chapter the focus will remain on blade pitch and the next chapter will describe blade circulation.

5.1 Pressure Loading in Terms of Rotor Controls

We will now extend the development in order to express first the rotor pressure loading, and then, the rotor loads, in terms of rotor controls. This is needed for general performance and for more convenient application of rotor loads as constraints for optimization. Rotor controls are those variables that define the operation of the rotor system in terms of performance and induced-power. Examples are collective pitch, linear twist, cyclic pitch, higher-harmonic control, variable airfoil geometry, or even circulation control via local blowing. These variables may be either fixed or time-varying. Along with rotor blade geometry (e.g., radial chord distribution), the control variables influence the blade loading and thus affect the unsteady pressure-loading coefficients of dynamic inflow. Any conventional, non-conventional, or hypothetical control can be defined within a vector of allowable blade controls $\{\theta\}$.

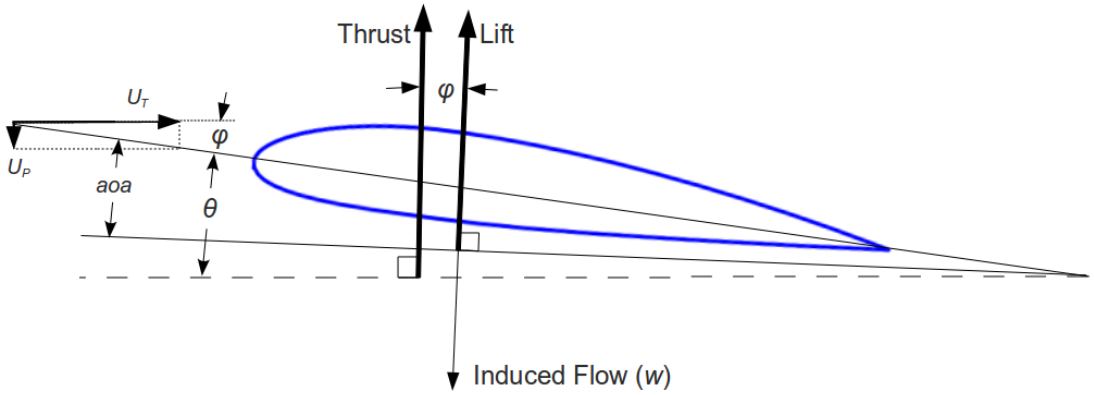

Figure 5.1: Graphic depiction of the pitch angle relative to the rotor disk plane and the blade section chord.

For the purposes of this research, we will restrict the rotor control vector $\{\theta\}$ to be comprised of harmonics of blade azimuthal pitch and blade radial twist

$$\theta(\bar{r}, \psi_q) = \sum_{k=0}^{K} \sum_{m=0}^{M} \left[\bar{r}^k \left[\theta_k^{mc} \cdot cos(m\psi_q) + \theta_k^{ms} \cdot sin(m\psi_q)\right]\right] \tag{5.1}$$

where M is the maximum harmonic of azimuthal pitch and K is the maximum power of $\bar{r}$ of the blade twist. Therefore, the number of defined controls is a function of the radial expansion and harmonic number.

$$H = (K+1)(2M+1) \tag{5.2}$$

It follows that the allowable pressure loading coefficients across the rotor disk are no longer the complete set of $\{\tau_n^m\}$ of Eqs.(3.17) and (4.4) but rather only those blade loadings that can be generated through the rotor controls $\{\theta\}$. In the language of formal optimization, this implies a constraint on the allowable τ's.

The relationship between the controls and the corresponding allowable pressure loading coefficient vector may be found from conventional blade-element theory. The underlying methodology is given in Refs.[43] and [44] and is explained below.

The rotor disk pressure expansion coefficients are defined in terms of the blade lift per unit length, $\mathscr{L}_q$, and the radial shape functions ϕ_n^m defined in Eq.(2.27):

$$\begin{aligned}
\tau_n^{0c} &= \tfrac{1}{2\pi} \sum_{q=1}^{Q} \left[\int_0^1 \tfrac{\mathscr{L}_q}{\varrho \Omega^2 R^3} \phi_n^0(\bar{r}) d\bar{r} \right] \\
\tau_n^{mc} &= -\tfrac{1}{\pi} \sum_{q=1}^{Q} \left[\int_0^1 \tfrac{\mathscr{L}_q}{\varrho \Omega^2 R^3} \phi_n^m(\bar{r}) d\bar{r} \right] cos(m\psi_q) \\
\tau_n^{ms} &= -\tfrac{1}{\pi} \sum_{q=1}^{Q} \left[\int_0^1 \tfrac{\mathscr{L}_q}{\varrho \Omega^2 R^3} \phi_n^m(\bar{r}) d\bar{r} \right] sin(m\psi_q)
\end{aligned} \tag{5.3}$$

Where $\mathscr{L}_q$ is the blade lift per unit length of the 2-D airfoil section of the q^{th} blade based on conventional blade-element theory,

$$\mathscr{L}_q = \frac{1}{2} \varrho a c \left(U_T^2 \cdot \theta_q - U_P \cdot U_T \right) \tag{5.4}$$

where U_T and U_P are the tangential and perpendicular components of velocity at the blade section.

$$\begin{aligned}
U_T &= \Omega R \left(\bar{r} + \mu \cdot sin(\psi_q) \right) \\
U_P &= \Omega R \left(\lambda + w(\bar{r}, \psi_q) \right)
\end{aligned} \tag{5.5}$$

Note how the induced flow, itself, affects the $\{\tau\}$ loads giving an effect of induced-flow feedback.

The above blade-element result gives the lift perpendicular to the disk under the potential flow relation that lift coefficient is proportional to $sin(angle\ of\ attack)$ with no small-angle assumptions except that $cos(\theta) \approx 1.0$ and $sin(\theta) \approx \theta$. There are no small-angle assumptions on U_T and U_P. It follows that:

$$\begin{aligned}
\left\{ \begin{array}{c} \tau_n^{0c} \\ \tau_n^{mc} \\ \tau_n^{ms} \end{array} \right\} = & \frac{\sigma a}{2} \int_0^1 \left([\bar{r} + \mu sin(\psi)]^2 \theta(\bar{r}, \psi) \phi_n^m \right) d\bar{r} \cdot \left\{ \begin{array}{c} \frac{1}{2} \\ cos(m\psi) \\ sin(m\psi) \end{array} \right\} \\
& - \frac{\sigma a}{2} \int_0^1 \left([\bar{r} + \mu sin(\psi)][\lambda + w] \phi_n^m \right) d\bar{r} \cdot \left\{ \begin{array}{c} \frac{1}{2} \\ cos(m\psi) \\ sin(m\psi) \end{array} \right\}
\end{aligned} \tag{5.6}$$

With $w = w(\bar{r}, \psi)$ written from Eq.(3.4), the integrations of Eq.(5.6) yield the following:

$$\{\tau\} = \frac{\sigma a}{4}\left[[A]\{\theta\} - [B]\left\{\begin{array}{c} 2\alpha_n^0 \\ \alpha_n^m \\ \beta_n^m \end{array}\right\}\right] \tag{5.7}$$

where the matrix $[A]$ represents the effect of the controls on $\{\tau\}$, and $[B]$ represents the effect of the resultant induced flow on both angle-of-attack and $\{\tau\}$. Discussion and details of $[A]$ and $[B]$ are presented in AppendixE. The effect of λ on $\{\tau\}$ is a fixed loading and is not included in Eq.(5.7).

The rotor solidity and lift curve slope enter the formulation of $[A]$ and $[B]$ due to a summation over the number of blades that involves chord and lift coefficients from blade-element theory. Thus, $[A]$ and $[B]$ then depend on advance ratio; and they can be simplified by multi-blade identities. Here $[A]$ is $N \times H$ and $[B]$ is $N \times N$, where H is the number of rotor controls, N is the number of included states, and J is the number of loading constraints. The vector of controls $\{\theta\}$ is $H \times 1$. There are no limitations on the number of controls except that $1 \leq J \leq H \leq N$ such that there are at least enough controls to effect the loading constraints. The rows of both $[A]$ and $[B]$ and the columns of $[B]$ are partitioned in the normal way in terms of superscripts and subscripts.

It is clear that the controls, the pressure loads, and the induced inflow are all coupled together. However, these interdependencies are fully expressed in the previous equations, e.g., inflow is given in terms of the pressure loadings $\{\tau\}$ in Eq.(3.15) and $\{\tau\}$ in terms of the controls and inflow in Eq.(5.7). Therefore, a formal solution for the pressure loading coefficients solely in terms of the rotor controls may be obtained from these equations to yield:

$$\{\tau\} = \frac{\sigma a}{4}\left[[I] + \frac{\sigma a}{8V}[B][\bar{L}]\right]^{-1}[A]\{\theta\} = [P]\{\theta\} \tag{5.8}$$

where

$$[P] \equiv \frac{\sigma a}{4}\left[[I] + \frac{\sigma a}{8V}[B][\bar{L}]\right]^{-1}[A] \tag{5.9}$$

The rows of $[P]$ follow the m, n partitioning system. One can see that the effect of the inflow feedback is characterized by the factor $\frac{\sigma a}{8V}$. It can be shown that, in axial

flow, $[\bar{L}] = [B]^{-1}$ so that the leading matrix becomes the well-known equivalent Lock number factor $[1 + \frac{\sigma a}{8V}]^{-1}$. In skewed flow, the effect is more involved but still driven by $\frac{\sigma a}{8V}$.

If fact, the effect of inflow feedback can be much smaller than the term $\frac{\sigma a}{8V}$. As noted above, in axial flow the entire effect is a factor of $[1 + \frac{\sigma a}{8V}]^{-1}$. This factor simply rescales the $\{\theta\}$ controls and has no effect on the optimum. The only effect of inflow feedback on the optimum is $\frac{\sigma a}{8V}$ multiplied by the deviation of $[B][\bar{L}]$ from $[I]$. Thus, the effect on the optimum is null both in axial flow and in high-speed flight (V large); and one may often neglect it in performing as optimization, as will be done in the results here.

For the sake of brevity, $[P]$, in Eq.(5.8), represents the $N \times H$ matrix that defines completely how the controls translate into the admissible values of disk loadings. For $H = J$ and where $[A]$ is a matrix of full rank, one can obtain any combination of desired $\{\tau\}$ with some combination of $\{\theta\}$ so that neither the $[A]$ matrix, the $[B]$ matrix, nor σa affects the optimum.

5.2 Rotor Loads in Terms of Rotor Controls

The previous sections outlined the derivation of rotor induced-power based on finite-state induced flow theory in terms of the rotor loading coefficients$\{\tau_n^m\}$. Expressions for the basic integrated rotor loadings (thrust, roll moment, and pitching moment) were also derived in terms of the rotor loading coefficients. That is, they were given as special cases of arbitrary loading constraints that must be applied in an optimization process. Finally, the rotor loading coefficients were expressed in terms of rotor controls; and these were defined so as to encompass conventional collective and cyclic pitch control. These results may now be combined to produce the final formulation for the general performance of a lifting-rotor. These results will also be used to cast rotor performance as a classical, quadratic optimization problem.

We proceed by substitution of Eq.(5.8) into Eq.(4.18) to yield:

$$\{C\} = [D][P]\{\theta\} \tag{5.10}$$

For the case where $\{C\}$ is comprised of the rotor thrust and moments, this becomes:

$$\left\{ \begin{array}{c} C_T \\ C_L \\ C_M \end{array} \right\} = [D][P]\{\theta\} \tag{5.11}$$

Similarly, by substituting Eq.(5.8) into the steady solution for a rotor with an infinite number of blade (Eq.(3.18)) one obtains, for the coefficient of power, the following relation.

$$C_P = \frac{1}{2V}\{\theta\}^T[P]^T[\bar{L}][P]\{\theta\} \tag{5.12}$$

Chapter 6

Blade Circulation

In this chapter the focus will be describing the pressure loadings and then the rotor loads in terms of the circulation.

6.1 Pressure Loading in Terms of Circulation

In order to represent the loadings $\{\tau\}$ and, hence, rotor power C_P in terms of blade circulation, we now apply blade-element theory. The lift per unit length per blade $\mathscr{L}_q$ is written in terms of standard airfoil theory with the lift coefficient $C_{\mathscr{L}}$ proportional to the sine of the angle of attack.

$$C_{\mathscr{L}} = a \sin(aoa) \tag{6.1}$$

which is the exact result of 2-D potential flow theory.

One may now determine the loadings on the rotor as an expression of the lift, which are given in terms of tip speed ΩR and nondimensional radial position $\bar{r}$.

$$\left\{ \begin{array}{c} \tau_n^{0c} \\ \tau_n^{mc} \\ \tau_n^{ms} \end{array} \right\} = 2 \sum_{q=1}^{Q} \int_0^1 \bar{\mathscr{L}_q} \phi_n^m(\bar{r}) d\bar{r} \left\{ \begin{array}{c} \frac{1}{2} \\ \cos(m\psi_q) \\ \sin(m\psi_q) \end{array} \right\} \tag{6.2}$$

where

$$\bar{\mathscr{L}_q} = \frac{\mathscr{L}_q}{2\pi\varrho(\Omega R)^2 R} \tag{6.3}$$

is the non-dimensional form of the lift per unit length per blade, Q is the total number of blades, and ϕ_n^m is defined as the following polynomial.

$$\phi_n^m(\bar{r}) \equiv \frac{1}{\nu}\bar{P}_n^m(\nu) \tag{6.4}$$

If one defines the lift as an expansion in harmonics of Legendre functions, similar to what was done with the pitch angle:

$$\bar{\mathscr{L}}_q \equiv \frac{\bar{r}}{Q}\sum_{m,n}\left(\gamma_n^{mc}\cos(m\psi_q) + \gamma_n^{ms}\sin(m\psi_q)\right)\bar{P}_n^m \tag{6.5}$$

where γ_n^m are the circulation coefficients. This, then, permits the blade loadings to be expressed in a very simplified form.

$$\left\{\begin{array}{c}\tau_n^{0c}\\ \tau_n^{mc}\\ \tau_n^{ms}\end{array}\right\} = 2\sum_{q=1}^{Q}\int_0^1 \bar{\mathscr{L}}_q\bar{P}_n^m\frac{d\bar{r}}{\nu}\left\{\begin{array}{c}\frac{1}{2}\\ \cos(m\psi_q)\\ \sin(m\psi_q)\end{array}\right\} \tag{6.6}$$

The above integral can be evaluated by substitution of the following matrix:

$$\left[T_{nj}^{mr}\right] \equiv \int_0^1 \bar{P}_n^m(\bar{r})\bar{P}_j^r(\bar{r})d\bar{r} \tag{6.7}$$

where

$$\left[T_{nj}^{mm}\right] = [\delta_{nj}] = [I] \tag{6.8}$$

This gives a closed form expression for the blade loadings in terms of the circulation.

$$\left\{\begin{array}{c}\tau_n^{mc}\\ \tau_n^{ms}\end{array}\right\}_k = \left[\begin{array}{cc}[T^c]_k & 0\\ 0 & [T^s]_k\end{array}\right]\left\{\begin{array}{c}\gamma_j^{rc}\\ \gamma_j^{rs}\end{array}\right\}_k \tag{6.9}$$

where the matrices $[T^c]$ and $[T^s]$ are defined from the orthogonality matrix Eq.(6.7)[4].

$$[T^c]_k \equiv \left[\begin{array}{cc}[T^{cc}]_k & [0]\\ [0] & [T^{cs}]_k\end{array}\right] \tag{6.10}$$

[4]Refer to Appendix E for detailed explanation of $[T]$.

and

$$[T^s]_k \equiv \begin{bmatrix} [0] & [T^{ss}]_k \\ [T^{sc}]_k & [0] \end{bmatrix} \tag{6.11}$$

Here, the superscripts (i.e., cs) indicate if a zero harmonic term is included and the subscript k defines the allowed harmonics.

6.2 Rotor Loads in Terms of Circulation

We will follow the example of Sec.5.2 by substitution of Eq.(6.9) into Eq.(4.18) to yield:

$$\{C\} = [D][T]\{\gamma\} \tag{6.12}$$

For the case where $\{C\}$ is comprised of the rotor thrust and moments, this becomes:

$$\begin{Bmatrix} C_T \\ C_L \\ C_M \end{Bmatrix} = [D][T]\{\gamma\} \tag{6.13}$$

To simplify the expression for the power coefficient, one may define a new matrix, say $[R]$, as the representation of the summation of influence coefficients over all values of k.

$$[R] \equiv \begin{bmatrix} [\bar{L}^c] & 0 \\ 0 & [\bar{L}^s] \end{bmatrix} + \frac{1}{2V} \sum_k \left\{ \begin{bmatrix} [T^{cc}]_k & [0] \\ [0] & [T^{cs}]_k \end{bmatrix}^T [\mathscr{L}^c] \begin{bmatrix} [T^{cc}]_k & [0] \\ [0] & [T^{cs}]_k \end{bmatrix} \right. \\ \left. + \begin{bmatrix} [0] & [T^{ss}]_k \\ [T^{sc}]_k & [0] \end{bmatrix}^T [\mathscr{L}^s] \begin{bmatrix} [0] & [T^{ss}]_k \\ [T^{sc}]_k & [0] \end{bmatrix} \right\} \tag{6.14}$$

where, again, the summation of the unsteady influence contributions is over the integer multiples of the number of blades, i.e., $k = Q, 2Q, 3Q, \cdots$.

This allows the expression for the power coefficient to be compact and succinct. Therefore, the summation expressed in Eq.(3.17) becomes an inner product.

$$C_P = \frac{1}{2V}\{\tau\}^T[R]\{\tau\} \tag{6.15}$$

Here the τ's are implied to contain both the sine and cosine contributions of the pressure expansions. This efficient expression is convenient due to the symmetry of the matrix multiplication and will be utilized in the later optimization procedures.

It should be noted that the above power coefficient is given in terms of an arbitrary number of blades. This is due to the matrix $[R]$ which includes the effects of finite blade number. If the coefficient of power were to be computed for the special case of an infinite number of blades, Eq.(6.14) would reduce to the first term only. This would reduce the power coefficient to the special case of

$$C_P = \frac{1}{2V}\{\tau\}^T[\bar{L}]\{\tau\} \tag{6.16}$$

Chapter 7

Performance Optimization

7.1 General Rotor Loads

From the previous two chapters we have expressions for C_T, C_L, C_M, and C_P directly in terms of the rotor control variables—either pitch controls or circulation. These results provide rotor induced-power for any arbitrary loading condition, as defined by any arbitrary rotor control inputs. Moreover, these results provide the basis for a completely general rotor performance theory, that is, an analytical formulation for all six components of the integrated rotor loads (i.e., the thrust, H-force, side force, roll and pitch moments, and shaft torque). While only three of these are included in Eqs.(5.11) and (6.13), the development is easily extended to include the other three. [Note that the induced-power in Eq.(5.12) encompasses two of the remaining three load components (i.e., the rotor shaft torque and the drag component of the thrust and H-forces)].

Such a general rotor performance theory is notable in that it provides the thrust and power that explicitly reflects the complexity of the non-uniform inflow of the lifting-rotor. It provides a general analytical formulation for performance based entirely on first principles. Heretofore, such models have been available only for simple uniform induced inflow, (i.e., classical theory) developed by Wheatley, Bailey, and others, Refs.[45]-[49] or in recent refinements for high advance ratio by Harris, Ref.[25].

The power model of Refs.[39], [25], and [41] is similar to the present formulation, specifically Eqs.(5.11) and (5.12), and it embodies non-uniform inflow. However, it is much less general, contains only three fixed controls, and the constants are derived

from numerical calculations of finite-state inflow theory (although an arbitrary finite number of blades may be included and reversed flow is included).

We now address the main focus of this research, the determination of the optimum, or minimum, induced power of the lifting-rotor with constraints on the loads. Up until now, the pressure loading coefficients $\{\tau\}$, the rotor controls $\{\theta\}$, and the circulation $\{\gamma\}$ were not constrained. However, the induced power may only be optimized when appropriate loading constraints are applied. Otherwise, the optimum of Eq.(3.17) would simply be $C_P = 0$. The most basic constraint is to specify a non-zero value for rotor lift since induced power is a consequence of the generation of lift. Typically, the objective is to determine the minimum induced power for a specified value of lift. In addition there may be other constraints characterized in terms of rotor loads (e.g., a rotor typically operates in moment trim and generates a specified propulsive force). In addition, specific higher-harmonic blade pitch and variable twist controls may be included. Therefore, the optimization problem will include these as constraints; the controls are allowable controls; the $\{\tau\}$'s are allowable $\{\tau\}$'s; and the rotor loads $\{C\}$ define the specified rotor lift and trim operating conditions.

7.2 Quadratic Optimization

With the above, one may formulate the computation of given power under loading constraints in terms of a functional F. This is done by an augmentation of the induced power coefficient C_P with the inner product of the constraints and Lagrange multipliers, Λ, yielding,

$$F = C_P - \{C\}^T\{\Lambda\} \tag{7.1}$$

Substitution from Eqs.(6.15) and (4.18), yields a functional in terms of the pressure expansion coefficients.

$$F(\tau) = \frac{1}{2V}\{\tau\}^T[R]\{\tau\} - \{\tau\}^T[D]^T\{\Lambda\} \tag{7.2}$$

where $\{\Lambda\}$ is the $J \times 1$ column of Lagrange multipliers that are used to match the constraints. Note that the first term in this functional is the power coefficient proper, and the second term is the augmentation with constraints on the pressure loading.

It must be noted that the below optimization may be attempted with either a controls constraint $[P]\{\theta\}$ or by constraining the circulation $[T]\{\gamma\}$. Therefore, to keep the generalization concise, a new vector, say $\{Y\}$, will be defined to represent either the controls or the circulation. Also, the transformation matrices to map either the controls or the circulation to the loads will also be redefined to, say $[G]^T$. Therefore,

$$\{\tau\} = [G]^T\{Y\} \tag{7.3}$$

will be the vector of pressure loading coefficients.

In order to express the augmented power functional in terms of the constraints on the allowable controls or circulation, Eq.(7.3) may be substituted into Eq.(7.2). The constrained optimization problem has the final functional as below.

$$F(Y) = \frac{1}{2V}\{Y\}^T[R]\{Y\} - \{Y\}^T[G]\{\Lambda\} \tag{7.4}$$

Because the loading constraints are fixed at the desired values $\{C\}$, the variation of $F(Y)$ set equal to zero will give the optimality condition for C_P.

$$\delta F(Y) = \frac{1}{V}\{\delta Y\}^T[R_s]\{Y\} - \{\delta Y\}^T[G]\{\Lambda\} = 0 \tag{7.5}$$

where $[R_s]$ is the symmetric portion of $[R]$.

Immediately, one can solve for the optimum control settings in terms of the Lagrange multipliers.

$$\{Y\} = V[R_s]^{-1}[G]\{\Lambda\} \tag{7.6}$$

The Lagrange multipliers are then set so as to enforce the loading constraints.

$$\{C\} = 2V[G]^T[R_s]^{-1}[G]\{\Lambda\} \tag{7.7}$$

$$\{\Lambda\} = \frac{1}{2V}[[G]^T[R_s]^{-1}[G]]^{-1}\{C\} = \frac{1}{2V}[Q]^{-1}\{C\} \tag{7.8}$$

where

$$[Q] \equiv \left[[G]^T[R_s]^{-1}[G]\right] \tag{7.9}$$

is a symmetric matrix. When combined with Eqs.(7.3) and (7.6), the above gives the optimum loading distribution.

$$\{\tau\} = \frac{1}{2}[R_s]^{-1}[G][Q]^{-1}\{C\} \tag{7.10}$$

The optimum C_P then can be found from Eqs.(3.17), (7.9), and (7.10). Matrix manipulation (along with the definition of $[Q]$) results in a simplified expression for the optimum C_P.

$$(C_P)_{opt} = \frac{1}{2V}\{C\}^T[Q]^{-1}[[G]^T(R_s)^{-1}[G]][Q]^{-1}\{C\} = \frac{1}{2V}\{C\}^T[Q]^{-1}\{C\} \tag{7.11}$$

Thus, all information about the optimum power is contained in $[Q]$ from Eq.(7.9).

7.3 Induced Power Efficiency

It is known from Glauert that the minimum possible power is given by

$$(C_P)_{ideal} = \frac{C_T^2}{2V} \tag{7.12}$$

One can normalize the above relation by dividing both sides by C_T^2.

$$\left(\frac{C_P}{C_T^2}\right)_{ideal} = \frac{1}{2V} \tag{7.13}$$

This is the classic Glauert minimum.

We define the Induced Power Ratio (IPR) as the ratio of optimum power (for a constrained case above) divided by the minimum Glauert induced power. Since Glauert power depends on C_T , one must assume that the vector of desired loadings $\{C\}$ is proportional to C_T. We therefore define the normalized loading vector as,

$$\{\zeta\} = \frac{1}{C_T}\{C\} \tag{7.14}$$

which is scaled against C_T. The optimum power (Eq.(7.11)) can then be divided by C_T^2 to obtain a formula for computing this power with the scaled constraints.

$$\left(\frac{C_P}{C_T^2}\right)_{opt} = \frac{1}{2V}\{\zeta\}^T[Q]^{-1}\{\zeta\} \tag{7.15}$$

One can then take a ratio of the optimum power (with constraints on the available controls/circulation and loads) divided by the Glauert minimum to get the IPR.

$$IPR \equiv \frac{(C_P/C_T^2)_{opt}}{(C_P/C_T^2)_{ideal}} = \{\zeta\}^T[Q]^{-1}\{\zeta\} \tag{7.16}$$

We may also describe an efficiency ε_{IP} of the induced-power for the lifting rotor by defining a ratio of the minimum Glauert induced power divided by the optimum power (again, for a constrained case above). This is also the same as the inverse of the induced-power ratio.

$$\varepsilon_{IP} \equiv \frac{(C_P/C_T^2)_{ideal}}{(C_P/C_T^2)_{opt}} = \frac{1}{IPR} = \left[\{\zeta\}^T[Q]^{-1}\{\zeta\}\right]^{-1} \tag{7.17}$$

The induced-power efficiency ε_{IP} is always a number between 0 and 1. The vector $\{\zeta\}$ and each of the matrices in $[Q]$ represents the effect of a given physical variable on the induced power efficiency. It may be noted that the ε_{IP} is analogous to the Figure of Merit used as a measure of efficiency of a rotor in the hover condition.

For a general rotor configuration a description of each matrix is as follows.

$$\varepsilon_{IP} = \left[\{\zeta\}^T[Q]^{-1}\{\zeta\}\right]^{-1} \tag{7.18}$$

Chapter 8

Approximate Effects of Blade Number

Betz describes the circulation for an infinite number of blades that is equal to uniform inflow for a *finite* number of blades.

$$IPE_{\text{Betz}} = 2\int_0^1 \frac{\bar{r}^3}{\lambda^2 + \bar{r}^2} dr = 1 - \lambda^2 \ln\left(1 + \frac{1}{\lambda^2}\right) \tag{8.1}$$

Prandtl extends the work of Betz and approximates both the effect of tip losses (which are due to the thrust loss near the blade tip for a finite number of blades) and lift tilt (where the lift vector is positioned perpendicular to the vortex sheets instead of perpendicular to the rotor disk) on induced power. References [18] and [23] illustrate Prandtl's approximation of the induced power efficiency for rotors with finite blade number. The plots displayed in Figure 8.1 depict the effects of swirl generation due to the inclination of the lift vector on induced power for a rotor with 4 blades. The blue curve ($cos(\varphi) = 1$) implies there is no swirl generated from the tilting of the lift vector. The green curve allows for swirl generation due to lift tilt. These were computed by the following model:

$$IPE_{\text{Prandtl}} = \frac{4}{\pi}\int_0^1 cos^2(\varphi) \cdot cos^{-1}\left(e^{\left(\frac{-Q(1-r)}{2\lambda}\right)}\right) r dr \tag{8.2}$$

which is done numerically.

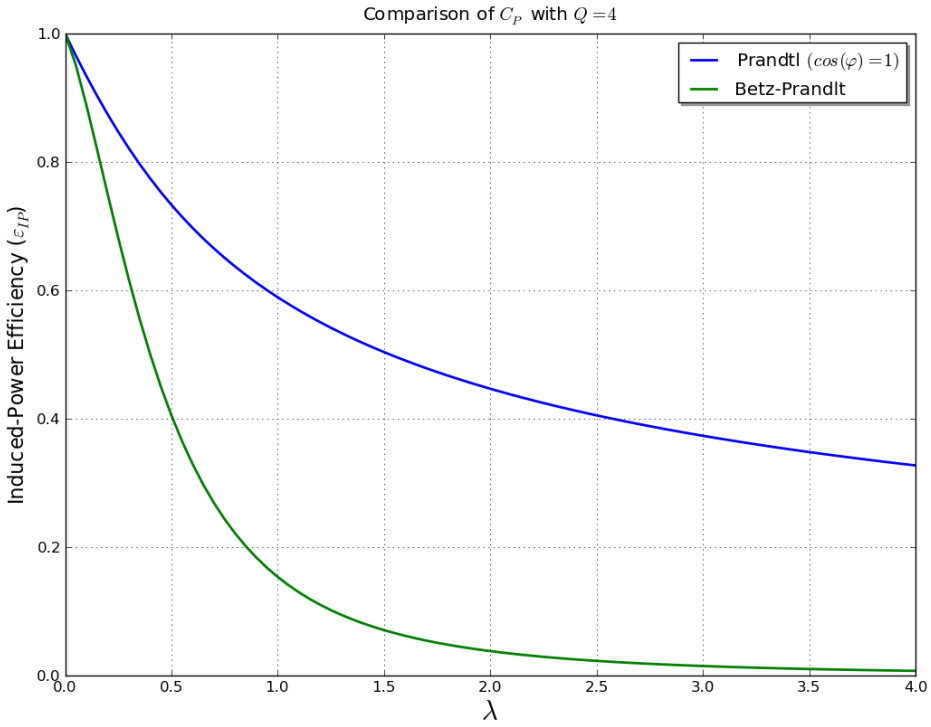

Figure 8.1: Prandtl comparison with/without tip loss and lift inclination.

The next goal for this research is to validate the finite blade solution with a comparison to these curves. Swirl correction factors were explored by Ref.[18] and these correction factors will be investigated further with the current optimized solution for induced power performance.

Reference [3] attempted to extend the Prandtl and Betz inflow model to determine an optimum circulation. Another goal of the current research is to compare with these models. For the infinite blade approximation, the optimized solution will be adjusted to include the effect of lift inclination to compare with Betz. This lift inclination will then be included in the finite blade analysis and compared with Goldstein.

$$IPE_{\text{Goldstein}} = IPE_{\text{Betz}} + \sum_{k} \left(\frac{4Q^2}{\pi^2 k^2 \mu_0^2} \int_0^{\mu_0} \mu \cdot h(\mu) d\mu \right) \tag{8.3}$$

8.1 Axial Flow

The matrix $[M]$ in Eq.(3.9) was originally derived from potential flow theory for an actuator disk. This implies that there is no angular momentum added to the flow through the disk and, consequently, no energy loss due to swirl. Makinen[19] showed that the effect of swirl could be accounted for in a rigorous manner in the context of a finite-state actuator disk by two adjustments: 1.) the induced flow at the rotor disk is taken to be parallel to the local rotor lift vector, 2.) the mass matrix is augmented to include the extra kinetic energy in the swirl velocity. The amount of added mass was found to be

$$[M^m]_{\texttt{swirl}} = [M^m]\left[[I] + m\left(\frac{\kappa\lambda}{Q}\right)^2\left[[I] - [A^m]^2\right]^{-m}\right] \tag{8.4}$$

where m is the harmonic number for a given term, λ is the inflow ratio, Q is the number of blades, and κ is an empirical factor to account for the swirl velocity. Although κ is theoretically equal to 2.0, the best correlation with Goldstein was found for $\kappa = 2.2$. It should be noted that the apparent mass matrix takes the following form:

$$[M^c] = \begin{bmatrix} [M^0] & & & \\ & [M^1] & & \\ & & \ddots & \\ & & & [M^m] \end{bmatrix} \tag{8.5}$$

where, $[M^0] = \frac{1}{2}[M^0]_{\texttt{He}}$ is a modified form of the original mass matrix from the Peters-He model. A similar matrix exists for the sine representation ($[M^s]$) but with no zeroeth harmonic terms.

In the derivation of this swirl correction by Makinen, it was assumed (in the context of a helicopter) that λ is small such that $\lambda^2 \ll 1$. However, in order to correlate with Goldstein results, one must allow for λ to be of the order unity or larger. Therefore, it is necessary to extend the formula in Eq.(8.4) to large λ. This implies replacing $\kappa^2\lambda^2$ in this equation with a more general $f(\lambda)$. In order to do this, we ran our numerical Goldstein solution for rotors with 2, 4, and 6 blades over climb ratios from 0 to 4.0. We then optimized the swirl correction function based on the most rapid convergence of the finite-state model to the induced power efficiency as found from the numerically exact Goldstein results.

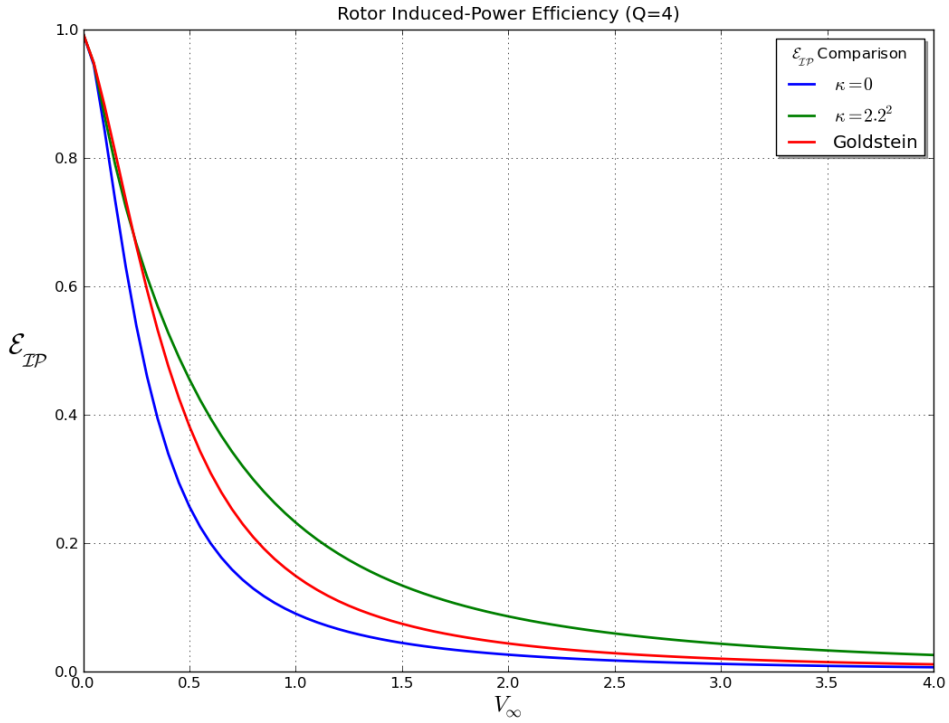

Figure 8.2: 4 bladed rotor comparison with $\kappa = 0$, $\kappa = 2.2$, and results from Goldstein solution.

Figure 8.2 shows plots with the swirl correction factor forced to zero—this implies that there is no swirl generation due to the tilting of the lift vector—as well as the Makinen factor of 2.2.

Results for the optimum $f(\lambda)$ were found to be relatively insensitive to blade number so that a single expression could be found, as shown in Figure 8.3. The resulting curve was then fit with a rational polynomial in λ, also shown in the figure. At small λ, the new swirl correction behaves as $4.4\lambda^2$ ($\kappa \approx 2.09$)—whereas the result in Makinen gave $\kappa = 2.2$ for the optimum fit. In revisiting the optimization results of Makinen, we discovered that the higher value of κ found in that work was due to the attempt of the optimizer to lower the error at larger values of λ. The new factor improves correlation at all inflow ratios. It should be noted that the efficiencies become very low for $\lambda > 1$ such that the "optimum" value is fitting a very small number. The important part of $f(\lambda)$ for practical considerations is for $\lambda < 0.5$ where the new formula is a significant

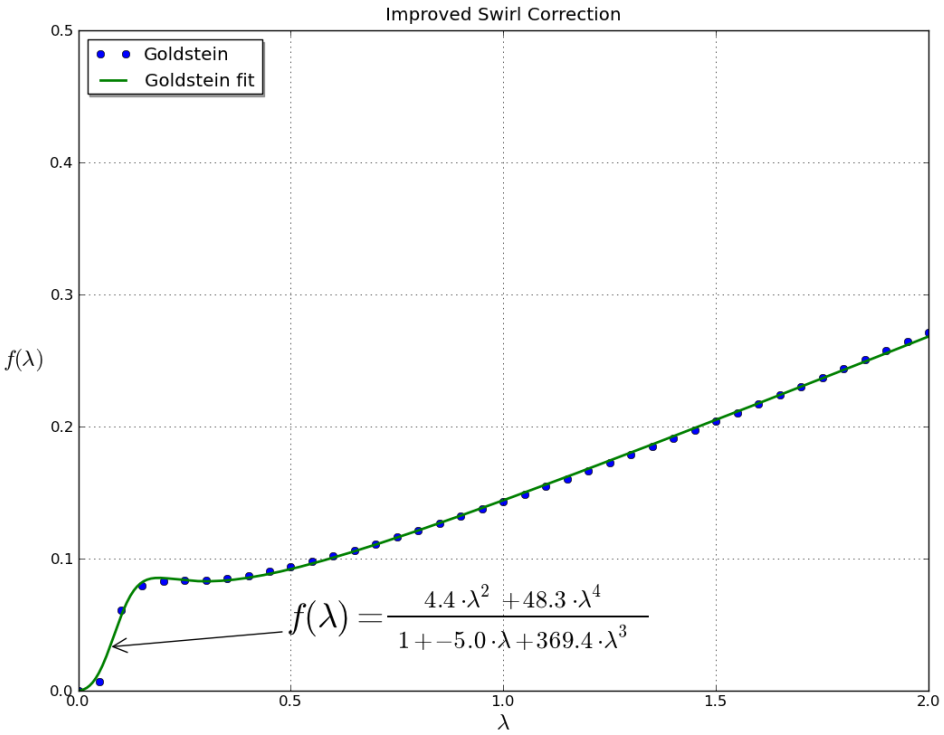

Figure 8.3: Swirl correction as a function of the inflow ratio λ to correlate with Goldstein 2 blade solution.

improvement over that of Makinen. This new formula is used in all of the results to follow.

8.2 Blade Number Factor

To address the original question pertaining to induced-power, Ref.[24], a detailed investigation to the effects of blade number is in order. Reference [24] uses RCAS to compute values of induced-power ratio—that is, the induced-power coefficient C_P divided by the Glauert minimum $C_{P_{ideal}}$—for a rotor in forward flight conditions, Fig.8.4. These values are the result of subtracting known sources of power demands such as aerodynamic drag and profile drag to reduce the vaules to that of induced-power only. Reference [24] argues that the vaules of the induced-power of the lifting

rotor are still significant. To better understand what the effects are as blade number goes to infinity, a plot of the inverse of blade number is produced. Figure 8.4b is a plot of the data computed by Ref.[24] versus $1/Q$. With a value of unity for the induced-power ratio at $1/Q = 0$ (or as $Q \to \infty$), a linear distrubution of the induced-power ratio is quite evident.

8.2.1 Prandtl Tip Correction

To more accurately define a blade factor equation for the power loss of the lifting rotor, a more indepth look at axial and forward flight studies is necessary. The tip correction factor of Prandtl can be approximated as follows:

$$B = 1 - \frac{2\ln(2)}{Q} \cdot \frac{\lambda}{\sqrt{1+\lambda^2}} \tag{8.6}$$

where Q is the number of blades and λ is the inflow ratio $V_\infty/\Omega R$. One may then take a first order approximation to this for small λ.

$$B \approx \frac{1}{1 + \frac{2\ln(2)}{Q} \cdot \frac{\lambda}{\sqrt{1+\lambda^2}}} \tag{8.7}$$

where an inverse of this would provide a type of power ratio factor for a given blade number.

$$h(\lambda) = \frac{1}{B} = 1 + \frac{1}{Q} \cdot \frac{2\ln(2) \cdot \lambda}{\sqrt{1+\lambda^2}} \tag{8.8}$$

However, this is valid only for axial flow at small λ. To extend this to larger inflow, one may assume that the above power factor is simply a low-order approximation to the more general power factor. Prandtl agrees with Goldstein for small λ. Therefore, the leading coefficient should remain as $2\ln(2)$. A least-squares fit at, say, $\lambda = 0.5$ yields a constant of 7.83. Thus a modified form of the power factor may be expressed as the following.

$$h(\lambda) = 1 + \frac{1}{Q} \cdot \frac{(2 \cdot \ln(2) + 23.8 \cdot \lambda^2) \cdot \lambda}{\sqrt{1+\lambda^2}} \tag{8.9}$$

8.2.2 Hall-n-Hall Data

To allow the blade effect factor to account for forward flight conditions a dependence on advance ratio, μ, is needed. Inspection of the data presented by Ref.[26] shows a great dependence on advance ratio, Fig.8.5.

To calculate this dependence, a linear curve fit was computed for varying advance ratios and then the change—i.e., the slope—of each fit was plotted against advance ratio. Figure 8.6 details this method with a few sample plots of advance ratios of 0.5, 0.6, 0.7, and 0.76.

The slopes of these fits were then plotted against advance ratio to determine a function that would account for the effects blade number has on induced power. Figure 8.7 displays the strong dependence on advance ratio as values increase beyond 0.5.

A curve-fit to this data yeilds the following empirical function:

$$g(\mu) = 24.8 \cdot \tan^{-1}(2.2 \cdot \mu^3 + 2.9 \cdot \mu^5) \tag{8.10}$$

Equations 8.9 and 8.10 may then be combined to formulate a blade number effect model that is valid for both axial and forward flight conditions.

$$f(Q) = 1 + \frac{1}{Q} \cdot \frac{2 \cdot \ln(2) \cdot \lambda + 23.8 \cdot \lambda^3 + 24.8 \cdot \mu \cdot \tan^{-1}(2.2 \cdot \mu^3 + 2.9 \cdot \mu^5)}{\sqrt{1 + \lambda^2 + \mu^2}} \tag{8.11}$$

Figure 8.8 is a sample calculation of Eq.8.11 with advance ratio 0.73 and inflow ratio 0.2.

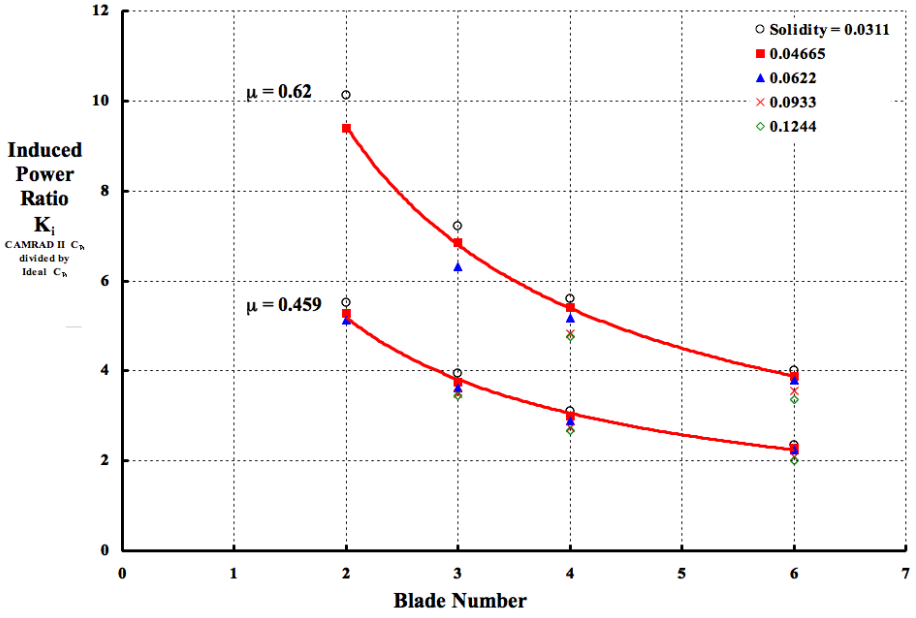

(a) Induced-Power Data

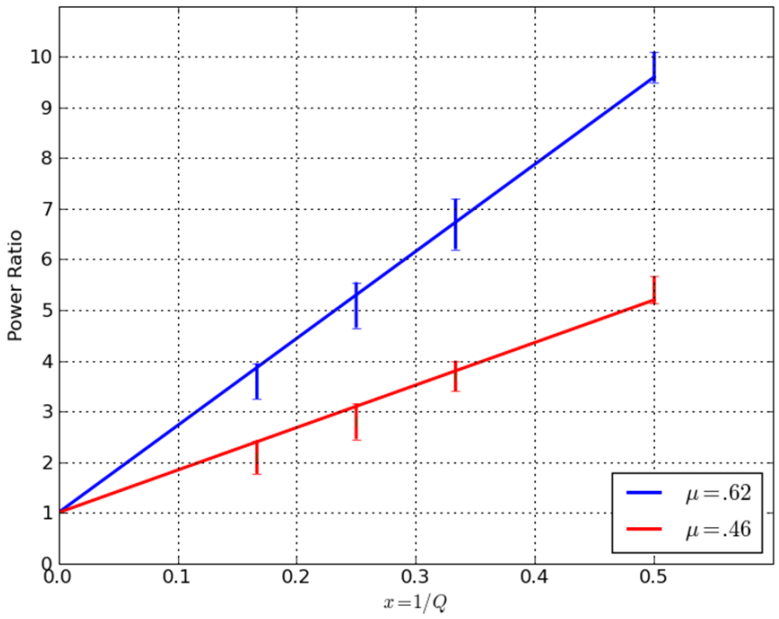

(b) Inverse of Blade Number

Figure 8.4: Induced-power ratio computed from RCAS, Ref.[24].

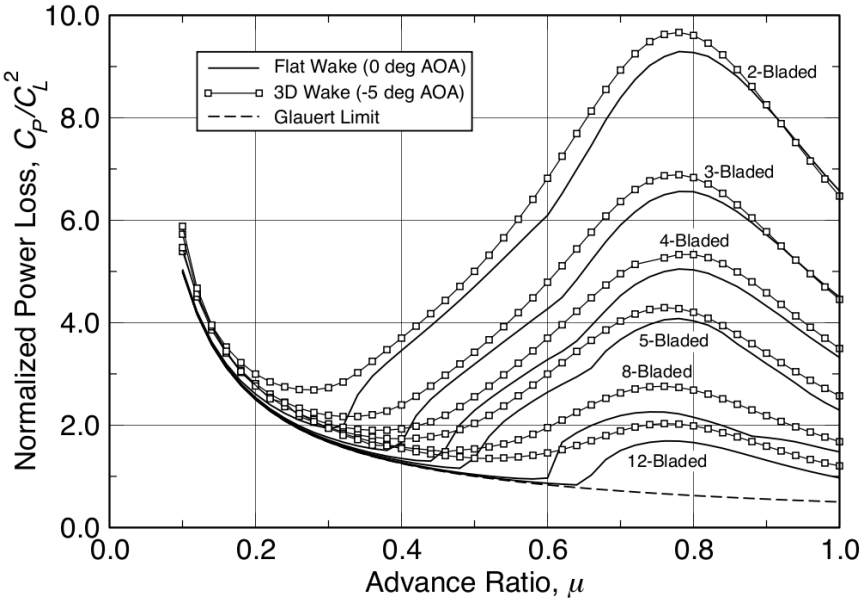

Figure 8.5: Hall and Hall data, Ref.[26], trimmed.

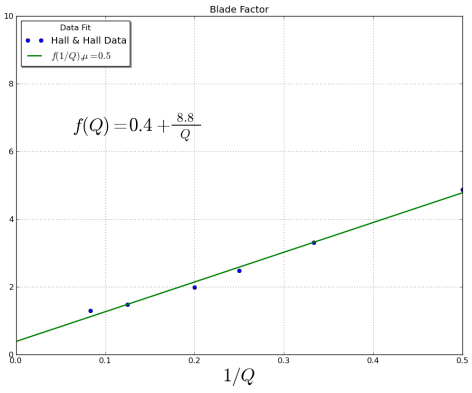

(a) $\mu = 0.5$

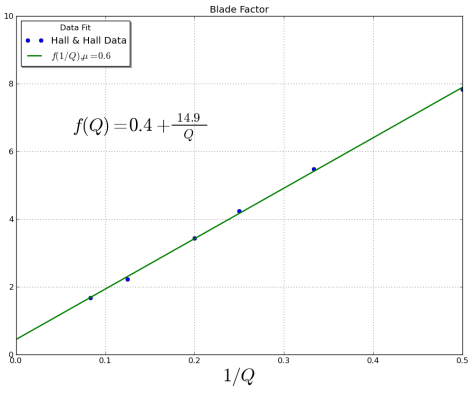

(b) $\mu = 0.6$

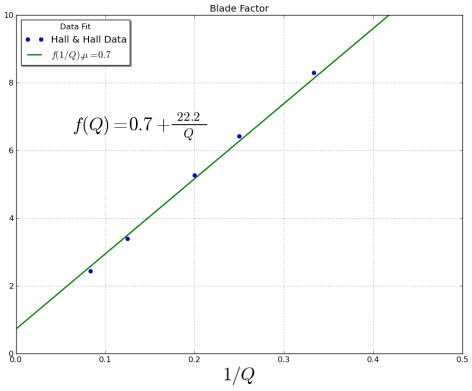

(c) $\mu = 0.7$

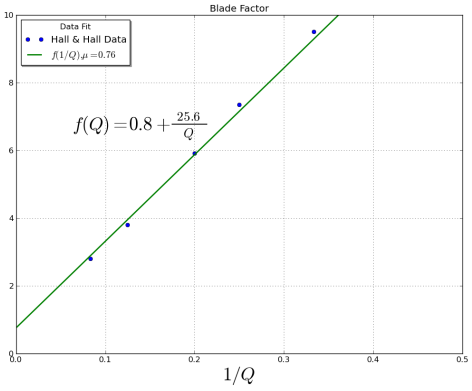

(d) $\mu = 0.76$

Figure 8.6: Plots of the induced-power as a function of one over the blade number for a given advance ratio.

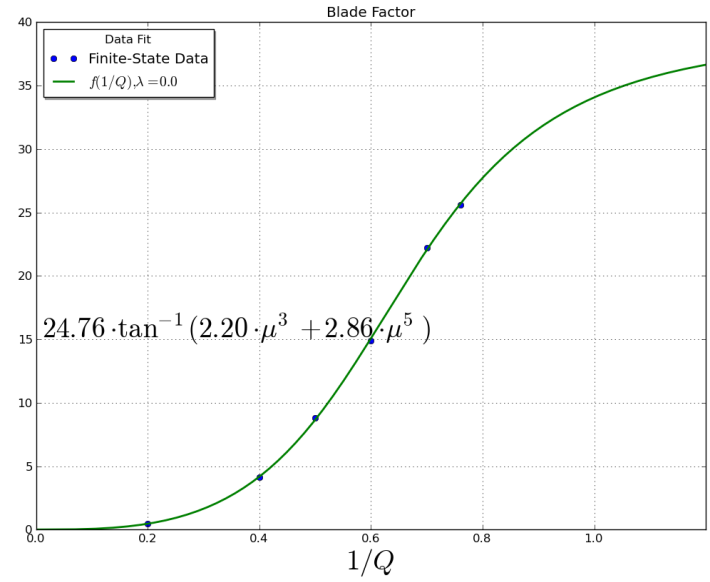

Figure 8.7: Blade number effect on performance as a function of advance ratio, μ.

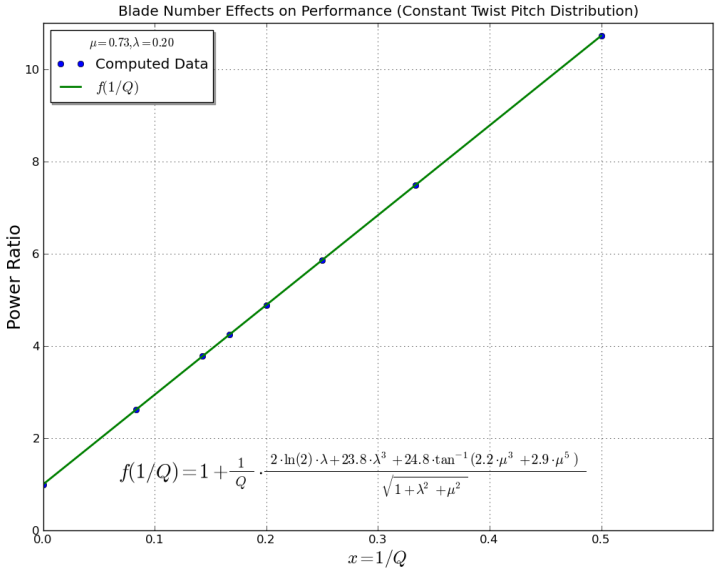

Figure 8.8: Blade number effect as a function of $1/Q$.

Chapter 9

Results and Comparisons

9.1 Infinite Blade Analysis

Although the above theory, with $[\bar{L}]$ defined appropriately, can be applied to rotors with a finite number of blades, in this section we present results only for an infinite number of blades ($Q = \infty$). Also, the transformation matrices $[A]$ and $[B]$ can be obtained in closed form either with or without reversed flow, herein we neglect reversed flow. Third, since we neglect induced-flow feedback ($\sigma a/8V \ll 1$), the matrix $[B]$ does not enter the present computations. Nevertheless, the theory presented herein (including optimization) applies both to a finite number of blades and to induced-flow feedback. Resuts for finite blade analysis is presented in the following section. However, inclusion of the reversed flow region and induced-flow feedback is proposed for future work.

Typical results for IPE are shown in Figs.9.1-9.3. Each figure is for a particular set of blade pitch controls defined by a combination of parameters M and K introduced earlier with Eq.(5.1). Here, M is the maximum harmonic allowed for the control inputs; and, similarly, K is the maximum power of $\bar{r}$ allowed for the control inputs. Therefore, $M = 0$ corresponds to a steady state input; $M = 1$ to both steady and first harmonic, as in collective and cyclic pitch; while $M = 2$, 3, and 4 correspond to higher-harmonic pitch inputs at $2/rev$, $3/rev$, and $4/rev$, respectively. Similarly, $K = 0$ corresponds to radially constant (uniform) pitch, while $K = 1$ corresponds to a linearly twisted blade. Results are shown for skew angles of $\chi = 0^o$, 45^o, 60^o, and 75^o.

All of the results were obtained using finite-state inflow with 10 harmonics corresponding to 66-states. Reiterating again, the theory is for a lightly-loaded actuator disk (e.g., an infinite number of blades), and the inclination of the local lift vector is neglected. The effects of reverse flow from blade-element theory are neglected in the $[A]$ matrix and induced flow feedback via $[B]$ is neglected; the latter is the same as neglect of the effect of $\sigma a/8V$. This is not unreasonable for high advance ratios, however the neglect of the reverse flow region for $[A]$ is significant at high advance ratio. For this reason the present numerical results are somewhat preliminary, although they may be compared with other results that reflect the same approximation.

Figure 9.1 is for $M = 1$, $K = 0$, which corresponds to three allowable control inputs—conventional static collective and cyclic pitch of an untwisted blade. Figure 9.2 is for $M = 4$, $K = 0$, which is nine allowable controls—higher harmonic control of collective and cyclic pitch up to $4/rev$. Figure 9.3 is for $M = 4$, $K = 1$, corresponding to eighteen inputs including both uniform pitch and linear-twist as unsteady radial pitch distributions. Two sets of results are included. One set (Figs. 9.1a, 9.2a, and 9.3a) is for a flight condition where two rotor loads, the roll and pitch moment, are constrained to be zero—that is, the rotor is trimmed to zero hub moments. The other flight condition (Figs. 9.1b, 9.2b, and 9.3b) is unconstrained, such that the rotor roll and pitch moments are untrimmed.

Although the result is not shown in the figures, a special, *nearly* full-authority case ($M = 10$, $K = 5$) was computed as a baseline for comparison. For this case, the number of available rotor controls is 126 and this enabled sufficient flexibility for the rotor air-load to be optimized to very closely approach the ideal minimum induced power. It demonstrates virtually perfect efficiency with an $IPE = 1.0$ independent of skew angle, advance ratio, or trim condition. This nearly full authority result is true for an actuator disk without control constraints but will not be true with constraints or for a finite number of blades.

For the results in Figure 9.1, conventional collective and cyclic ($M = 1$, $K = 0$), advance ratio and skew angle both degrade efficiency, although the effect of skew angle is relatively small. At $\mu = 1.0$ and $\chi = 75^o$, the trimmed efficiency is down to 0.22 and untrimmed efficiency is down to 0.54. The effect of trim is therefore clearly evident. When the rotor is constrained to be trimmed, it cannot obtain an

efficiency as high as can be obtained without this additional constraint, and the loss is substantial. Although trim does not affect the baseline control case (i.e., nearly, full-authority with an infinite number of blades), it profoundly affects cases with limited available control. This corroborates the findings of Ref.[26] that trim profoundly affects efficiency.

The results in Figure 9.2 show that higher harmonic control (HHC) of the untwisted blade case ($M = 4, K = 0$) increases the induced power efficiency by redistributing the rotor loading through optimization with the additional controls. Current active rotor control research is partly based on improving rotor aerodynamic efficiency in this manner, and the present methodology provides some indication of the theoretical potential available from this approach. For $4/rev$ HHC without radial twist control, the improvement for the trimmed rotor and 75^o wake skew angle is limited to about 10% for advance ratios below 0.4.

Figure 9.3 illustrates the extra efficiency that can be gained by the addition of linear twist ($M = 4, K = 1$). Improvements are realized for all advance ratios for both the trimmed and untrimmed cases, especially compared to the trimmed results for the rigid blade case in Figure 9.1a. Also of particular interest is the case at zero advance ratio and zero skew angle (hover, axial flow), for which no higher-harmonic loadings appear in the optimum solution (and trim is not an issue). One can see that the induced power efficiency with no twist is given by $IPE = 0.873$ whereas the efficiency with linear twist is $IPE = 0.966$. If a quadratic term were added to allowable twist ($K = 2$), the efficiency increases to $IPE = 0.979$. As advance ratio increases, the advantages of nonlinear twist seem to diminish.

Figures 9.1-9.3 show that, in general, the higher the level of constraint on the controls or rotor loads, the higher the resulting rotor induced power. With fewer constraints (such as unconstrained rotor moments - untrimmed) and a higher number of available controls, the more the rotor pressure distribution can redistribute itself to minimize power.

Figure 9.4 gives results for the case of perfectly edgewise flow, $\chi = 90^o$, for which the rotor trailed and shed wake vorticity collapses to a planar sheet (i.e., a flat-wake). For other wake skew angles the wake vorticity fills the oblique cylinder downstream of the rotor disk. For the edgewise flow, flat-wake condition, there is a singularity in the

optimum solution because there are redundant pressure distributions that will result in the identical vorticity within the flat wake. However, the limit as χ approaches 90^o does exist; and this is computed by use of a nearly flat wake, (i.e., $\chi = 89.9^o$).

Figure 9.4a gives IPE for the flat wake under various available controls (and for both trimmed and untrimmed rotors) in a similar manner as was presented for other skew angles results in Figs.9.1-9.3. The results for limited control authority ($[M, K] = [1, 0]$ and $[4, 0]$) show that IPE increases beyond $\mu = 0.8$. Detailed runs reveal that, for $[M, K] = [1, 0]$, this reversal of the slope of IPE versus advance ratio begins at $\chi = 85^o$ for both trimmed and untrimmed cases—reaching the level seen in Figure 9.4a for edgewise flow. For $[M, K] = [4, 0]$, the reversal does not appear until $\chi = 87.5^o$. Figure 9.4b presents the flat-wake results in inverse form as $IPR = 1/IPE$ which more clearly shows both the increase in required power (over Glauert power) as one approaches $\mu = 0.8$ and the decrease in power for $0.8 < \mu < 1.0$.

In order to make the present results more directly meaningful in terms of induced power for a given value of rotor lift, the flat-wake results are presented as normalized induced power, $C_P = C_T^2$ in Figure 9.5. Relevant results from Ref.[41] are also included for comparison. The Figure 9.4b results are expressed as normalized power and shown in Figure 9.5a; for edgewise flow they are equal to $IPR/(2\mu)$. The Glauert ideal power is included for comparison to highlight the well-known inverse relationship with advance ratio. It is not difficult to appreciate that Glauert theory encourages the belief that induced power is unimportant at high advance ratio. However, the present flat-wake results for lower control authority, $[M, K] = [4, 0]$ and $[1, 0]$, show a significant increase in induced power as advance ratio approaches 0.8, followed by a decrease at higher advance ratio. Clearly, Glauert induced power is not accurate for these advance ratios. For the high control authority case, $[M, K] = [4, 1]$ in Figure 9.5a the induced power is nearly equal to Glauert ideal power for both the trimmed and untrimmed cases. A significant finding of the present investigation is that increasing the number of available controls enables the optimum induced power to approach Glauert ideal power.

The present flat-wake results in Figure 9.5a can be compared with the results from Ormiston from Ref.[41]. These results are shown in Figure 9.5b for a three-blade rotor with a solidity of 0.111 and no root cutout. The effects of reverse flow are not

neglected. The induced power is obtained from the analytical power model having constants identified from numerical data computed with finite-state inflow theory for $M = 9$ and 55-states. The Ormiston rotor has two explicit rotor controls: collective pitch and rotor disk angle-of-attack; and cyclic pitch is included implicitly to satisfy the zero rotor moment trim constraint. Note that the present results do not include rotor angle-of-attack as a control variable. Three results from Ref.[41] are included: 1) collective mode induced power, identical to the present $[M, K] = [1, 0]$ case; 2) rotor angle-of-attack mode induced power; and 3) the minimum power obtained by optimizing the two rotor controls. These results show the singularity of the collective mode induced power at the critical advance ratio near $\mu = 1.0$ that is due to the reverse flow region and the thrust control derivative reversal mentioned in the Background section. The angle-of-attack mode induced power is significantly lower than the collective mode, and optimizing the two rotor controls further reduces the induced power.

Ormiston's results show significantly larger induced power than the present results, particularly for the collective mode that compares directly with the $[M, K] = [1, 0]$ case here. There are two main reasons for this. First, the presence of three blades significantly increases induced power relative to an infinite-bladed actuator disk; and, second, the effect of reverse flow is important, particularly near the critical advance ratio. Although this is not a one-to-one comparison because of several modeling differences, the two sets of results clearly show very similar qualitative trends for the rapid increase of induced power at high advance ratio. At $\mu = 0.8$, both the present $[M, K] = [1, 0]$ trimmed results and Ormiston's optimum results show an increase of induced power over the Glauert ideal power by a factor of approximately 3.3.

A few comments are in order here about optimization, rotor controls, constraints, and trim. As expressed herein, control authority is the ability to control the rotor disk airload distribution by varying blade radial and azimuthal pitch via the rotor control variables. The incorporation of blade-element theory frames the performance problem in terms of relevant rotor blade aerodynamic characteristics. As a consequence, the rotor pressure distributions are physically limited by the blade geometry. Therefore an increased number of rotor controls relaxes the rotor blades' limitations on the rotor air-load distributions. Low authority collective and cyclic pitch controls of typical rigid blades significantly constrain the available rotor air-load distribution. Additional

controls $\{\theta\}$ in the form of radial and azimuthal pitch variations (e.g., active control via variable geometry) enable increased variability in the air-load distributions. The rotor trim constraints are expressed in terms of rotor loads constraints through the $\{C\}$ load vector.

In view of the above discussion, some of the present optimum induced power results may be interpreted in a different light. For example, the present results for the $[M, K] = [1, 0]$, that represent a rigid untwisted blade with steady state collective and cyclic pitch do not, strictly speaking, represent an optimum solution for rotor induced power. Despite the fact that the solution is obtained from formal constrained quadratic optimization, the available controls are all utilized to satisfy the rotor loads constraints of producing thrust and rotor moment trim. There are no additional controls to further change the rotor air-load distribution to reduce induced power—therefore, the result is not really an optimum in the sense of minimum power. The induced power in the $[1, 0]$ case is, in fact, the characteristic induced power of Ormiston's "collective pitch mode". The lack of the singularity at the critical advance ratio is due to the neglect of reverse flow.

The present normalized power results in Figure 9.5a can also be compared with trimmed results taken from Hall and Hall, Ref.[26]. Figure 8.5 shows these results for various blade numbers for the edgewise rotor flat wake at 90^o wake skew angle as well as an 85^o wake skew angle case (-5^o disk angle-of-attack). The Hall and Hall results are based on minimum power quadratic optimization using a vortex lattice wake model. These results are important in that they explicitly show the significant increase in induced power relative to the Glauert ideal power at high advance ratios—and are thus qualitatively consistent with the present results and Ormiston's results. The Hall and Hall results are also significant in showing the marked decrease of induced power with increasing blade number; the 12-bladed case approaches the actuator disk condition and is very close to the Glauert ideal power. This is very similar to the present $[M, K] = [4, 1]$ result. In other words, the limit of increasing the number of blades is effectively equivalent to the limit of increasing the number of rotor controls. Either approach enables the optimization process sufficient flexibility to distribute the rotor pressure loading to approach the ideal loading. The neglect of reversed flow effects in the present results is indirectly similar to the Hall and Hall results since they treat the rotor blade load as a radial bound circulation distribution

that is not subject to reverse flow physics arising through the blade-element air-load formulation.

9.2 Finite Blade Analysis

In this section we treat the optimization theory with a finite number of blades. Also, the matrices $[A]$ and $[B]$ may be defined to include the reversed flow region. However, herein we neglect this effect. Third, the effects of inflow feedback are also neglected since it is assumed that $\sigma a/8V \ll 1$. Therefore, the matrix $[B]$ does not enter the computations.

Typical results for IPE are shown in Fig.9.6. Here, M is the maximum harmonic allowed for the circulation inputs. Therefore, $M = 0$ corresponds to a steady state input; $M = 1$ to both steady and first harmonic, etc. Results are shown for an infinite number of blades (which is the Glauert momentum optimum) and also for $Q = 2$, 3, 4, and 6. The limit to this finite blade number efficiency—provided by Betz[2]—states that the minimum power is achieved when the trailing vortex sheet is contained along a helical path behind the rotor. One can see the clear effect of blade number on efficiency. For this optimization, $M = 10$ is virtually full control authority on available blade twist.

Figure 9.7 shows the effects of including wake rotation for differing blade numbers in the computation. This is possible because the effect of blade number is distinct from the effect of swirl—i.e., wake rotation. The magenta, red, and blue lines are for blade numbers of $Q = 2$, 4, and 6, respectively. These three plots depict the induced power efficiency for rotors that do not experience wake rotation. However, in contrast to this, the yellow, light blue, and green lines—again $Q = 2$, 4, and 6, respectively—show the effects of wake rotation due to the tilting of the lift vector. Note that, at larger values of V_∞ , the effect of swirl dominates, whereas at lower climb rates the effect of blade number becomes more dominate.

The results presented in Fig.9.8 illustrate the rapid convergence by increasing the number of included terms in the circulation expansion. The difference in adding the third term is crucial. However, after that only minor increases in accuracy are

achieved by continuing to add terms. Increasing beyond 3 terms allows the solution to become more accurate only in the very low region of V_∞ which—for axial flow—is identical to the non-dimensional climb rate λ and the mass-flow parameter V. Figure 9.8a shows the induced-power efficiency for a rotor with 3 blades, whereas Fig.9.8b is for a rotor with 4 blades. These plots are both for an untrimmed rotor in axial flow and both include the effects of wake rotation.

The logarithmic plots shown in Fig.9.9 attest to the accuracy of the Finite-State method. Figure 9.9 shows that increasing the available harmonics drives the convergence towards that of Goldstein. Figure 9.9a exemplifies the difference between the Betz-Prandtl and Goldstein solutions and thus shows the finite-state method to be accurate with Goldstein. The data in Fig.9.9b was plotted on a logarithmic scale to accentuate the high order of agreement. From these graphs one can see that the finite-state method converges to the Goldstein results at all blade numbers.

The results in Fig.8.8 are examples of blade number effects for a rotor in forward flight conditions. Using the blade factor in Eq.8.11, the infinite blade solutions from Fig.9.5a may then be scaled to represent the approximate power loss for a rotor with a given number of blades. This may then be compared to the results of Hall & Hall[26]. Despite the analysis and modeling differences noted above, the present investigation, along with the results of Ref.[41] and [26] compared in Fig. 9.10, clearly demonstrates the significant increases of induced power over classical Glauert ideal power when advance ratio is increased above the range of low performance conventional rotorcraft. Note the difference in the location of the peaks in power loss between that of Ref.[26] and those of the present investigation. The data from Ref.[26] peak just before an advante raio of 0.8. However, upon inspection, the critical advance ratio occurs when the determinant of the trimming matrix becomes zero causing the system to be singular, Refs.[45]-[48]

$$\left\{ \begin{array}{c} 6\frac{C_T}{\sigma a} \\ -16\frac{C_L}{\sigma a} \end{array} \right\} = \left[\begin{array}{cc} 1+\frac{3}{2}\mu^2-\frac{4}{3\pi}\mu^3 & \frac{3}{2}\mu+\frac{3}{8}\mu^3 \\ \frac{8}{3}\mu+\frac{32}{45\pi}\mu^4 & 1+\frac{3}{2}\mu^2-\frac{5}{24\pi}\mu^4 \end{array} \right] \cdot \left\{ \begin{array}{c} \theta_0 \\ \theta_s \end{array} \right\} \tag{9.1}$$

where the determinant of the trimming matrix is defined below.

$$\text{Det} = 1-\mu^2-\frac{4}{3\pi}\mu^3+\frac{25}{24\pi}\mu^4-\frac{46}{15\pi}\mu^5-\frac{5}{16\pi}\mu^6+\frac{1}{90\pi}\mu^7 \tag{9.2}$$

When neglecting higher-order terms of μ^4 and larger—which implies ignoring the effects of the reverse-flow region—the determinant becomes zero when μ is approximately 0.86, see Fig.9.11a.

$$\text{Det} \approx 1 - \mu^2 - \frac{4}{3\pi}\mu^3 = 0 \tag{9.3}$$

The location of the peaks in the finite-state method illustrated in Fig.9.10b are very near to this value. This is a significant improvement over the results of Ref.[26].

Also, Ref.[24] uses RCAS to extract the induced power from a vast array of rotor configurations. With a solution to the induced power for finite number of blades, a comparison to Harris' data provides fundamental insight into the effect that blade number has on the induced power. Figure 9.12 shows the comparison between data extracted from RCAS and the computed values using the finite-state method with the imperical blade factor found in Sec.8.2. The lower values of the finite-state method may indicate a difference in rotor modeling. Reference [24] uses a single harmonic term with only constant pitch, whereas the finite-state model uses four harmonics with linear twist pitch distribution. This, however, provides great evidence to the linear dependence of blade number on the induced-power of the lifting rotor.

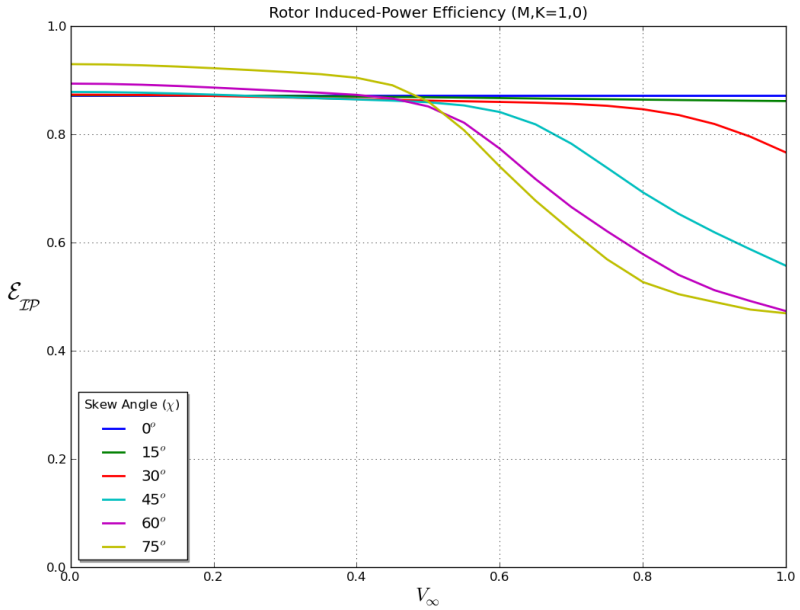

(a) Trimmed.

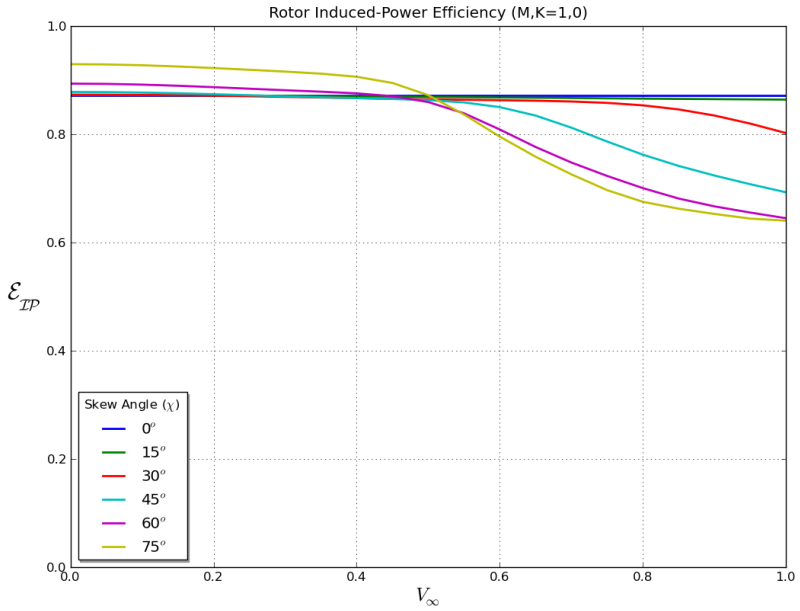

(b) Untrimmed.

Figure 9.1: Conventional collective and cyclic pitch inputs and without blade twist.

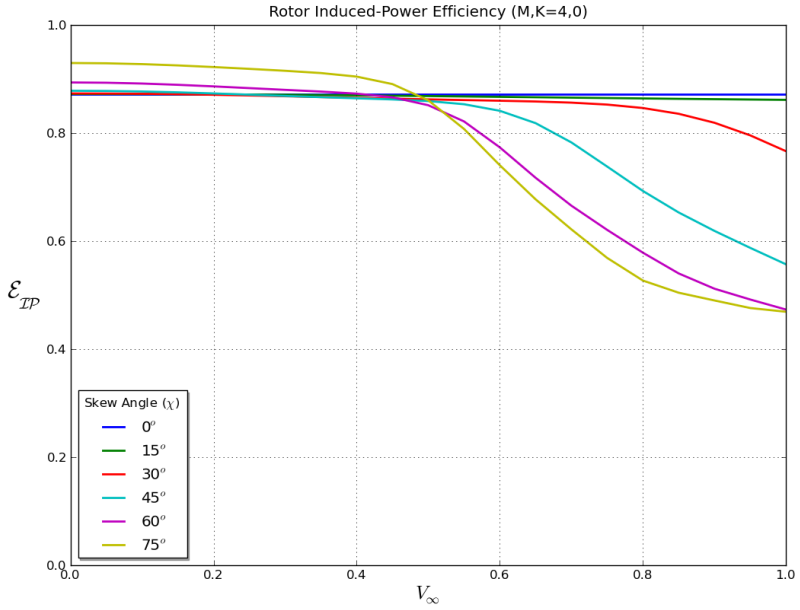

(a) Trimmed.

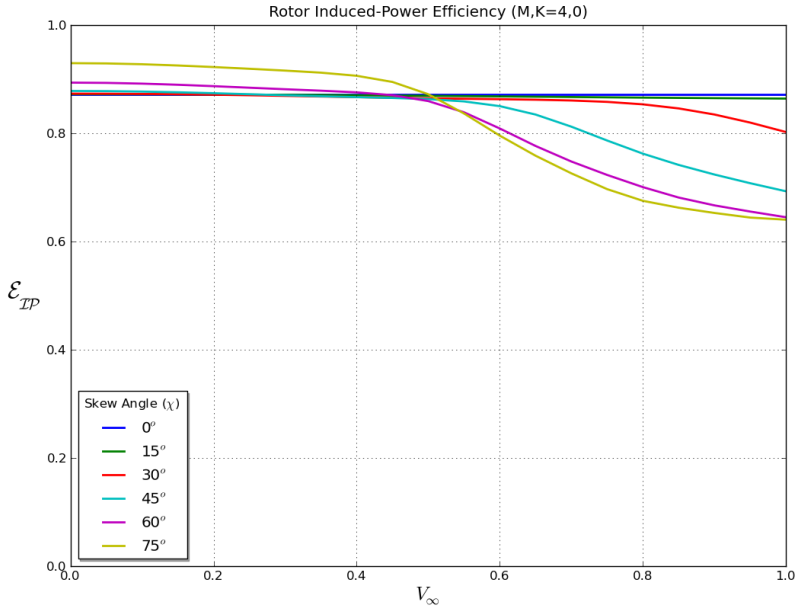

(b) Untrimmed.

Figure 9.2: Conventional collective and cyclic pitch inputs and higher harmonic control up to $4/rev$; without blade twist.

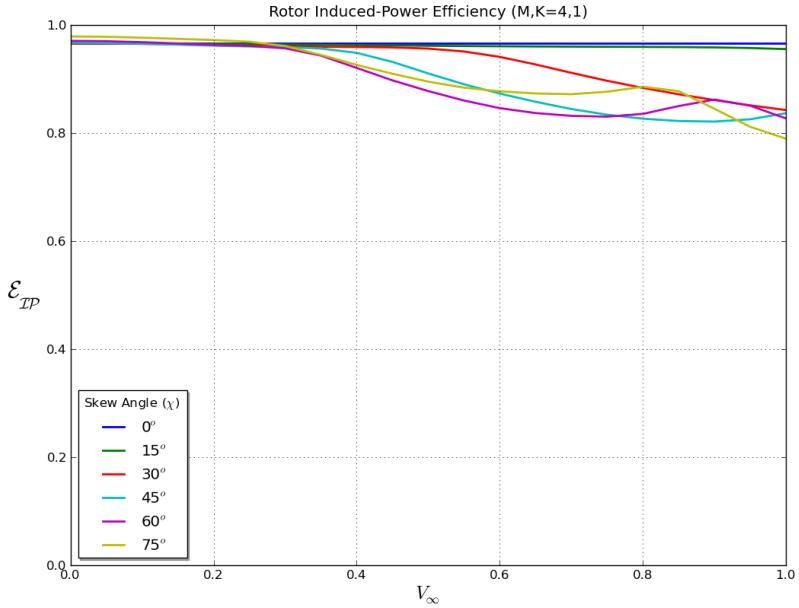

(a) Trimmed.

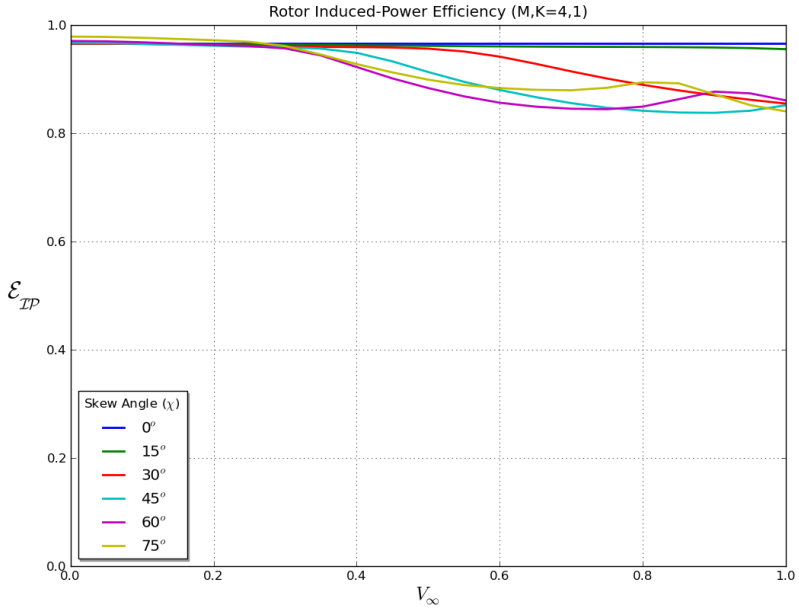

(b) Untrimmed.

Figure 9.3: conventional collective and cyclic pitch inputs and higher harmonic control up to $4/rev$; and with blade twist up to $4/rev$.

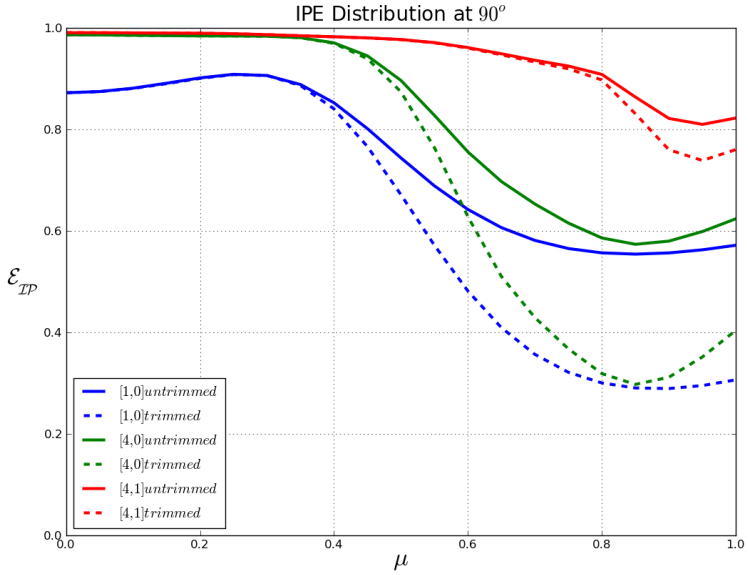

(a) Induced Power Efficiency, IPE, Glauert ideal power/Actual power.

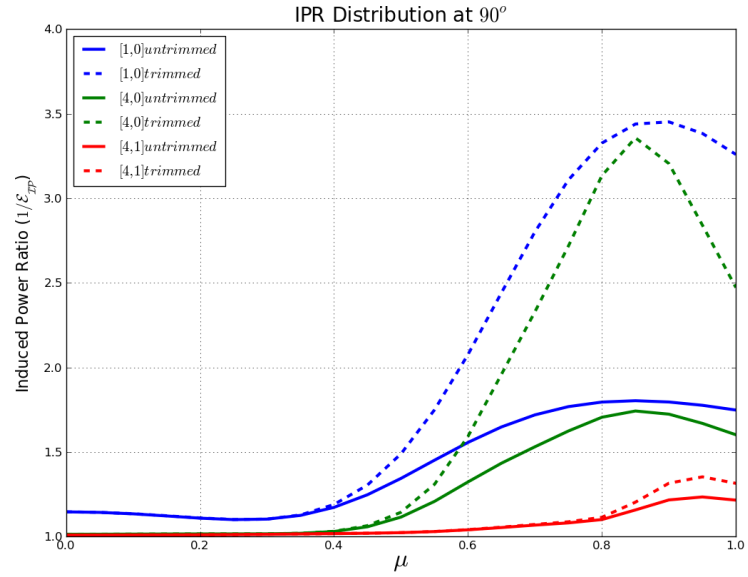

(b) Induced Power Ratio, IPR, Actual power/Glauert ideal power.

Figure 9.4: Induced power for the flat-wake edgewise rotor condition, skew angle $\chi = 90^o$, trimmed and untrimmed for the three rotor control combinations.

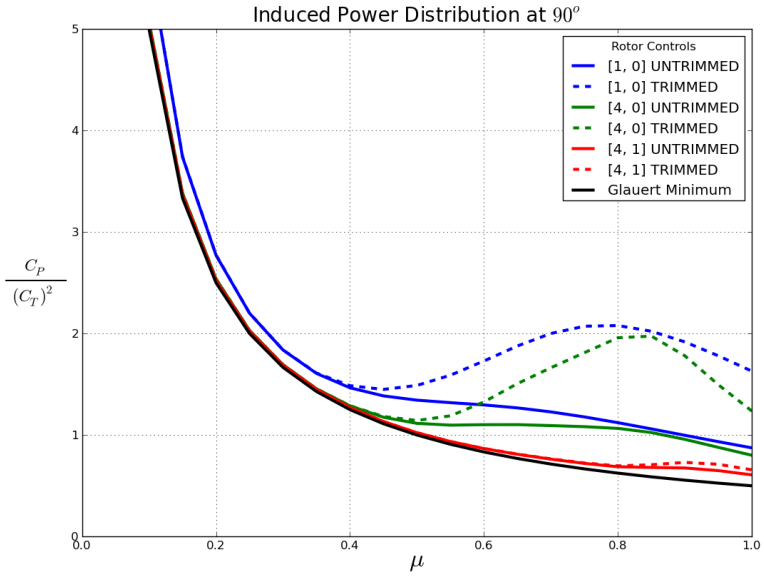

(a) Present results, trimmed and untrimmed for the three rotor control combinations.

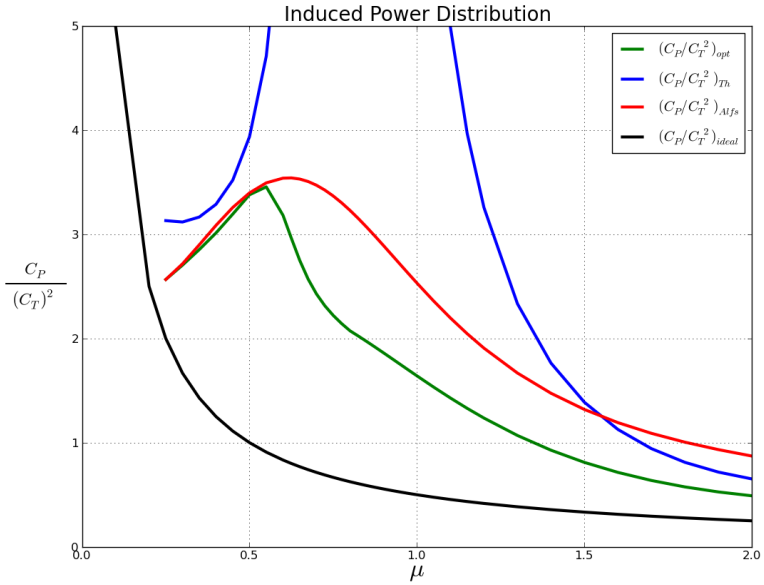

(b) Ormiston results, Ref.[41], three-blade rotor, with reverse flow effects and trimmed; collective mode, angle-of-attack mode, and optimum collective and angle-of-attack

Figure 9.5: Normalized induced power for the flat-wake edgewise rotor condition, skew angle $\chi = 90^o$.

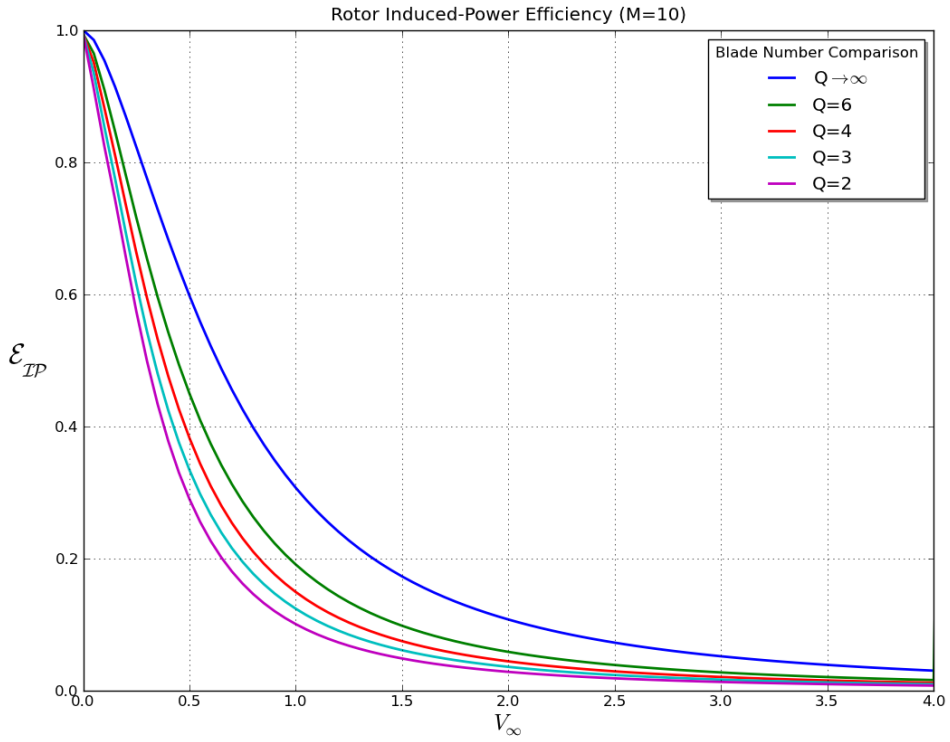

Figure 9.6: Effects of blade number on Induced-Power Efficiency in axial flow with Finite-State Model, untrimmed rotor.

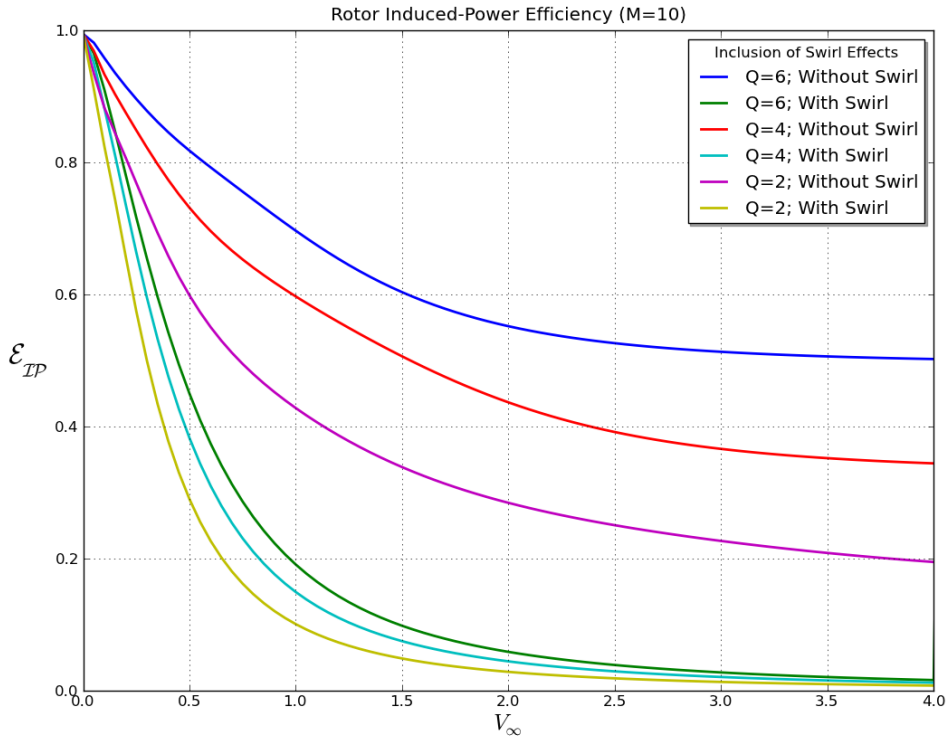

Figure 9.7: Effects of lift tilt on Induced-Power Efficiency with Finite-State Model, untrimmed rotor.

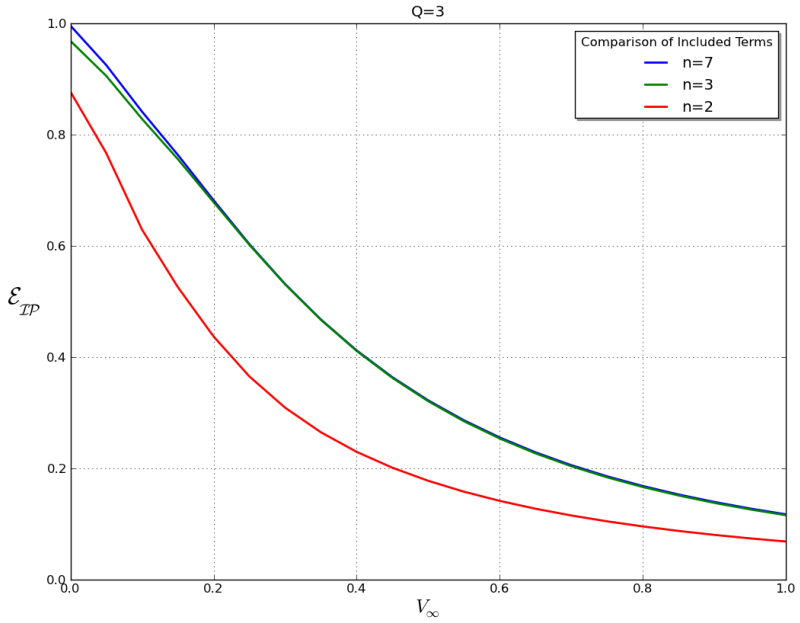

(a) 3 Bladed Rotor

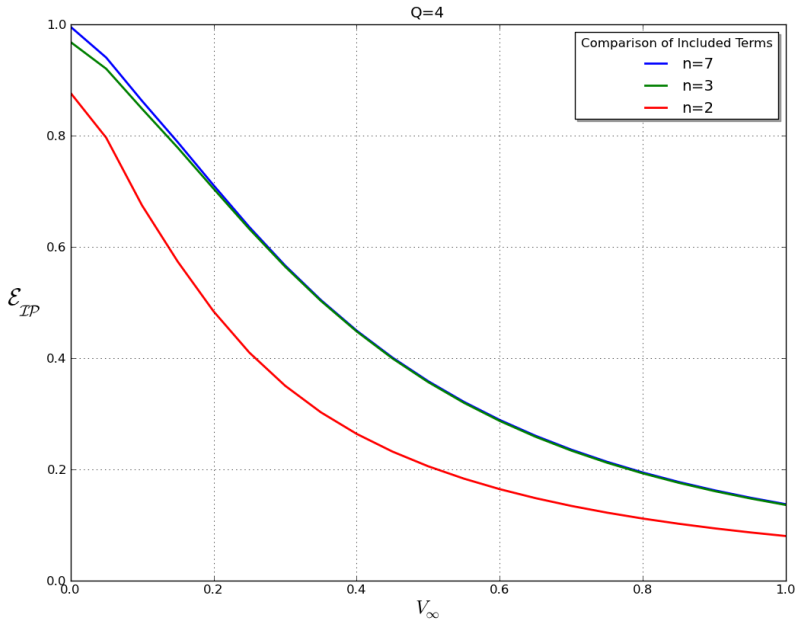

(b) 4 Bladed Rotor

Figure 9.8: Number of terms included in lift expansion for 3 and 4 bladed rotors, untrimmed rotor in axial flow.

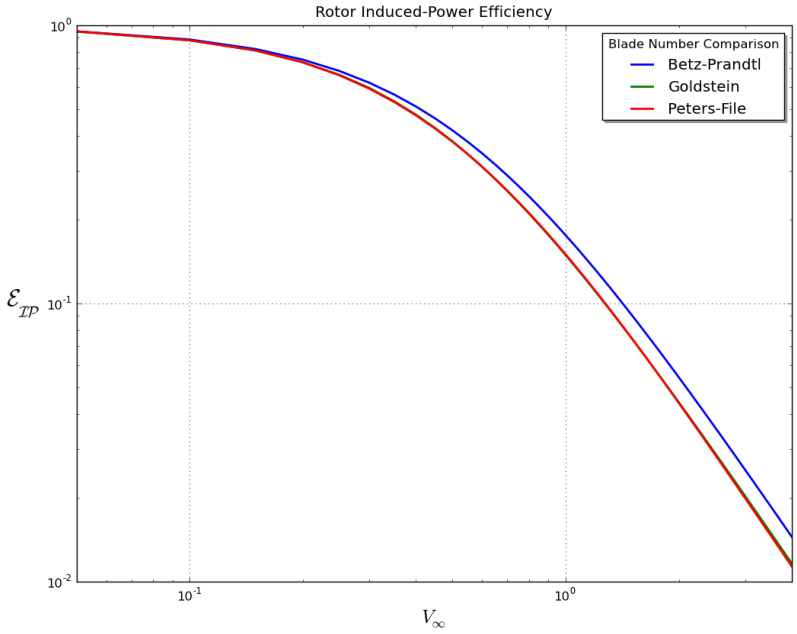

(a) Betz-Prandtl, Goldstein, Peters-File, $Q = 4$

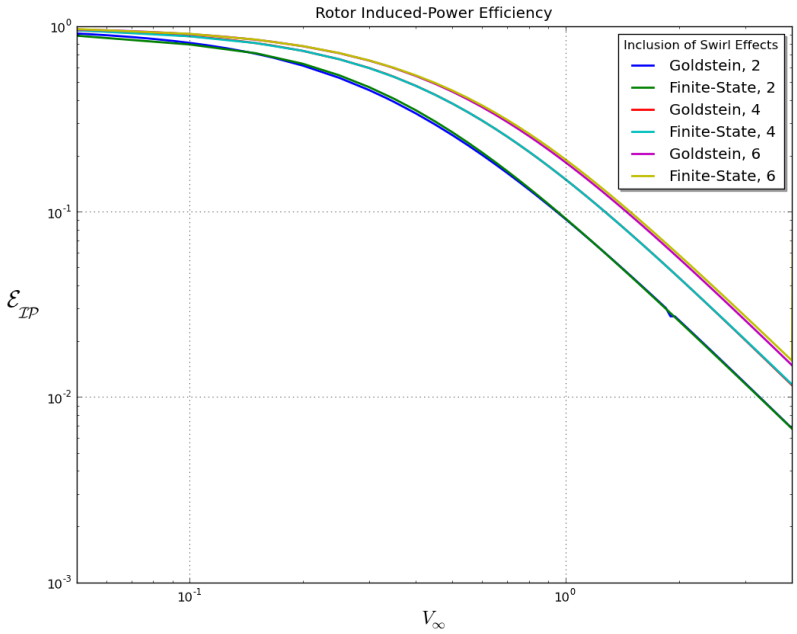

(b) Goldstein Comparison

Figure 9.9: Log correlations to Betz-Prandtl, Goldstein, and Finite-State models, untrimmed rotor in axial flow.

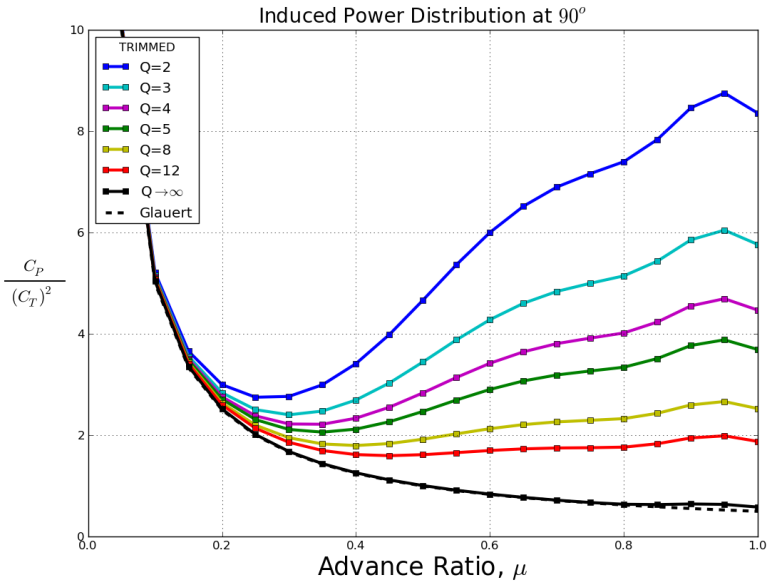

(a) Higher harmonic control and linear twist in edgewise flow, trimmed.

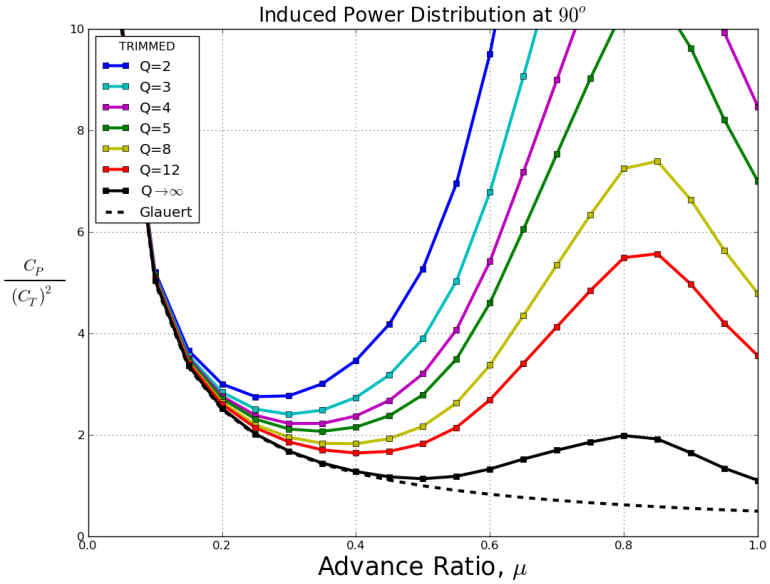

(b) Higher harmonic control and constant pitch in edgewise flow, trimmed.

Figure 9.10: Normalized induced power for the flat-wake, edgewise rotor condition, skew angle $\chi = 90^o$.

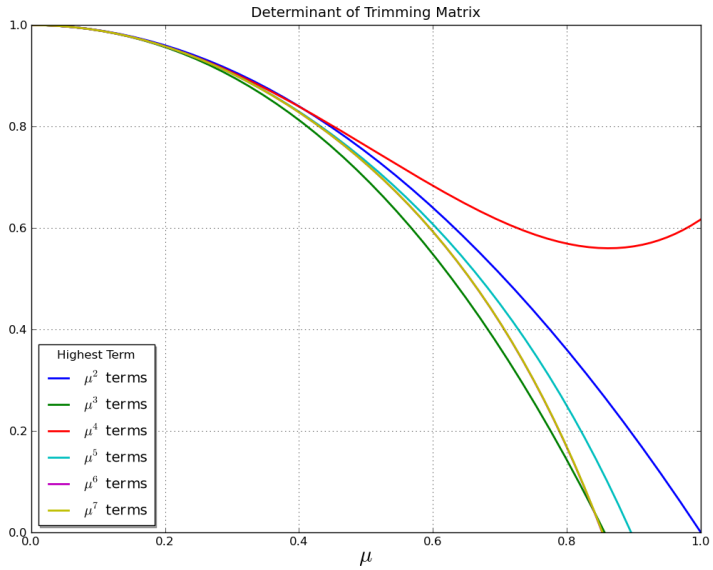

(a) Values for the determinant of the trimming matrix defined in Eq.9.2.

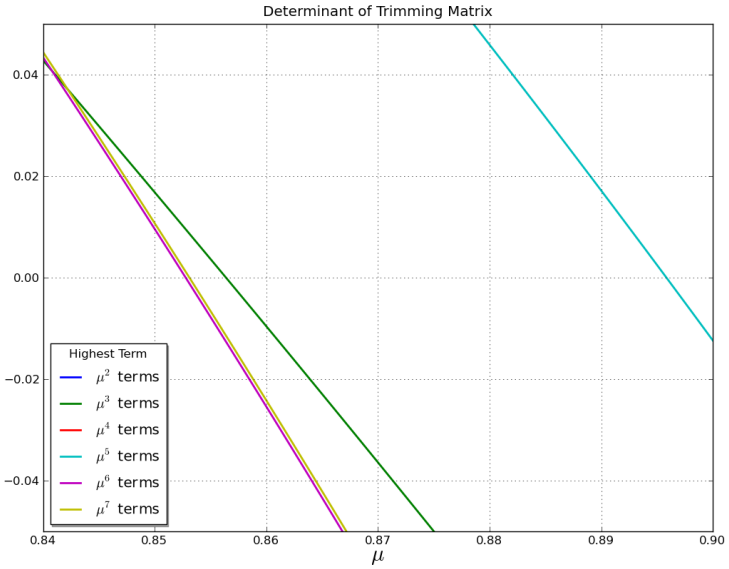

(b) Detailed plot of the areas where the zeros occur for differing truncations of the trimming matrix determinant.

Figure 9.11: Plots of the determinant of the trimming matrix for specific truncation values—i.e., $\mu^2, \mu^3, \mu^4, \cdots$.

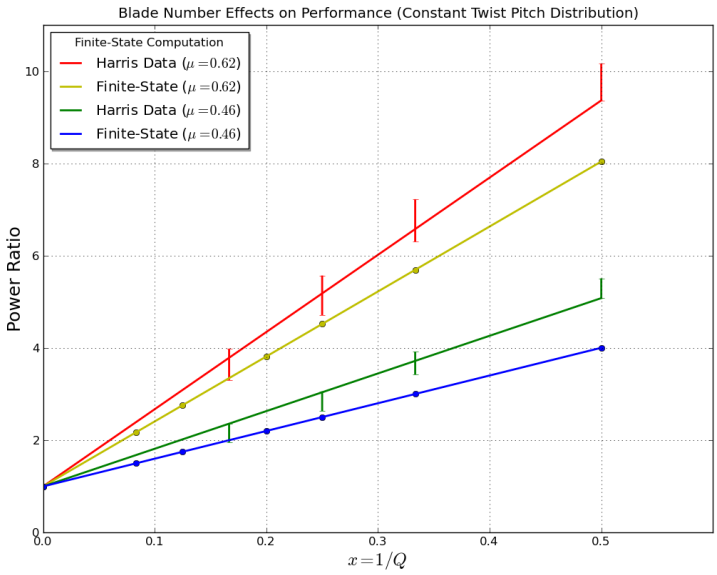

Figure 9.12: Finite-state computation of blade number effect on rotor performance.

Chapter 10

Summary and Conclusion

10.1 Infinite Blade Summary

Finite-state induced inflow theory has been applied to derive a general analytical model for rotor performance in forward flight for arbitrary loading and operating conditions. The theory combines rotor wake induced inflow with rotor blade-element theory to yield rotor forces and induced power in terms of arbitrary rotor controls and conventional rotor blade configuration parameters.

This present formulation is analogous to traditional blade-element momentum theory based on uniform inflow. However it explicitly incorporates the important complexity of non-uniform inflow from finite-state inflow theory responsible for significant increases in induced power at moderate and high advance ratio that is lacking in Glauert ideal power.

The general finite-state wake inflow rotor performance model provides the basis for classical, constrained, quadratic optimization to minimize induced power. A compact analytical expression was obtained for optimum induced power efficiency (IPE) in terms of wake skew angle and advance ratio that shows how additional controls for blade radial twist and higher harmonic azimuthal pitch enable induced power at high advance ratio to be minimized.

The present numerical results were limited to the infinite number of blades actuator disk case with both reverse flow and induced inflow feedback neglected. These are not restrictions of the general performance formulation presented herein and despite the

limitations of the numerical results, important new information was obtained that shows how optimum induced power varies with advance ratio, wake skew angle, trim condition, and the number of available rotor controls.

For the most constrained problem, the trimmed rotor with only conventional collective and cyclic controls, the induced power was significantly higher than Glauert ideal power for advance ratios above 0.5. As the number of available controls was increased, the induced power decreased rapidly to approach Glauert ideal power.

The present results were found to be generally consistent with recent previous investigations of induced power for the lifting rotor operating at high advance ratios. The present results reinforce the significance of rotor trim constraints in influencing induced power and the ability of additional rotor blade controls to redistribute the rotor loading to yield optimized minimum power. Insights from this investigation should help to guide for the development of future high-speed rotorcraft with higher aerodynamic efficiency.

The numerical results were limited to the actuator disk case with both reverse flow and induced inflow feedback neglected. These are not restrictions of the general performance formulation presented herein and despite the limitations of the numerical results, important new information was obtained that shows how optimum induced power varies with advance ratio, wake skew angle, trim condition, and the number of available rotor controls.

10.2 Finite Blade Summary

Applying the finite-state model to the dynamic inflow of the lifting rotor proves viable to a working solution of the induced-power for rotors with finite blade number. This formulation applies blade-element theory to account for the rotor loads on each blade. Combining these two theories has rendered an improved correction factor over the previous quadratic function to account for the swirl velocities in the rotor wake.

The modified correction factor has provided greater insight to the nature of the swirl velocities that had previously remained obscure. The presence of swirl vortices dramatically increases the induced-power demand and, thus, decreases the performance of the rotor for a given number of blades. However, the previous quadratic term drives the inflow solution to diverge from the results of Goldstein at inflow ratios close to unity. The improved swirl function compensates for the unique behavior at these higher velocities.

Blade number has a direct effect on the induced-power efficiency of the helicopter rotor. Plotting the induced-power ratio—that is, the induced-power coefficient C_P divided by the Glauert ideal induced-power coefficient C_{P_I}—as a function of the inverse of blade number displays a highly linear distribution that increases in slope with increasing advance ratio. The results presented provide evidence that increasing the number of blades on a lifting rotor greatly reduces the induced-power demand, thus reducing the overall power consumption. By introducing higher blade numbers, the rotor then redistributes the load throughout the disk in a more efficient manner—thus, increasing the number of blades increases the efficiency of the induced-power of the rotor.

The results presented were found to be in close agreement with previous investigations by Goldstein and others of induced power of the lifting rotor operating at moderate to high inflow ratios. There is also good correlation with data from Hall & Hall and Harris at moderate to high advance ratios. Insights from this investigation will aid in the design of future high-speed rotorcraft with higher aerodynamic efficiency.

10.3 Future Work

Inflow Feedback: The effect of inflow inducing circulation which, in turn, induces flow.

Reverse Flow: Inclusion of that portion of the rotor disk that encounters negative flow velocities during forward flight.

Circulation/Controls Mapping: Develop a transformation matrix that maps circulation to the controls vector and/or vice versa.

The effects of inflow feedback and reverse flow should be surveyed. Inflow feedback will better gauge the effects of solidity on induced-power and may account, at least in part, for the lower values compared with that of Harris. Including the effects of reverse flow will greatly aid in representing the singularity at the critical advance ratio in foward flight conditions. Mapping the controls to a desired circulation—and vice versa—will allow engineers to better design rotor blades that will generate more desirable results for lift, etc. These examinations will allow for modeling the behavior of realistic helicopter rotors—due, in part, to the limited amount of blade twist in current rotor designs as well as the complex nature of the flow distribution through the rotor.

Appendix A

Ellipsoidal Coordinate System

It is convenient to model the inflow and pressure distribution of the helicopter rotor in Ellipsoidal coordinates. This is a fully three dimensional orthogonal system in $\Re^3$.

A.1 Rotor Disk Coordinates

The rotor disk coordinate system (Cartesian, (x, y, z)) is located on the surface of the disk with its origin at the root, or hub, of the disk. Convention dictates that the x-axis points in the direction of forward flight. The z-axis points "downward" or with the direction of air flow. Thus, the y-axis must therefore lie in the plane of the disk pointing in the starboard direction, as depicted in the following diagram.

A.2 Ellipsoidal Coordinates

The Ellipsoidal coordinate system is defined by the following conditions.

$$\begin{aligned} x &= -\sqrt{1-\nu^2}\sqrt{1+\eta^2}\cos(\psi) \\ y &= \sqrt{1-\nu^2}\sqrt{1+\eta^2}\sin(\psi) \\ z &= -\eta\nu \end{aligned} \tag{A.1}$$

It should be noted that the quantities (ν, η, ψ) account for the entire domain of the flow field once and only once provided we restrict their values to the following ranges.

$$\begin{aligned} -1 \leq &\ \nu &&\leq +1 \\ 0 \leq &\ \eta &&< \infty \\ 0 \leq &\ \psi &&< 2\pi \end{aligned} \tag{A.2}$$

The ν equals constant surfaces are hyperboloids and change signs from one side of the disk to the other. The η equals constant surfaces are ellipsoids that approach spheres for very large η's and flatten to a disk—the rotor disk, in particular—for $\eta = 0$. ψ is the azimuthal angle that is measured positive from rotor aft (negative x-axis), counterclockwise as viewed from above the rotor disk.

The inverse of Eq.(A.1) is also available and is defined by the follwing.

$$\begin{aligned} \nu &= \frac{-\text{sign}(z)}{\sqrt{2}}\sqrt{(1-S)+\sqrt{(1-S)^2+4z^2}} \\ \eta &= -\frac{z}{\nu} \\ \psi &= \tan^{-}1(\frac{y}{-x}) \end{aligned} \tag{A.3}$$

where, $S \equiv x^2 + y^2 + z^2$.

Appendix B

Normalized Associated Legendre Functions

B.1 Laplace's Equation

In the development of the finite-state model, the fundamental equations of fluid dynamics—namely the continuity and momentum equations—where transformed into Laplace's equations $\nabla^2\Phi = 0$. It turns out that in three-dimensional Ellipsoidal coordinates, Laplace's equation is a partial differential equation that is daunting in appearance.

$$\frac{\partial}{\partial\nu}\left[(1-\nu^2)\frac{\partial\Phi}{\partial\nu}\right] + \frac{\partial}{\partial\eta}\left[(1+\eta^2)\frac{\partial\Phi}{\partial\eta}\right] + \frac{\partial}{\partial\psi}\left[\frac{(\nu^2+\eta^2)}{(1-\nu^2)(1+\eta^2)}\frac{\partial\Phi}{\partial\psi}\right] = 0 \tag{B.1}$$

However, if one choses a solution that is separable by way of products, i.e., $\Phi(\nu,\eta,\psi) = \Phi_1(\nu)\Phi_2(\eta)\Phi_3(\psi)$, the above partial differential equation becomes a set of ordinary differential equations.

$$\begin{aligned}
\frac{d}{d\nu}\left[(1-\nu^2)\frac{d\Phi_1}{d\nu}\right] + \left[-\frac{m^2}{1-\nu^2} + n(n+1)\right]\Phi_1 = 0 \\
\frac{d}{d\eta}\left[(1+\eta^2)\frac{d\Phi_2}{d\eta}\right] + \left[\frac{m^2}{1+\eta^2} - n(n+1)\right]\Phi_2 = 0 \\
\frac{d\Phi_3}{d\psi} + m^2\Phi_3 = 0
\end{aligned} \tag{B.2}$$

where m and n are constants of separation—written with appropriate exponents from hindsight. It is recognized that the first two equations in the above ordinary differential equations are forms of Legendre's associated differential equation. A general solution to the first equation is $P_n^m(\nu)$ and a general solution to the second is $Q_n^m(i\eta)$, where i is the imaginary $\sqrt{-1}$. These are referred to as associated Legendre functions of the first and second kind, respectively. There are also solutions of $P_n^m(i\eta)$ and $Q_n^m(\nu)$, but we allow the leading coefficients to these functions to be zero for all values of ν and η. This is due to the fact these functions yield divergent solutions for the pressure distribution in the flow field.

The third equation is also well known. This is the equation for simple harmonic motion. A general solution to the third equation is a combination of sines and cosines—e.g., $\cos(m\psi) + \sin(m\psi)$—with some set of leading coefficients to satisfy boundary conditions.

Therefore, a general solution to Laplace's equation in Ellipsoidal coordinates (from the method of separation of variables) is the product of all three solutions to the above ordinary differential equations.

$$\Phi_n^m(\nu,\eta,\psi) = \Phi_1(\nu)\Phi_2(\eta)\Phi_3(\psi) = P_n^m(\nu)Q_n^m(i\eta)\left(C_1\cos(m\psi) + C_2\sin(m\psi)\right) \quad \text{(B.3)}$$

where C_1 and C_2 are allowed to be functions of both m and n. They may also be time varying, so long as they remain independent of ellipsoidal coordinates (ν,η,ψ). The most general solution to the differential equation is the sum of all solutions. However, not just a summation but a sum that permits valid Legendre functions—i.e., the superscripts must not be greater in value than the subscripts. In should be noted that in this research, another restriction occurs on m and n. Boundary conditions require that only $m+n$ odd be retained due to the fact that this combination causes P_n^m to be an odd function. However, in this appendix we will disregard boundary conditions which were addressed in detail in Chapter2.1.

$$\Phi(\nu,\eta,\psi) = \sum_{m=0}^{\infty}\sum_{n=m,m+1,\cdots}^{\infty} P_n^m(\nu)Q_n^m(i\eta)\left(C_1\cos(m\psi) + C_2\sin(m\psi)\right) \quad \text{(B.4)}$$

B.2 Normalized Legendre Function

In this research the associated Legendre functions are normalized. For the normalization of $P_n^m(\nu)$, we use the following characteristic.

$$\int_0^1 \left(P_n^m(\nu)\right)^2 d\nu = \frac{1}{2n+1}\frac{(n+m)!}{(n-m)!} \equiv \left(\rho_n^m\right)^2 \tag{B.5}$$

Therefore, a normalized associated Legendre function can be defined as follows.

$$\bar{P}_n^m(\nu) \equiv \frac{(-1)^m}{\rho_n^m} P_n^m(\nu) \tag{B.6}$$

such that,

$$\int_0^1 \bar{P}_n^m(\nu)\bar{P}_j^m(\nu)d\nu = \delta_{nj} \tag{B.7}$$

where δ_{nj} is the Kronecker delta that equals 0 for all $n \neq j$ and equals 1 for $n = j$. Also, the normalization of $Q_n^m(i\eta)$ is defined in the following manner.

$$\bar{Q}_n^m(i\eta) \equiv \frac{Q_n^m(i\eta)}{Q_n^m(i0)} \tag{B.8}$$

Also, note that in this research, only the pressure distribution *on* the disk is of importance. This demands that the ellipsoidal coordinate η be zero for all computation. Thus, for all values of m and n

$$\bar{Q}_n^m(i0) = \frac{Q_n^m(i0)}{Q_n^m(i0)} = 1 \tag{B.9}$$

Therefore, the solution to Laplace's equation for the pressure distribution on the surface of the rotor disk is as follows.

$$\Phi(\nu,\psi) = \sum_{n,m} \bar{P}_n^m(\nu)\left(C_1\cos(m\psi) + C_2\sin(m\psi)\right) \tag{B.10}$$

where, again, the coefficients C_1 and C_2 may be functions of m and n as well as time varying.

Appendix C

General Galerkin Method

In the Galerkin Method, the goal is to seek an approximate solution to the linear[5] differential equation of interest. This is accomplished by assuming a solution that is comprised of a summation of known "trial" solutions. The general process is outlined here.

C.1 General Process

First let $L(u)$ be the linear differential operator. Then

$$L(u) = 0 \tag{C.1}$$

is the linear differential equation of interest. The approximate solution may then be expressed as;

$$u_a(x) = u_0 + \sum_{n=1}^{N} a_n \cdot \phi_n(x) \tag{C.2}$$

where $\phi_n(x)$ are the known/predetermined trial functions and u_0 is typically related to a boundary condition and thus considered known. This (u_0) may be thought of as $a_0 \cdot u(x = 0)$, where a_0 is unity, if $u(x = 0)$ is known, or some combination therein. One may now define a residual (or amount of error) in the approximate solution by

[5]Linear implies that the equation is linear in the *dependent* variable. This says nothing about the independent variable which may be of any order and generally of any complexity.

substituting this solution back into the differential equation.

$$R(a_0, a_1, \cdots, a_{N-1}, a_N, x) \equiv L(u_a) = L(u_0) + \sum_{n=1}^{N} a_n \cdot L(\phi_n) \tag{C.3}$$

According to Galerkin, one may solve for the unkown coefficients a_n by solving the following system of equations.

$$< R, \phi_m >= 0, \quad m = 1, 2, \cdots, N \tag{C.4}$$

where, by definition, the above equation is an inner product defined as follows.

$$< f, g > \equiv \int_D (f \cdot g) dx \tag{C.5}$$

Here, D is the domain of interest. Substitution of R and ϕ_m into Eq.C.4 yields the following.

$$\sum_{n=1}^{N} a_n < L(\phi_n), \phi_m > + < L(u_0), \phi_m >= 0 \tag{C.6}$$

or rewritten in matrix form,

$$\bar{M}\vec{A} = \vec{D} \tag{C.7}$$

where

$$m_{mn} \equiv < L(\phi_n), \phi_m > \tag{C.8}$$

$$d_m \equiv < L(u_0), \phi_m > \tag{C.9}$$

are all know values and a_n are the unknowns to be solved for.

C.2 Simple Example

As an illustration, consider the following linear differential equation, see Ref.[50].

$$\frac{du}{dx} = u \tag{C.10}$$

with the boundary condition, $u_0 = u(x = 0) = 1$, and bound to the following domain, $0 \leq x \leq 1$. Therefore, the linear differential operator may be defined as follows.

$$L(u) = \frac{du}{dx} - u = 0 \tag{C.11}$$

Then, assume a solution of the form presented in Eq.C.2.

$$u_a(x) = 1 + \sum_{n=1}^{N} a_n \cdot \phi_n(x) \tag{C.12}$$

The choice of trial functions is somewhat of an art and in general might not be arbitrarily chosen. Experience is often beneficial and in this case, the functions chosen is a power series.

$$\phi_n(x) \equiv x^n \tag{C.13}$$

Then the differential operator becomes:

$$L(u_a) = \frac{du_a}{dx} - u_a = R \tag{C.14}$$

where,

$$\frac{du_a}{dx} = 0 + \sum_{n=1}^{N} a_n \frac{d\phi_n(x)}{dx} = \sum_{n=1}^{N} n \cdot a_n \cdot x^{n-1} \tag{C.15}$$

Therefore,

$$R = \sum_{n=1}^{N} n \cdot a_n \cdot x^{n-1} - \left(1 + \sum_{n=1}^{N} a_n \cdot x^n\right) = -1 + \sum_{n=1}^{N} a_n (n \cdot x^{n-1} - x^n) \tag{C.16}$$

Chose ϕ_m (in Eq.C.4) from the set of trial functions ϕ_n. Also, ϕ_m must be the lowest-order members when evaluating the inner product, namely $\phi_m(x) \equiv x^{m-1}$. This, then, produces the following as the inner product.

$$< R, \phi_m >= \int_0^1 (-1 + \sum_{n=1}^{N} a_n (n \cdot x^{n-1} - x^n)) \cdot x^{m-1} dx = 0 \tag{C.17}$$

or rewritten,

$$\sum_{n=1}^{N} a_n \int_0^1 \left(n \cdot x^{n-1} - x^n\right) \cdot x^{m-1} dx = \int_0^1 x^{m-1} dx \tag{C.18}$$

or in matrix form,

$$\bar{M}\vec{A} = \vec{D} \tag{C.19}$$

where the elements of M and D are denoted as m_{mn} and d_m, respectively.

$$m_{mn} \equiv < x^{n-1} - x^n, x^{m-1} > = \frac{n}{m+n-1} - \frac{1}{m+n} \tag{C.20}$$

$$d_m \equiv < 1, x^{m-1} > = \frac{1}{m} \tag{C.21}$$

and a_n are the unknown coefficients to be solved for. In this case, for $n = 4$, the elements of A become:

$$A^T = \{0.9990, 0.5095, 0.1399, 0.0699\} \tag{C.22}$$

Therefore, the approximate solution to the differential equation Eq.C.10 is

$$u_a(x) = 1 + \sum_{n=1}^{N} a_n \cdot x^n = 1 + 0.9990 \cdot x + 0.5095 \cdot x^2 + 0.1399 \cdot x^3 + 0.0699 \cdot x^4 \tag{C.23}$$

The solution to the original differential equation is well known, $u(x) = e^x$. The below table illustrates the high accuracy of the Galerkin method with seemingly low algebraic effort.

Approximate Solution, u_a					
x	$N = 1$	$N = 2$	$N = 3$	$N = 4$	e^x
0.0	1.0000	1.0000	1.0000	1.0000	1.0000
0.2	1.4000	1.2057	1.2220	1.2214	1.2214
0.4	1.8000	1.4800	1.4913	1.4919	1.4918
0.6	2.2000	1.8229	1.8214	1.8221	1.8221
0.8	2.6000	2.2343	2.2259	2.2255	2.2255
1.0	3.0000	2.7143	2.7183	2.7183	2.7183

Table C.1: This table demonstrates the high order of accuracy that can be achieved with a minimal amount of algebraic effort.

Appendix D

Table Method

The computation of the induced-flow states from the Peters-He generalized dynamic wake model uses a series of harmonics. For each harmonic the radial term is then expanded in harmonics of polynomial powers. This method may be accomplished by first defining the number of harmonics to expand the induced velocity. This number is chosen based on the highest dynamic frequency of interest for a given condition. This provides the model with a limit to the degree of polynomial in $\bar{r}$.

Highest power of $\bar{r}$	m						Total Inflow States
	0	1	2	3	4	5	
0	1						1
1	1	1					3
2	2	1	1				6
3	2	2	1	1			10
4	3	2	2	1	1		15
5	3	3	2	2	1	2	21

Table D.1: Choice of number of spatial modes ($n + m$ =odd).

In order to determine the number of inflow states needed to obtain accurate results, the induced-power efficiency for differing numbers of harmonics was computed. The following table and plot shows the values of the efficiency for an actuator disk (no tilting of the lift vector) with an infinite number of blades ($Q = \infty$) in axial flow (skew angle χ is zero). In the limit that the harmonic terms continue to infinity, the induced-power efficiency is driven to unity. However, in the scope of this research, much of the computation is limited to a maximum harmonic of 10 which gives an efficiency value of more than 99%.

M_{max}	Induced-Power Efficiency
0	0.887
2	0.971
4	0.988
6	0.994
8	0.996
10	0.997
12	0.998
18	0.999

Table D.2: Numerical results of convergence with increasing number of harmonics.

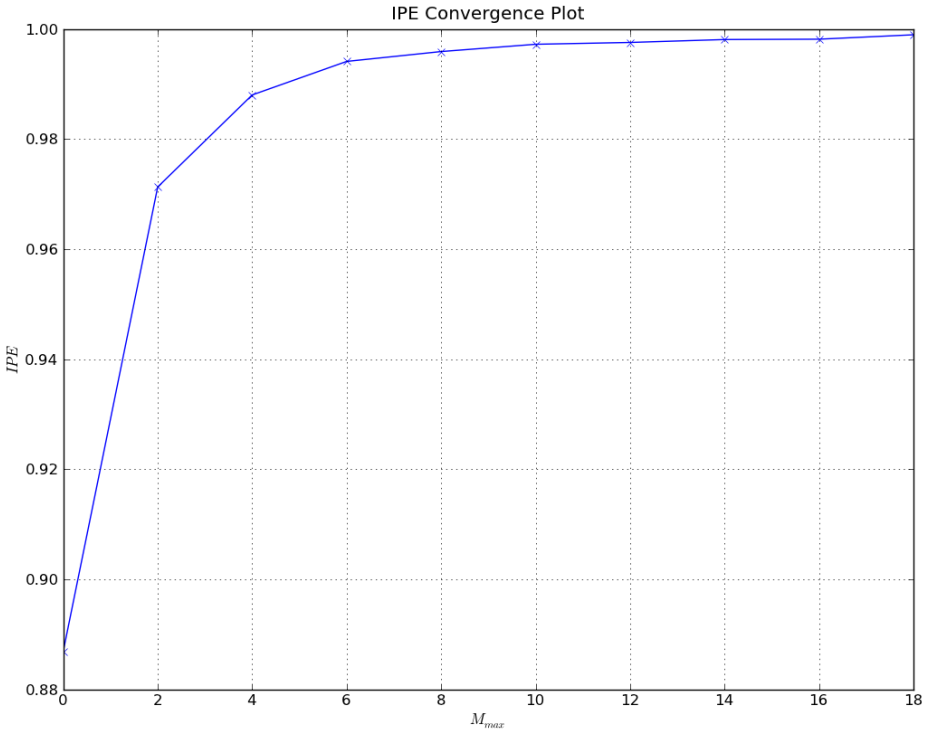

Figure D.1: Plot that demonstrates the rapid convergence of the finite-state method with increasing number of harmonics.

Appendix E

Transformation Matrices

The development of the $[A]$ matrix was outlined in Chapter 5.1 as part of the introduction of blade-element theory to the general performance formulation and the constraints for induced power optimization. This appendix is provided to clarify the finite-state inflow theory and details of the derivation of $[A]$.

In the mathematical notation of Associated Legendre functions, there is a superscript m and a subscript n. These arise from the separation of variables that is used in the solution of Laplaces equation in elliptical coordinates[6]. The ellipsoids of ellipsoidal coordinates collapse down to a circle of radius unity at mid-plane, and the Legendre functions are allowed discontinuities across that disk. The superscript m denotes the harmonic number of the solution, and the subscript n denotes the order of the radial term on the disk.

Because the solutions to Laplaces equation must be analytical across the center of the circular disk, it follows that only $n \geq m$ values are allowed—i.e., Legendre functions are defined for only those values. Furthermore, functions with $m + n$ odd represent discontinuities in the function across the disk; and they are used for pressure drop across the disk—i.e., lift—whereas functions with $m+n$ even represent a discontinuity in the normal derivative—i.e., a mass source. As a consequence, the only values of n admitted in the Peters-He model of dynamic inflow, Ref.[43], are $n = m + 1, m + 3, m + 5, \cdots$.

In the Peters-He theory, both the dynamic-inflow states, Eq.(3.4), and the pressure expansion coefficients, Eq.(3.6), have this standard superscript/subscript notation.

[6]See AppendixB

As a consequence, the matrix that relates these two sets of variables, $[\bar{L}]$, has a set of superscripts/subscripts (m, n) that relate to the inflow state (i.e., the row location) and another set of superscripts/subscripts (r, j) that relate to the pressure expansion (i.e., the column location). In addition, the harmonic numbers (m and r) have an associated superscript c or s to indicate whether they refer to a cosine harmonic or a sine harmonic. In order to facilitate the computations with standard matrix subroutines, Ref.[43] has elected to write the matrices of the dynamic wake model in partitions that represent the harmonic numbers with rows and columns within each partition (that refer to the allowed values on n (or j) for that row (or column) of the matrix). Reference [43] shows that the most consistent inflow model (and the one with the best convergence) is one for which the subscripts of any given harmonic are all limited to some maximum value, $n_{max} = M + 1$. This automatically limits the highest harmonic of the matrices to be $M = n_{max} - 1$. As a consequence of this procedure, the inflow expansion functions ϕ_n^m are polynomials in the radial position $\bar{r}$ that go as $(\bar{r})^m$, $(\bar{r})^{m+2}$, $(\bar{r})^{m+4}$ with the maximum allowed power of $\bar{r}$ being M:

$$\phi_n^m(\bar{r}) = \sqrt{H_n^m \cdot (2n+1)} \sum_{q=m,m+2,\cdots}^{n-1} \bar{r}^q \frac{(-1)^{(q-m)/2}(n+q)!\,!}{(q-m)!\,!\,(q+m)!\,!\,(n-q-1)!\,!} \tag{E.1}$$

where

$$H_n^m = \frac{(n+m-1)!\,!\,(n-m-1)!\,!}{(n+m)!\,!\,(n-m)!\,!} \tag{E.2}$$

E.1 Finite-State Wake Notation

The indexing of $[\bar{L}^c]$ in Eq.(5) takes the following form.

$$[\bar{L}_{nj}^{mrc}] = \left[\begin{array}{c|c|c|c|c|c} 00 & 00 & 01 & 01 & 02 & 03 \\ 11 & 13 & 12 & 14 & 13 & 14 \\ 00 & 00 & 01 & 01 & 02 & 03 \\ 31 & 33 & 32 & 34 & 33 & 34 \\ \hline 10 & 10 & 11 & 11 & 12 & 13 \\ 21 & 23 & 22 & 24 & 23 & 24 \\ 10 & 10 & 11 & 11 & 12 & 13 \\ 41 & 43 & 42 & 44 & 43 & 44 \\ \hline 20 & 20 & 21 & 21 & 22 & 23 \\ 31 & 33 & 32 & 34 & 33 & 34 \\ \hline 30 & 30 & 31 & 31 & 32 & 33 \\ 41 & 43 & 42 & 44 & 43 & 44 \end{array}\right] \tag{E.3}$$

Equation (E.3) shows the row/column superscripts and subscripts for $[\bar{L}^c]$ for the case $M = 3$. The indices for $[\bar{L}^s]$ are the same with the exception that the $m = 0$, $r = 0$ rows and columns are omitted. Notice that, due to this truncation of n at $M + 1$, not all of the partitioned matrices (for given values of m and r) are of the same size and not all are square. Since both inflow states and pressure expansions are given the same limitation, the maximum r is also M and the maximum j is also $M + 1$. Thus, $[\bar{L}]$ is a square matrix even though its partitions need not be square. The total number of states (cosine + sine) is $(M+1)(M+2)/2$. Thus, a three-harmonic model ($M = 3$) has 10 states as seen in Eq.(E.3).

Since this notation has been used throughout the history of the theory for inflow and pressure expansions, it has been modified here to be used for the allowable pitch inputs introduced in Eq.(5.1) (rewritten here for convenience).

$$\theta(\bar{r}, \psi_q) = \sum_{k=0}^{K} \sum_{m=0}^{M} \left[\bar{r}^k \left[\theta_k^{mc} \cdot cos(m\psi_q) + \theta_k^{ms} \cdot sin(m\psi_q)\right]\right] \tag{E.4}$$

Here, the superscript m represents the harmonic of the allowed pitch input and the subscript k represents the power of r in the expansion.

E.2 $[A]$ Matrix Explanation

The integral equations (Eq.(5.6)) used to determine $[A]$ are based on blade-element theory, and the derivation is given in Chapter 6. It follows that the matrices $[A]$ and $[P]$ will have row partitions and row indices that correspond to the $[\bar{L}]$ matrix. They will also have column indices such that the superscript is a harmonic partition r. However, within each column partition, k is allowed to go up to any desired maximum value K that need not be the same for each partition. Thus, these matrices need not be square. Equation (E.5) shows the subscripts and superscripts for the case $M = 3$, $r_{max} = 1$ (1 pitch harmonic) for both uniform and linear twist ($k = 0, 1$). Thus, the

indexing of $[A]$ will be in the following manner:

$$[A_{nj}^{mr}] = \left[\begin{array}{cccccc|cccc}
00 & 00 & 01 & 01 & 02 & 03 & 01 & 01 & 02 & 03 \\
10 & 13 & 12 & 14 & 13 & 14 & 12 & 14 & 13 & 14 \\
00 & 00 & 01 & 01 & 02 & 03 & 01 & 01 & 02 & 03 \\
30 & 33 & 32 & 34 & 33 & 34 & 32 & 34 & 33 & 34 \\
\hline
10 & 10 & 11 & 11 & 12 & 13 & 11 & 11 & 12 & 13 \\
20 & 23 & 22 & 24 & 23 & 24 & 22 & 24 & 23 & 24 \\
10 & 10 & 11 & 11 & 12 & 13 & 11 & 11 & 12 & 13 \\
40 & 43 & 42 & 44 & 43 & 44 & 42 & 44 & 43 & 44 \\
\hline
20 & 20 & 21 & 21 & 22 & 23 & 21 & 21 & 22 & 23 \\
30 & 33 & 32 & 34 & 33 & 34 & 32 & 34 & 33 & 34 \\
\hline
30 & 30 & 31 & 31 & 32 & 33 & 31 & 31 & 32 & 33 \\
40 & 43 & 42 & 44 & 43 & 44 & 42 & 44 & 43 & 44 \\
\hline\hline
10 & 10 & 11 & 11 & 12 & 13 & 11 & 11 & 12 & 13 \\
20 & 23 & 22 & 24 & 23 & 24 & 22 & 24 & 23 & 24 \\
10 & 10 & 11 & 11 & 12 & 13 & 11 & 11 & 12 & 13 \\
40 & 43 & 42 & 44 & 43 & 44 & 42 & 44 & 43 & 44 \\
\hline
20 & 20 & 21 & 21 & 22 & 23 & 21 & 21 & 22 & 23 \\
30 & 33 & 32 & 34 & 33 & 34 & 32 & 34 & 33 & 34 \\
\hline
30 & 30 & 31 & 31 & 32 & 33 & 31 & 31 & 32 & 33 \\
40 & 43 & 42 & 44 & 43 & 44 & 42 & 44 & 43 & 44
\end{array}\right] \tag{E.5}$$

The structure of Eq.(5.6) indicates the following integrals over $\bar{r}$ which, due to Eq.(E.1), can be done in closed form.

$$S_{n,k}^{m}(\bar{r}) \equiv \int_0^1 \phi_n^m(\bar{r}) \cdot \bar{r}^k d\bar{r} \tag{E.6}$$

With this definition, one can construct all the elements of $[A_{nk}^{mr}]$ in closed form. Equation E.7 shows the elements of $[A_{nk}^{mr}]$ for $M = 3$, $R_{max} = 1$, where $m_{(c,s)}$ is the harmonic number of τ, and $r_{(c,s)}$ is the harmonic number of θ. The matrix $[B]$ is

formed in a similar manner but that derivation is not given herein.

$$
[A_{nk}^{mr}] = \left[\begin{array}{c|c|c}
\begin{array}{c} m_c = 0, r_c = 0 \\ \\ S^0_{n,k+2} + \frac{1}{2}\mu^2 S^0_{n,k} \end{array} & \begin{array}{c} m_c = 0, r_c = 2 \\ \\ \frac{1}{4}\mu^2 S^0_{n,k} \end{array} & \begin{array}{c} m_c = 0, r_s = 1 \\ \\ \mu S^0_{n,k+1} \end{array} \\
\hline
\begin{array}{c} \\ \\ m_c = 2, r_c = 0 \\ \\ \frac{1}{2}\mu^2 S^2_{n,k} \end{array} & \begin{array}{c} m_c = 1, r_c = 1 \\ \\ S^1_{n,k+2} + \frac{1}{4}\mu^2 S^1_{n,k} \\ \hline m_c = r_c > 1 \\ \\ S^{r>1}_{n,k+2} + \frac{1}{2}\mu^2 S^{r>1}_{n,k} \\ \hline m_c = r_c \pm 2, r > 2 \\ \\ -\frac{1}{4}\mu^2 S^{r\pm 2}_{n,k} \end{array} & \begin{array}{c} \\ \\ m_c = r_s + 1 \\ \\ -\mu S^{r+1}_{n,k+1} \\ \hline m_c = r_s - 1 \\ \\ \mu S^{r-1}_{n,k+1} \\ \\ \end{array} \\
\hline
\begin{array}{c} \\ \\ m_s = 1, r_c = 0 \\ \\ 2\mu S^1_{n,k+1} \end{array} & \begin{array}{c} \\ \\ m_s = r_c + 1 \\ \\ \mu S^{r+1}_{n,k+1} \\ \hline m_s = r_c - 1 \\ \\ -\mu S^{r-1}_{n,k+1} \\ \\ \end{array} & \begin{array}{c} m_s = 1, r_s = 1 \\ \\ S^1_{n,k+2} + \frac{3}{4}\mu^2 S^1_{n,k} \\ \hline m_s = r_s > 1 \\ \\ S^{r>1}_{n,k+2} + \frac{1}{2}\mu^2 S^{r>1}_{n,k} \\ \hline m_s = r_s \pm 2, r > 2 \\ \\ -\frac{1}{4}\mu^2 S^{r\pm 2}_{n,k} \end{array}
\end{array}\right] \tag{E.7}
$$

E.3 $[T]$ Matrix Explanation

The orthogonality matrix $[T_{nj}^{mr}]$ defined in Eq.(6.7) follows the notation from the Peters-He inflow theory. For example, the cosine partition exhibits the following convention.

$$[T_{nj}^{mr}] \Rightarrow \left[\begin{array}{cc:cc:cc} 00 & 00 & 01 & 01 & 02 & 03 \\ \underline{11} & \underline{13} & \underline{12} & \underline{14} & \underline{13} & \underline{14} \\ 00 & 00 & 01 & 01 & 02 & 03 \\ \underline{31} & \underline{33} & \underline{32} & \underline{34} & \underline{33} & \underline{34} \\ \hline\hline 10 & 10 & 11 & 11 & 12 & 13 \\ \underline{21} & \underline{23} & \underline{22} & \underline{24} & \underline{23} & \underline{24} \\ 10 & 10 & 11 & 11 & 12 & 13 \\ \underline{41} & \underline{43} & \underline{42} & \underline{44} & \underline{43} & \underline{44} \\ \hline 20 & 20 & 21 & 21 & 22 & 23 \\ \underline{31} & \underline{33} & \underline{32} & \underline{34} & \underline{33} & \underline{34} \\ \hline 30 & 30 & 31 & 31 & 32 & 33 \\ 41 & 43 & 42 & 44 & 43 & 44 \end{array}\right] \tag{E.8}$$

where the 0^{th} harmonic terms are only present in the cosine states (i.e., the sine partition will contain the same terms as the cosine partition with the exception of the zeroeth terms). From the definition of the orthogonality matrix, the pressure loading coefficients may be expressed in the following manner:

$$\{\tau_n^{0c}\} = \sum_{r,j} T_{nj}^{0r} \left(\gamma_j^{rc} \cos(rt) + \gamma_j^{rs} \sin(rt)\right) \tag{E.9}$$

$$\begin{aligned} \{\tau_n^{mc}\} = \sum_{r,j} T_{nj}^{mr} \big[\gamma_j^{rc} &\left(\cos\left((m+r)t\right) + \cos\left((m-r)t\right)\right) \\ &+ \gamma_j^{rs} \left(\sin\left((m+r)t\right) - \sin\left((m-r)t\right)\right)\big] \end{aligned} \tag{E.10}$$

$$\begin{aligned} \{\tau_n^{ms}\} = \sum_{r,j} T_{nj}^{mr} \big[\gamma_j^{rc} &\left(\sin\left((m+r)t\right) + \sin\left((m-r)t\right)\right) \\ &- \gamma_j^{rs} \left(\cos\left((m+r)t\right) - \cos\left((m-r)t\right)\right)\big] \end{aligned} \tag{E.11}$$

The above equations may be recast into a set of matrices that map the lift coefficients γ_j^r to the pressure expansion coefficients τ_n^m for a given blade harmonic k. These matrices are partitioned by the sum/difference of m and r based on the following:

$$|m \pm r| = k \tag{E.12}$$

which comes about from the use of trigonometric rules when carrying out the integrals in Eq.(6.6). The above relation states the only values that are allowed in the computation are the sum and/or difference of harmonic numbers that are, in turn, equal to integer multiples of blade number (i.e., $k = 0, Q, 2Q, \cdots$). This, along with the orthogonality of the Legendre functions, allows values from Eq.(6.7) into only partitions of m and r that are equal to k, Eq.(E.12). All other harmonic partitions are zero.

This defines a simple set of matrices that may be used to transorm the influence coefficient matrices into the appropriate harmonics for a rotor with a given number of blades.

To demonstrate this assume a rotor with, say, 2 blades. Then, the only allowable blade harmonics are $k = 0, 2, 4, 6, \cdots$ up to a maximum harmonic k_{max}. To illustrate further, below are the matrix partitions for the example of $k = 2$:

$[T^{cc}]_2 \Rightarrow$

$m \diagdown r$	0	1	2	3	4
0			T^{02}		
1		T^{11}		T^{13}	
2	$2T^{20}$				$\ddots$
3		T^{31}			
4			T^{42}		
5				$\ddots$	

$[T^{cs}]_2 \Rightarrow$

$m \diagdown r$	1	2	3	4	5
0		T^{02}			
1	T^{11}		T^{13}		
2				T^{24}	
3	$-T^{31}$				$\ddots$
4		$-T^{42}$			
5			$\ddots$		

$$[T^{sc}]_2 \Rightarrow \begin{array}{c|c} m \diagdown r & \begin{array}{ccccc} 0 & 1 & 2 & 3 & 4 \end{array} \\ \hline 1 & \left[\begin{array}{c||c|c|c|c} & T^{11} & & -T^{13} & \\ \hline 2T^{20} & & & & \ddots \\ \hline & T^{31} & & & \\ \hline & & T^{42} & & \\ \hline & & & \ddots & \end{array}\right] \\ 2 & \\ 3 & \\ 4 & \\ 5 & \end{array}$$

$$[T^{ss}]_2 \Rightarrow \begin{array}{c|c} m \diagdown r & \begin{array}{ccccc} 1 & 2 & 3 & 4 & 5 \end{array} \\ \hline 1 & \left[\begin{array}{c|c|c|c|c} -T^{11} & & T^{13} & & \\ \hline & & & T^{24} & \\ \hline T^{31} & & & & \ddots \\ \hline & T^{42} & & & \\ \hline & & \ddots & & \end{array}\right] \\ 2 & \\ 3 & \\ 4 & \\ 5 & \end{array}$$

where the submatrix, say, T^{31} takes the following form:

$$[T^{3,1}_{n,j}] = \int_0^1 \bar{P}^3_n(\nu)\bar{P}^1_j(\nu)d\nu \tag{E.13}$$

The partitions of the harmonic transformation matrix $[T^{xx}_k]$ where $|m \pm r| \neq k$ are zero matrices.

The above relations therefore reduce the pressure integrals of Eq.(6.6) to the compact matrix representation found in Eq.(6.9)

References

[1] Glauert, H., "A General Theory of the Autogyro," R&M No. 1111, Aeronautical Research Council of Great Britain, March 1927.

[2] Betz. A. and Prandtl, L., "Schraubenpropeller mit geringstem energieverlust," Goettinger Nachrichten, March 1919, pp. 193-217.

[3] Goldstein, S., "On the Vortex Theory of Screw Propellers," Proceedings of the Royal Society of London. Series A, Containing Papers of a Mathematical and Physical Character, Vol. 123, The Royal Society, April 6, 1929, pp. 440-465.

[4] Glauert, H. *Aerodynamic Theory: A General Review of Progress*, Vol. IV, Division L, Airplane Propellers. Dover Publications, Inc., New York, 1980.

[5] Mangler, K. W., "Fourier Coefficients for Downwash of a Helicopter Rotor," Royal Aircraft Establishment Tech. Note No. 1958 (A.R.C. 11694), 1948.

[6] Mangler, K. W. and Squire, H. B., "The Induced Velocity Field of a Rotor," Royal Aircraft Establishment Reports & Memorandum No. 2642, 1950.

[7] Joglekar, M. and Loewy, R., "An Actuator-Disk Analysis of Helicopter Wake Geometry and the Corresponding Blade Response," USAAVLABS Technical Report 69-66, 1970.

[8] Kinner, W., "Theory of the Circular Wing," Ingenieur Archiv, Vol. 7, 1937, pp. 47, Translation No. 2345, Ministry of Aircraft Production, U.K.

[9] Peters, David A., "How Dynamic Inflow Survives in the Competitive World of Rotorcraft Aerodynamics," the 2008 Alexander Nikolsky Lecture, *Journal of the American Helicopter Society*, Vol. 53, No. 1, January 2009, pp. 1-15.

[10] Sissingh, G. J., "The Effect of Induced Velocity Variation on Helicopter Rotor Damping in Pitch or Roll," Aeronautical Research Council (Great Britain), A.R.C. Technical Report C.P. No. 101 (14,757), 1952.

[11] Ormiston, R. A. and Peters, D. A., "Hingeless Helicopter Rotor Response with Nonuniform Inflow and Elastic Blade Bending," *Journal of Aircraft*, Vol. 9, No. 10, October 1972, pp. 730-736.

[12] Ormiston, R. A., "An Actuator Disc Theory for Rotor Wake Induced Velocities," proceedings of the AGARD Specialists' Meeting on the Aerodynamics of Rotary Wings, Marseilles, France, September 13-5, 1972; AGARD CP-111, February 1973.

[13] Peters, David A., "Hingeless Rotor Frequency Response with Unsteady Inflow," Proceedings of the American Helicopter Society Dynamics Specialists' Meeting, NASA Ames Research Center, NASA SP-352, February 1974, pp. 1-12.

[14] Baskin, V.E., Vil'dgrube, L.S., Vozhdayev, Ye. S., and Maykapar, G.I., "Teoriya Nesushchego," edited by A.K. Martunov, Mashinostroyeniye Press, Moscow, 1973, pp. 1-364: also appearing as "Theory of the Lifting Airscrew," NASA TT F-823, February 1976, translated by W.Z. Stepniewski and W.L. Metz.

[15] Pitt, Dale M. and Peters, David A., "Theoretical Prediction of Dynamic-Inflow Derivatives," Vertica, Vol. 5, 1981, pp. 21-34.

[16] Peters, D.A., and He, Cheng Jian, "Finite State Induced Flow Models Part II: Three-Dimensional Rotor Disk," *Journal of Aircraft*, Vol. 32, No. 2., March-April, 1995, pp. 323-333.

[17] Loewy, R. G., "A Two-Dimensional Approach to the Unsteady Aerodynamics of Rotary Wings," *Journal of Aerospace Science*, Vol. 24, 1957, pp. 81-98.

[18] Peters, D.A., and Makinen, S.M., "A Comparison of Prandtl and Goldstein Optimum Propeller Solutions with Finite-State Dynamic Wake Models," Georgia Institute of Technology and Army Research Office 10th International Workshop on Aeroelasticity of Rotorcraft Systems, Atlanta, GA, November 3-5, 2003.

[19] Makinen, Stephen M., *Applying Dynamic Wake Models to Large Swirl Velocities for Optimal Propellers*, Doctor of Science Thesis, Washington University in St. Louis, May 2005.

[20] Morillo, Jorge and Peters, David, "Velocity Field Above a Rotor Disk by a New Dynamic Inflow Model," *Journal of Aircraft*, Vol. 39, No. 5, Sept.-Oct. 2002, pp. 731-738.

[21] Peters, David A., Hsieh, Antonio, and Garcia-Duffy, Cristina, "A Complete Finite-State Inflow Theory from the Potential Flow Equations," Keynote Lecture, 3rd International Basic Research Conference on Rotorcraft Technology, Nanjing, China, Oct. 14-16, 2009.

[22] Garcia-Duffy, Cristina, Hsieh, Antonio, and Peters, David A., "A Complete Nonlinear Induced Flow Theory for Rotors in Incompressible Flow," 11th Pan-American Congress of Applied Mechanics PACAM XI, Foz do Iquau, Peran, Brazil, January 4-8, 2010.

[23] Garcia-Duffy, Cristina, *Applying Dynamic-Wake Models to Induced Power Calculations for an Optimum Rotor*, PhD Thesis, Washington University in St. Louis, December 2008.

[24] Harris, Franklin D., "Rotary Wing Aerodynamics Historical Perspectives and Important Issues," paper presented at the American Helicopter Society Southwest Region National Specialists' Meeting on Aerodynamics and Aeroacoustics, February 25-27, 1987.

[25] Ormiston, Robert A., "An Analytical Formulation for Lifting Rotor Induced Power," Proceedings of the AHS International 65th Annual Forum and Technology Display, Grapevine, TX, May 27-29, 2009.

[26] Hall, Kenneth C. and Hall, Steven R., "A Variational Method for Computing the Optimal Aerodynamic Performance of Conventional and Compound Helicopters," *Journal of the American Helicopter Society*, Vol. 55, No. 4, October, 2010, pp. 042006-1 042006-16.

[27] Peters, David A., File, Chad, Ormiston, Robert A., "Rotor Performance and Optimum Power from Finite-State Inflow with Realistic Constraints," Proceedings of the AHS International 67th Annual Forum and Technology Display, Virginia Beach, VA, May 3-5, 2011.

[28] Hall, S. R., Yang, K.Y., and Hall, K.C., "Helicopter Rotor Lift Distributions for Minimum-Induced Power Loss," *Journal of Aircraft*, Vol. 31, No. 4, 1994, pp.873-845.

[29] Makinen, Stephen and Peters, David, "Comparison of Dynamic Wake Models with Closed-Form Optimum Propeller Solutions," Paper No. 9, Proceedings of the 30th European Rotorcraft Forum, Marseilles, France, September 14-16, 2004.

[30] Peters, David A. and Garcia-Duffy, Cristina, "Optimum Rotor Performance in Axial Flow by Finite-State Methods," Proceedings of the AHS International 63rd Annual Forum and Technology Display, Virginia Beach, VA, May 1-3, 2007.

[31] Moffitt, R.C. and Bissell, J.R., "Theory and Application of Optimum Airloads to Rotors in Hoover and Forward Flight," Proceedings of the 38th Annual Forum of the American Helicopter Society, Washington, DC, 1982, pp. 1-12.

[32] Quackenbush, T.R., Wachspress, D.A., and Kaufman, A.E., "Optimization of Rotor Performance in Hover Using a Free Wake Analysis," *Journal of Aircraft*, Vol. 28, No. 3, 1991, pp. 200-207.

[33] Rand, O., Khromov, V., and Peyran, R.J., "Minimum-Induced Power Loss of a Helicopter Rotor via Circulation Optimization," *Journal of Aircraft*, Vol. 41, No. 1, 2004, pp.104-109.

[34] Ormiston, Robert A., "Further Investigations of Helicopter Rotor Induced Power," Proceedings of the AHS International 61st Annual Forum and Technology Display, Grapevine, TX, June 1-3, 2005.

[35] Wachspress, Daniel A., Quackenbush, Todd R., and Solomon, Christine L., "On Minimum Induced Power of the Helicopter Rotor," CDI Report No. 05-04, Continuum Dynamics, Inc., February 2005.

[36] Garcia-Duffy, Cristina, Peters, David A., and Ormiston, Robert A., "Optimum Rotor Performance in Skewed Flow Based on Actuator-Disk Theory," Proceedings of the 27th AIAA Applied Aerodynamics Conference, San Antonio, TX, June 22-25, 2009, AIAA-2009-3517.

[37] Harris, Franklin D., "An Overview of Autogyros and The McDonnell XV-1 Convertiplane," NASA/CR-2003-212799, October 2003.

[38] Ormiston, Robert A., "Induced Power of the Helicopter Rotor," Proceedings of the AHS International 60th Annual Forum and Technology Display, Baltimore, MD, June 8-10, 2004.

[39] Ormiston, Robert A., "A New Formulation for Lifting Rotor Performance Including Comparison with Full-Scale Data," Proceedings of the AHS International 64st Annual Forum and Technology Display, Montreal, Quebec, Canada, April 29 - May 1, 2008.

[40] Saberi, Hossein; Khoshlahjeh, Maryam; Ormiston, Robert A.; and Rutkowski, M.J., "Overview of RCAS and Application to Advanced Rotorcraft Problems," AHS 4th Decennial Specialist's Conference on Aeromechanics, San Francisco, CA, January 21-23, 2004.

[41] Ormiston, Robert A., "Applications of the Induced Power Model and Performance of Conventional and Advanced Rotorcraft," Proceedings of the American Helicopter Society Aeromechanics Specialists' Conference, San Francisco, CA, January 20-22, 2010.

[42] Peters, David A. and He, Chengjian, "A Closed Form Unsteady Aerodynamic Theory for Lifting Rotor in Hover and Foward Flight," Proceedings of the 43rd Annual National Forum of the American Helicopter Society, St. Louis, Missouri, May 1987.

[43] He, Cheng Jian, *Development and Applications of a Generalized Dynamic Wake Theory for Lifting Rotors*, Ph.D. Dissertation, Georgia Institute of Technology, August 1998.

[44] Peters, David A. and He, Cheng Jian, "Correlation of Measured Induced Velocities with a Finite-State Wake Model," *Journal of the American Helicopter Society*, Vol. 36, No. 3, July 1991, pp. 59-70.

[45] Wheatley, J.B., "An Aerodynamic Analysis of the Autogiro Rotor With a Comparison Between Calculated and Experimental Results," NACA Technical Report 487, 1934.

[46] Wheatley, J.B., "An Analytical and Experimental Study of the Effects of Periodic Blade Twist on the Thrust, Torque, and Flapping Motion of an Autogiro Rotor," NACA TR-591, 1937.

[47] Bailey, F. J., Jr., "A Study of the Torque Equilibrium of an Autogiro Rotor," NACA TR-623, 1938.

[48] Bailey, F. J., Jr., "A Simplified Theoretical Method of Determining the Characteristics of a Lifting rotor in Forward Flight," NACA TR-716, 1941.

[49] Gessow, A. and Myers, Garry C., *Aerodynamics of the Helicopter*, Ungar, New York, 1952

[50] Fletcher, C.A.J., *Computational Galerkin Methods*, Springer-Verlag, New York, 1984, pp.4-6.

Vita

Chad L. File

Degrees

Ph.D. Aerospace Engineering, Washington Univeristy, May 2013
M.S. Aerospace Engineering, Washington Univeristy, December 2011
B.S. Physics, SIUe, May 2009
B.S. Mechanical Engineering, SIUe, December 2008
A.S. General Studies, Kaskaskia College, May 2005

Professional Societies

AHS International - The Vertical Flight Society
American Institute of Aeronautics and Astronautics
American Physical Society
Society of Industrial & Applied Mathematics

Publications

Peters, D.A., **File, C.L.**, Ormiston, R.A., "Rotor Performance and Optimum Power from Finite-State Inflow with Realistic Constraints," Proceedings of the AHS International 67th Annual Forum and Technology Display, Virginia Beach, VA, May 3-5, 2011.

File, C.L., Modarres, R., Peters, D.A., "Blade Number Effect on Optimum Rotor Performance in Axial Flow by Dynamic Wake Theory with Improved Swirl Correction," Proceedings of the 38th European Rotorcraft Forum, Amsterdam, the Netherlands, September 4-7, 2012.

May 2013